Measurement of Single π^0 Production in Neutral Current Neutrino Interactions on Water at the Near Detector of the T2K experiment

A Dissertation presented

by

Zoya Vallari

to

The Graduate School

in Partial Fulfillment of the

Requirements

for the Degree of

Doctor of Philosophy

in

Physics and Astronomy

Stony Brook University

December 2018

Stony Brook University

The Graduate School

Zoya Vallari

We, the dissertation committee for the above candidate for the

Doctor of Philosophy degree, hereby recommend

acceptance of this dissertation

Chang Kee Jung - Dissertation Advisor
Professor, Physics and Astronomy

Rouven Essig - Chairperson of Defense
Associate Professor, Physics and Astronomy

Joanna Kiryluk
Associate Professor, Physics and Astronomy

Clark McGrew
Associate Professor, Physics and Astronomy

Xin Qian
Physicist, Brookhaven National Laboratory

This dissertation is accepted by the Graduate School

Dean of the Graduate School

Abstract of the Dissertation

Measurement of Single π^0 Production in Neutral Current Neutrino Interactions on Water at the Near Detector of the T2K experiment

by

Zoya Vallari

Doctor of Philosophy

in

Physics and Astronomy

Stony Brook University

2018

T2K is a long baseline neutrino oscillation experiment located in Japan. It was built mainly to detect muon neutrino to electron neutrino oscillation and to measure the mixing angle θ_{13} of the PMNS matrix, along with the precision measurement of θ_{23} and mass differences. A ν_μ beam is produced at the Japan Proton Accelerator Research Complex (J-PARC) in Tokai and travels to the far detector in Kamioka, Japan. There is an ensemble of detectors at 280 m downstream of the target that form the near detector. Super-Kamiokande, a water Cherenkov detector, located 295 km away from the target serves as the far detector.

The two main backgrounds for electron neutrino appearance at the Super-Kamiokande are the inherent electron neutrino component of the beam and the π^0 particle produced via neutral current channel (NC1π^0) that mimics the electron neutrino interaction signature. To effectively constrain the NC1π^0 interaction rate on water, the Pi0 Detector (P0D) was built as one of the near detectors. This detector can be filled and drained with water periodically to enable extraction of neutrino interactions on water.

This analysis measures the NC1π^0 interaction rate on water in the P0D. It uses neutrino beam data of 3.53 $\times 10^{20}$ protons-on-target (POT) for the water-in configuration of the P0D and 6.70 $\times 10^{20}$ POT for the water-out configuration. A set of selections are implemented to obtain a sample enriched in signal events.

The π^0 invariant mass distribution is compared between data and Monte Carlo. Parameter estimation using Markov Chain Monte Carlo sampling method is performed to measure the signal events in data.

The data fit results in 130 ± 20 events on water including both statistical and systematic uncertainties for an expected value of 167 events predicted by the NEUT Monte Carlo. The ratio between nominal Monte Carlo and the best fit value is 0.78 ± 0.12.

Dedication Page

To Ma & Pa

Contents

1 Introduction **1**

1.1 The Standard Model 1

1.2 Neutrino Oscillation 3

1.2.1 Theoretical formulation 4

1.2.2 Experimental measurements 7

1.3 Neutrino - Nucleus Interactions 12

1.3.1 Interaction Modes 13

1.3.2 Nuclear Effects 16

1.3.3 Neutral Current Single π^0 Measurements 17

2 The T2K Experiment **23**

2.1 Neutrino Beamline 24

2.2 The Near Detector 26

2.2.1 INGRID : On-axis detector 26

2.2.2 ND280 : Off-axis detector 28

2.3 Super-Kamiokande : The Far Detector 30

2.4 PØD : The Pi0 Detector 30

2.4.1 P0D Reconstruction 32

3 Signal Selection **35**

3.1 Signal Sample 36
3.1.1 Selection Efficiencies 42
3.1.2 Reconstructed particles - True π^0 Association 51
3.2 Background Control Sample 55

4 Bayesian Inference for Parameter Estimation 61
4.1 The Markov Chain Monte Carlo Method 61
4.1.1 Metropolis-Hastings Algorithm 62
4.1.2 Adaptive Metropolis-Hastings Algorithm 64
4.2 Likelihood 64
4.2.1 Fit Parameters 65

5 Systematic Uncertainty 68
5.1 Cross Section & FSI Parameters 68
5.2 Flux Parameters 73
5.3 Detector Systematics Parameters 75

6 Results 88
6.1 Input Samples 88
6.2 Prior-Posterior Comparisons 91
6.3 Signal Event Rate 95
6.4 Posterior Predictive Distributions 96
6.5 Goodness-of-Fit 101

7 Conclusion 102
7.1 Summary 102
7.2 Outlook 103

A Adapting Analysis Tools Software to Interface with P∅D Reconstruction 111

List of Figures

1.1 The Standard Model of particle physics [1]. 2

1.2 Ratio of the background and geo-neutrino-subtracted $\bar{\nu}_e$ spectrum to the no-oscillation expectation as a function of L_0/E with $L_0 = 180\,\mathrm{km}$ [2]. 9

1.3 Allowed region for Δm^2_{21} and θ_{12} parameters from KamLAND and solar neutrino experiments. Side panels show $\Delta\chi^2$ for KamLAND (dashed), solar experiments (dotted) and combined (solid) [2]. 9

1.4 The 90% confidence region for $|\Delta m^2_{32}|$ and $\sin^2\theta_{23}$ parameters phase space given by measurement from different experiments. Figure adapted from [3]. . 10

1.5 90% confidence interval of the δ_{CP} measurement for the normal (black) and inverted (red) mass hierarchy. These values were obtained by the joint analysis of neutrino and antineutrino oscillations in both appearance and disappearance channels. Constraints for $\sin^2\theta_{13}$ from reactor measurements are implemented. Figure from [4]. 11

1.6 Significance at which Noνa disfavors the different values of δ_{CP} for the normal (blue) or inverted (red) hierarchy cases. The solid lines represent θ_{23} in the lower octant and dashed in the upper. Figure from [5]. 12

1.7 Total neutrino and antineutrino CC cross section divided by the neutrino energy as a function of energy for different interaction modes as predicted by NUANCE [6]. All data available up to 2012 is overlaid. Figures taken from [7]. 13

1.8 Feynman diagram to represent the CC quasi-elastic and NC elastic interaction of neutrino with a nucleon. 14
1.9 Feynman diagram to represent the CC single pion resonant interaction channel. 15
1.10 Final State Interactions inside a nucleus 17
1.12 Schematic figure to represent collinear and asymmetric decay of π^0 particle into two photons [8]. 18
1.11 Feynman diagrams to represent the two different modes of π^0 production via neutral current neutrino interaction on a nuclei. 18
1.13 A sample event display of Super-Kamiokande experiment showing Cherenkov radiation signature for a simulated event with μ^-, e^- and π^0 particle. 19
1.14 NC1π^0 cross section obtained from the re-ananlysis of Gargamelle data on propane+freone, corrected to a free nucleon. Figure from [9]. 20
1.15 Comparison of data and nominal T2K Monte Carlo for the distribution of NC1π^0 invariant mass [10]. 21

2.1 A schematic view of the T2K experiment. 23
2.2 An overview of the primary and secondary beamline of T2K. 24
2.3 Feynman diagram to represent the CC quasi-elastic and NC elastic interaction of neutrino with a nucleon. 25
2.4 The predicted off-axis neutrino (unoscillated) beam flux at ND280 and SK. . 26
2.5 The near detector complex of T2K. The bottom floor holds the on-axis detector (INGRID) while on top is the ND280 off-axis detector enclosed inside the magnet. 27
2.6 INGRID. 27
2.7 The ND280 off-axis detectors at T2K. 28
2.8 An event display of a (likely)DIS event in the tracker part of ND280 off-axis detectors consisting of three TPCs and two FGDs. 29
2.9 The Super-Kamiokande detector. 30

2.10 A schematic depicting connection of wavelength shifting (WLS) fiber connection to the multi-pixel photon counter (MPPC). Figure from [11]. 31
2.11 The Pi0 Detector (P0D) 33
2.12 P0D Reconstruction Algorithm 33

3.1 Distribution of π^0 interaction vertex position in the direction of beam. The histograms are area normalized. The excess of data seen in the first bin (most upstream position of ND280 detector) is due to the neutrino interactions on the surrounding environment not being simulated in the Monte Carlo. The fiducial distance (red line) cut removes these events. 37
3.2 Distribution of π^0 direction after all other cuts are applied. The histograms are area normalized. 37
3.3 Distribution of the number of μ decay cluster after all other cuts are applied. The histograms are area normalized. 38
3.4 2D distributions comparing allocation of charge in events. (a) Total charge vs. charge in 2 highest momentum (HM) shower particles. (b) Total charge vs. charge in other reconstructed particles (c) Total charge vs. charge not reconstructed as particles (d) Charge in other reconstructed particles vs. charge not reconstructed as particles 39
3.5 Distribution of the ratio of charge in two highest momentum showers to total charge in the event after all other cuts are applied. The histograms are area normalized. 39
3.6 kEM PID weight - kShower PID weight distribution after all other cuts are applied for (a) highest momentum shower particle for PØD water-in (b) highest momentum shower particle for PØD water-out (c) second highest momentum shower particle for PØD water-in (d) second highest momentum shower particle for PØD water-out. The plots are area normalized 40

3.7 (a) Distance between two showers using minimum hit distance as defined by previous analysis . This is dependent on individual hits. (b) Measurement could be incorrect due to presence of noise. (c) New definition using position of all charge weighted hits. 41

3.8 Shower particles which are spatially separated in 3D could still have an overlap in one 2D projection. Figure taken from [12]. 41

3.9 Distribution of minimum separation between two reconstructed shower particles after all other cuts are applied. The plots are area normalized. 42

3.10 Distribution of invariant mass of reconstructed π^0 particles after applying all selection cuts for Monte Carlo only. 43

3.11 Distribution of true incoming neutrino energy for events passing all selection cuts for Monte Carlo only. 43

3.12 π^0 kinematics phase space for signal events generated in true PØD fiducial volume (top) and signal events in selected sample (bottom) for PØD water-in (left) and water-out(right) configuration. 45

3.13 Ratio of signal events in the selected sample to all signal events generated in PØD fiducial volume in π^0 kinematics phase space for PØD water-in (left) and water-out (right) configuration. 46

3.14 True π^0 momentum distribution of signal events generated in PØD fiducial volume with π^0 direction $< 60^0$ to z axis (left) and the efficiency of selecting signal events (right) as a function of true pizero momentum for PØD water-in configuration. 46

3.15 True π^0 momentum distribution of signal events generated in PØD fiducial volume with π^0 direction $< 60^\circ$ to z axis (left) and the efficiency of selecting signal events (right) as a function of true pizero momentum for PØD water-out configuration. 47

3.16 True π^0 direction distribution of signal events generated in PØD fiducial volume (left) and the efficiency of selecting signal events (right) as a function of true pizero direction for PØD water-in configuration. 47
3.17 True π^0 direction distribution of signal events generated in PØD fiducial volume (left) and the efficiency of selecting signal events (right) as a function of true pizero direction for PØD water-out configuration. 48
3.18 Distribution of true simulated opening angle of π^0 decay particles w.r.t. π^0 momentum for signal events generated in PØD fiducial volume. High momentum π^0 particles are extremely forward going. 49
3.19 True Q^2 distribution of signal events generated in PØD fiducial volume with π^0 direction $< 60^0$ to z axis (left) and the efficiency of selecting signal events (right) as a function of true Q^2 for PØD water-in configuration. 49
3.20 True Q^2 distribution of signal events generated in PØD fiducial volume with π^0 direction $< 60^0$ to z axis (left) and the efficiency of selecting signal events (right) as a function of true Q^2 for PØD water-out configuration. 50
3.21 True W distribution of signal events generated in PØD fiducial volume with π^0 direction $< 60^0$ to z axis (left) and the efficiency of selecting signal events (right) as a function of true W for PØD water-in configuration. 50
3.22 True W distribution of signal events generated in PØD fiducial volume with π^0 direction $< 60^0$ to z axis (left) and the efficiency of selecting signal events (right) as a function of true W for PØD water-out configuration. 51
3.23 π^0 Invariant Mass distribution of signal events in selected sample, detailing contributions of true particles to reconstructed shower particles, for PØD water-in (left) and water-out (right) configurations. 52
3.24 True vs. reconstructed π^0 momentum for all selected signal (top) and for signal events where both reconstructed shower come from the same primary π^0 (bottom) for PØD water-in (left) and water-out (right) configurations. . . 53

3.25 Relative momentum resolution for all selected signal events for PØD water-in (left) and water-out (right) configurations. 53
3.26 True vs reconstructed π^0 direction for all selected signal events for PØD water-in (left) and water-out (right) configurations. 54
3.27 Relative π^0 direction resolution for all selected signal events before applying π^0 direction cut (top) and after applying the cut (bottom), for PØD water-in (left) and water-out (right) configurations. 54
3.28 Reconstructed π^0 invariant mass distribution of the background control sample. 55
3.29 Muon kinematics phase space for CC0π events in selected sample (top) and background control sample (bottom). CC0π events from background control sample are used to constrain the background in selected sample. 57
3.30 Muon kinematics phase space for CC1$\pi^{\pm}$ events in selected sample (top) and background control sample (bottom).CC1$\pi^{\pm}$ events from background control sample are used to constrain the background in selected sample. 58
3.31 True muon momentum vs. reconstructed π^0 invariant mass for CC0π events in selected sample (top) and background control sample (bottom). 59
3.32 True muon momentum vs. reconstructed π^0 invariant mass for CC1$\pi^{\pm}$ events in selected sample (top) and background control sample (bottom). 60

4.1 The effects of step size in estimating a normal distribution $N(0,1)$ using 500 steps of MCMC Chain. The top panel shows the optimal step size which quickly moves to a region of high probability and samples the stationary distribution. The middle panel has a small step size which cause too many steps to be accepted and takes a very long time to reach the stationary distribution. The last panel depicts the case of a large step size which fluctuates between the tails of the distribution leading to a poor acceptance rate. The dotted line shows the burn-in value. Figure is adapted from [13]. 63

5.1 Correlation Matrix for Resonance Parameters [14]. 71
5.2 Correlation Matrix for FSI Parameters [14]. 73
5.3 Correlation Matrix for Flux Parameters 75
5.4 Distribution of fraction of charge in two highest momentum shower particles from the total deposited charge for events that pass all cuts but fail the particle ID cut. This is used as a control sample to obtain priors on the systematics parameters for the cut on charge in shower particles. 77
5.5 Correlation matrix for charge in shower systematics parameters 77
5.6 First charge asymmetry distribution for events failing the the charge in shower particles cut and not applying any cut on particle ID weight, π^0 direction or shower separation distance for PØD water-in configuration. 79
5.7 Correlation Matrix obtained from the control sample fit of first charge asymmetry parameters in PØD water-in configuration. Parameter numbers correspond to the index in Table 5.13. 79
5.8 Effect of opening angle on Vertex Resolution 83
5.9 Distribution of number of events in PØD fiducial volume for 10,000 throws of $\Delta(\sigma_{x/y/z})$ for PØD water-in configuration. Nominal number of events for this Monte Carlo sample is 1363. 84
5.10 Distribution of number of events in PØD fiducial volume for 10,000 throws of $\Delta(\sigma_{x/y/z})$ for PØD water-out configuration. Nominal number of events for this Monte Carlo sample is 766. 85

6.1 Invariant mass distribution of events passing all selection cuts. 89
6.2 Invariant mass distribution of events failing shower separation cut but passing all other cuts. 90
6.3 Invariant mass distribution of events failing μ decay cluster cut but passing all other cuts. 90

6.4 Invariant mass distribution of events failing μ decay cluster and shower separation cut but passing all other cuts. 91

6.5 Comparison of prior and posterior of cross section and FSI parameters after the analysis fit.The one sigma error on the priors are highlighted by red boxes. The mean and the rms of the posterior histogram is plotted on top for comparison. The X axis labels all individual parameters. 92

6.6 Comparison of prior and posterior of flux parameters after the analysis fit. The one sigma error on the priors are highlighted by red boxes. The mean and the rms of the posterior histogram is plotted on top for comparison. The numbers on X axis correspond to the order of parameters listed in Table 5.10. 92

6.7 Comparison of prior and posterior of detector systematics parameters after the analysis fit.The one sigma error on the priors are highlighted by red boxes. The mean and the rms of the posterior histogram is plotted on top for comparison. 93

6.8 Comparison of prior and posterior of signal weight parameters for events not on water after the analysis fit. The one sigma error on the priors are highlighted by red boxes. The mean and the rms of the posterior histogram is plotted on top for comparison. The X axis labels the invariant mass bin that the parameter is used to re-weight. 93

6.9 Comparison of prior and posterior of signal weight parameters for events on water after the analysis fit.The one sigma error on the priors are highlighted by red boxes. The mean and the rms of the posterior histogram is plotted on top for comparison.The X axis labels the invariant mass bin that the parameter is used to re-weight. 94

6.10 Comparison of number of NC1π^0 events on water predicted by the nominal NEUT Monte Carlo (blue histogram) with the best fit number of NC1π^0 events (red points) from the fit in that bin. The best-fit is calculated by using the mean of the 1D posterior of the signal weight on-water parameters multiplied by the predicted number of events in the bin by the nominal Monte Carlo. . 94

6.11 Comparison of number of NC1π^0 events not on water predicted by the nominal NEUT Monte Carlo (blue histogram) with the best fit number of NC1π^0 events (red points) from the fit in that bin. The best-fit is calculated by using the mean of the 1D posterior of the signal weight not-water parameters multiplied by the predicted number of events in the bin by the nominal Monte Carlo. . 95

6.12 Number of signal events on water for invariant mass of 0 - 500 MeV marginalized over all nuisance parameters. The red line shows the nominal Monte Carlo prediction of 167 events. 96

6.13 Posterior predictive plots for the selected sample for PØD water-in configuration. The black line represents the POT normalized nominal Monte Carlo distribution and the red line is the data. The blue density region shows 5000 random throws from the posteriors of all fit parameters. 97

6.14 Posterior predictive plots for the selected sample for PØD water-out configuration. The black line represents the POT normalized nominal Monte Carlo distribution and the red line is the data. The blue density region shows 5000 random throws from the posteriors of all fit parameters. 97

6.15 Posterior predictive plots for the selected sample events that fail the shower separation cut for PØD water-in configuration. The black line represents the POT normalized nominal Monte Carlo distribution and the red line is the data. The blue density region shows 5000 random throws from the posteriors of all fit parameters. 98

6.16 Posterior predictive plots for the selected sample events that fail the shower separation cut for PØD water-out configuration. The black line represents the POT normalized nominal Monte Carlo distribution and the red line is the data. The blue density region shows 5000 random throws from the posteriors of all fit parameters. 98

6.17 Posterior predictive plots for the background control sample for PØD water-in configuration. The black line represents the POT normalized nominal Monte Carlo distribution and the red line is the data. The blue density region shows 5000 random throws from the posteriors of all fit parameters. 99

6.18 Posterior predictive plots for the background control sample for PØD water-out configuration. The black line represents the POT normalized nominal Monte Carlo distribution and the red line is the data. The blue density region shows 5000 random throws from the posteriors of all fit parameters. 99

6.19 Posterior predictive plots for the background control sample events that fail the shower separation cut for PØD water-in configuration. The black line represents the POT normalized nominal Monte Carlo distribution and the red line is the data. The blue density region shows 5000 random throws from the posteriors of all fit parameters. 100

6.20 Posterior predictive plots for the background control sample events that fail the shower separation cut for PØD water-out configuration. The black line represents the POT normalized nominal Monte Carlo distribution and the red line is the data. The blue density region shows 5000 random throws from the posteriors of all fit parameters. 100

6.21 A distribution of χ^2 data vs χ^2 fake data. The fake data is obtained by the poisson throws of the Monte Carlo prediction obtained by the sampling of posterior distributions of the parameters. χ^2 measures the poisson log-likelihood between this Monte Carlo prediction and data or fake data. The line represents χ^2 data = χ^2 fake data. p-value is the fraction of points below the line. 101

A.1 Parallel architecture of data storage in PØDRecon. The different colored arrows show the chain of pointers that is selected contingent on the reconstruction algorithms that is picked by the user. 112

A.2 Schematic depiction of hierarchical structure of classes in HighLAND software package prior to modifications to make it compatible with PØDRecon. 112

A.3 Modified structure of classes in HighLAND software that support interfacing with PØD reconstruction. 113

List of Tables

1.1 Current best fit values of neutrino mixing angles and the mass differences squared [15]. 7

1.2 Measurements of ratio of cross section of NC/CC channel using data from bubble chamber(ANL, Gargamelle) and spark chamber (BNL, CERN PS) experiments. $N(n, p)$ runs over interactions on both neutron and proton. The ANL results were reanalyzed with a better understanding of neutron background whereas BNL results were updated after considering multi-π background. The presented data from Gargamelle is also reanalyzed and is corrected for free nucleon. NUANCE provides the Monte Carlo prediction for free nucleon case. Table is adapted from [9]. 19

1.3 Measurement of NC/CC ratio by K2K (2005) and SciBooNE (2010) experiments. NEUT predicts a ratio of 0.065 for K2K and 0.068 for SciBooNE energies. K2K has the only measurement on water besides T2K. 20

1.4 Absolute cross sections for the NC1π^0 interaction on mineral oil by MiniBooNE experiment [16]. 20

1.5 NC1π^0 events in PØD in the previous T2K analysis [10]. 21

2.1 PØD Fiducial Volume in Global ND280 Coordinates 32

3.1 Proton on Target (POTs) collected by T2K data runs in neutrino mode that are used for this analysis. Data for Run 5 - Run 7 was taken in antineutrino mode which is not analyzed for this analysis. 42
3.2 Number of NC1π^0 events generated by Monte Carlo in the topology described in Column 1. 44
3.3 Number of NC1π^0 events with reconstructed topology described in Column 1. 44
3.4 Percentage breakdown of background events in the selected sample (SS) and background control sample (BCS) for PØD water-in and water-out configuration. CC 0π is the largest background in the SS while CC$\pi^{\pm}$ is the largest fraction in the BCS. Other event topology fractions are relatively equal. . . . 56

4.1 π^0 invariant mass bins in which the fit is performed. 66

5.1 Priors on CCQE parameters. Values are normalized with respect to NEUT Nominal. Absolute values are provided in brackets. 69
5.2 Priors on 2p2h shape parameters. 70
5.3 Priors on resonance interaction parameters. 70
5.4 Tuning applied to CC Coherent events as a function of pion energy. 71
5.5 Priors on 1 π coherent parameters. 71
5.6 Priors on ν_e interaction parameters. 72
5.7 Priors on NC1γ, NC Other and CC other interaction parameters. 72
5.8 Priors on pion final state interaction parameters. 73
5.9 Incoming neutrino energy bins for flux reweighting 74
5.10 Priors on T2K flux parameters. 74
5.11 Priors on PØD mass systematics parameters taken from [12] 76
5.12 Priors on charge ratio scale parameters for the analysis fit. 76

5.13 Priors on the charge asymmetry parameters for PID systematics in the analysis fit. 12 sets of parameters listed in this table are used to account for three separate cluster categories, two charge asymmetry variables and two PØD configurations 80
5.14 Priors on shower separation scale parameters for the analysis fit. 80
5.15 Efficiency of muon decay reconstruction measured using a sample of stopping muons [12]. 81
5.16 Priors on muon decay efficiency and fake rate parameters for the PØD water-in and water-out samples. 81
5.17 NC1π^0 vertex resolution in PØD [12]. 82
5.18 A Gaussian fit to data and Monte Carlo selected signal samples for PØD water-in configuration. The difference in means can be used as an approximation of energy scale difference between data and Monte Carlo. 86
5.19 A Gaussian fit to data and Monte Carlo selected signal samples for PØD water-out configuration.The difference in means can be used as an approximation of energy scale difference between data and Monte Carlo. 86

Acknowledgements

This thesis was a work of love and labor of many years during which I was supported, advised and inspired by very many people around the globe. First and foremost, I would like to acknowledge my adviser Chang Kee Jung, whose wise words, mostly delivered in the form of anecdotes and stories, informed many decisions academically and otherwise. My biggest appreciation for Chang Kee arises from the absolute freedom he provided to me to speak my mind on all issues under the sun. I had the complete confidence that he will always have my back. At Stony Brook, I worked most closely with Clark McGrew. Over the years, I managed to imbibe a small fraction of his excellent coding and physics skills which forms the majority of my graduate school toolbox. Mike Wilking was the mentor I never had! Even though we overlapped at Stony Brook for multiple years, we ended up talking to each other only during our trips to Japan. His physics undertakings have been a constant inspiration which stimulate creative thinking while tackling problems in science. As for the problems of the society, we often agreed on a similar path until the very end where we diverged drastically. When Cris joined Stony Brook, I never imagined the extent to which he would impact my analysis, as he was going to work on very different problems. Fast forward to the end, one of the biggest indicator of what ended up in my analysis or thesis is whether I discussed it with Cris in the long car rides we shared on our way home. He had really insightful inputs on all things ranging from estimating systematics to job talks. All this apart from the wonderful friendship we shared which included lots of food, wine, conversations and watering of the plants. Gabriel and Xiaoyue provided the best combination of people to have in my cohort at NN Group. Xiaoyue always provided answers for all my questions, irrespective of the time of the day, geographical location or the stupidity level while Gabriel would always volunteer to work with you on the black board to figure out random puzzles or hairy physics problems. While they both inspired me to do good science, Xiaoyue's sincerity motivated me to work hard while Gabriel helped lighten the stress with his ever delightful company. It also worked vice versa. Jay, Yue and Neha provided the remarkable camaraderie required to deal with the woes of working on PØD. Jose, Guang and Kevin contributed to making my time spent at NN Group fun and fruitful.

Being a member of T2K Collaboration presented the amazing opportunity to learn and interact with a wide scientific community. Helen, Kendall, Vittorio and Morgan were conveners and mentors that provided guidance, encouragement and support throughout the journey. The line between research and revelry truly became blurred when I was hanging out with Clarence, Callum, Leila, Thomas, Jackie, Elder, Corina, Sophie Berkman, Sophie King, Luke, Kirsty, Paula, Minoo, Stephen Dolan and Lukas in Japan. I received a lot of help from Anselmo, Sasha, Celeste, Matt Lawe, Dan, Enrico, Patrick Dunne and Patrick Stowell.

The administrative staff at Stony Brook including Tracy Hillenbrand, Gloria Clivilles-Ramos, Charise Kelly, Donald Sheehan and Sara Lutterbie made the tiresome paperwork incredibly smooth. They were like magicians who found solutions to all our non-academic woes. Ayako Kikuchi was a one stop answer for any and all problems in Japan, which she

graciously helped us resolve. I am glad, I also got to know her as a friend during my time in Japan.

Life at Stony Brook can be cold and lonely. However, the warmth of love provided by the friends I had on campus, made my stay very happy and gratifying. Bertus and Abhishodh truly made our shared apartment a home. There was always love, laughter, food and beer available in abundance. Naveen and Mat completed our Physics family which mostly discussed politics and *one other topic* with increasing passion and cadence as the night wore on. Mike, Anusha and Shikha formed happy extensions of this clan. Vinyas, Sayali, Ali and Pushkar provided a sudden whirlwind of friendship for a brief three month span at the end of which they left Stony Brook for sunnier lands, but not before we had formed bonds which would stretch to accommodate the space and time differences between the two US coasts.

Jinee and Sangay were merely phone numbers on a slip of paper given by my parents when I moved to this faraway land. From being the first to introduce me to the wonders of NYC, providing lots of home cooked food and being the familial support structure during graduate school, they've been a consistent source of love and friendship.

The heartache I felt at the thought of leaving behind everything familiar to join graduate school was soothed a bit by the fact that Rajita was moving to Boston when I came to Stony Brook. She would have to substitute for all things home : family, friends, lover, mentors and community. In the course of time, she was all this and much more. She was the seed of home in US, who helped me establish new roots and relations or wait for the old ones to join in the new land.

Sadhna Masi, Kabir and Kislay were true, constant cheerleaders throughout my life. It's been wonderful growing up with Kislay and watching Kabir grow. Scary, too. Kislay's creativeness, especially in inventing ways as kids to blame everything on me, helped me sharpen my creative edge too. Papa is a true academic dad. Though not quite sure of my exact birth date, he was exceptionally concerned about academic progress which wasn't restricted to school grades. Curiosity, courage and single-minded pursuit, especially in the academic context, were instilled in me by him. Ma's love is quintessentially motherly at times, when she worries about my eating and sleeping habits while it is fiercely feminist at other occasions when she concerns herself with cases of gender based power abuse in academia. I specially enjoy it when her two sides get conflicted with each other. Having a feminist, scientist mother has been a constant source of inspiration and exasperation in life. I'm fortunate to know her and love her in all her incarnations.

Chirag and I grew up together from classical mechanics to quantum mechanics and being concerned with high school politics to world politics. It's been a long and joyful adventure. He's a person of few words and prefers even fewer words spoken about him, so I'll restrict myself to the last six months of thesis writing. He tirelessly ensured that I always had enough water, food and Margaritas (in that order). To him I can only say, thank you *for existing*!

Chapter 1

Introduction

"And those who were seen dancing were thought to be insane by those who could not hear the music." - Friedrich Nietzsche

The history of the Standard Model, its triumphs and failures hold important lessons for particle physicsists. The Standard Model has successfully described the fundamental particles and their interactions for nearly five decades. Neutrinos in the Standard Model are massless particles. However, with experimental verification of neutrino oscillation, it was established that neutrinos have non-zero mass. Detecting neutrinos is a challenging task due to the fact that they only interact via gravity and weak force. The long distance covered by neutrino experiments from detecting a single neutrino to making precision measurements of the oscillation parameters is inspiring. The exciting journey of the prediction and measurement of neutrino oscillation is detailed in Section 1.2. The last section of this chapter is devoted to the discussion of different modes via which neutrinos interact with a target nucleus. It focuses on the neutral current single π^0 interaction channel which is the signal channel for this analysis.

1.1 The Standard Model

The Standard Model of particle physics describes the elementary particles and their interactions caused by the fundamental forces. The half integer spin particles, fermions, make up the matter, while the integer spin particles, gauge bosons are the carrier particles of fundamental forces. Fermions are subdivided into leptons and quarks, each of which come in three generations. The quarks carrying fractional electric charge and an additional color charge must combine to from integer, colorless particles called hadrons. Hadrons can be formed by a combination of three quarks knowns as baryons, such as protons (uud) or neutrons

(udd) or a quark and an antiquark, knows as mesons. The leptons come in both charged and neutral varieties. The e^-, μ^- and τ^- have a negative electric charge, while their neutrino counterparts ν_e, ν_μ and ν_τ are neutral. Important characteristics of these elementary particles is shown in Figure 1.1.

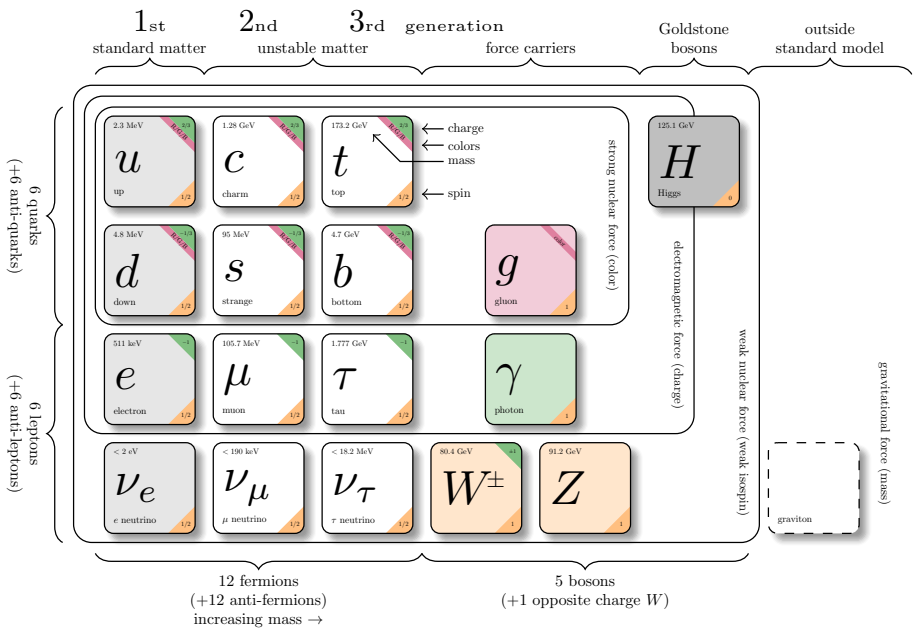

Figure 1.1: The Standard Model of particle physics [1].

Gluons mediate the strong force, which binds the quarks together whereas photons are the carriers of the electromagnetic force. $W^\pm$ and Z bosons are the mediators of the weak force. The quarks can interact with all three forces, while the charged leptons interact via the electromagnetic and the weak force. Neutrinos being neutral can only participate in weak interactions. When a weak interaction happens via $W^\pm$ gauge boson, an exchange of charge occurs between interacting particles. These are known as charged current interactions. The Z bosons can also mediate weak interactions which are called neutral current interactions.

The π^0 particle is a meson which forms the main signal of this analysis. It is formed from the quantum superposition of two combinations of quark and antiquark particles.

$$\pi^0 = \frac{u\bar{u} - d\bar{d}}{2} \tag{1.1}$$

It has a mass of 134.9770 ± 0.0005 MeV/c^2 and a mean lifetime of $(8.52 \pm 0.18) \times 10^{-17}$ s [15]. It decays into two photons with a branching ratio of $98.82 \pm 0.03\%$ [15].

The Standard Model developed in the early 1970s has successfully explained numerous phenomena and predicted new particles, and their properties which were verified by experimental measurements. The Higgs boson, discovered in 2012 is the latest proof of the success of Standard Model in explaining the world of fundamental particle physics. While the discovery of the Higgs explained the mechanism by which the elementary fermions and $W^\pm$/Z

bosons obtain their mass, the absolute value of these masses is not inherently predicted by the Standard Model. They have been measured by experimental observations and are treated as external inputs to the model. In fact, the neutrinos as defined in the Standard Model are massless particles. However, as detailed in the next section, the experimental verification of neutrino oscillation proved that neutrinos have non-zero mass.

1.2 Neutrino Oscillation

Neutrinos were introduced by W.E. Pauli in 1930 as a "*desperate remedy*" to explain the continuous energy spectrum of electrons emitted in β decay. Emission of a light, electrically neutral particle with spin 1/2 that escaped detection, but carried away energy could explain the continuous spectrum without violating the conservation of the angular momentum and energy. In 1934, Enrico Fermi published the quantitative theory of β decay and called the new postulated particle a 'neutrino'. The same year, Bethe and Peierls presented the first calculation of neutrino-nucleus interaction cross section, obtaining a value of less than 10^{-44} cm^2 suggesting that "*there is no practically possible way of observing the neutrino*". However, in 1956 Cowan and Reines detected the neutrinos for the first time using the newly invented nuclear reactors as an intense source of (anti)neutrino. They captured the (anti)neutrino in a large tank of liquid scintillator using the inverse β decay process given by Eq. 1.2.

$$\bar{\nu} + p \rightarrow e^+ + n \tag{1.2}$$

In 1962 L. M. Lederman, M. Schwartz and J. Steinberger proved the existence of the muon neutrino. They demonstrated the presence of muon tracks produced by the interactions of neutrinos emitted in a pion decay, using a 10-ton spark chamber at the new Brookhaven Alternating Gradient Synchrotron. After the discovery of tau particle in 1975, an associated tau neutrino was also expected. The first direct observation of tau neutrino interactions was made by DONUT(*Direct Observation of NU Tau*) collaboration in 2000 [17].

In the late 1960's, R. Davis and collaborators constructed an experiment to collect and count the neutrinos emitted in nuclear fusion reactions taking place in the Sun at the Homestake Mine in South Dakota. The measured neutrino flux was 1/3 of the expected flux from the theoretical calculations. This was known as the "solar neutrino problem". B. Pontecorvo had proposed the idea of neutrino oscillation in late 1950s but at that time it was not well accepted. However, the deficit in the solar neutrino flux was confirmed by Kamiokande experiment in 1980s followed by GALLEX/GNO [18] and SAGE [19] in 1990. In 2002, SNO collaboration made the first model independent measurement of the solar neutrino flux [20]. It measured a $5.3\,\sigma$ evidence of non-ν_e component of the ^{8}B solar flux which provided a strong evidence for flavor change of neutrinos.

In 1998, Super-Kamiokande experiment measured a difference in the number of upward and downward going muon neutrinos produced by the interaction of cosmic rays with the atmosphere [21]. For the neutrinos produced in the atmosphere, the downward going neutrinos travel a distance of $20 \sim 50$ km as compared to the upward going neutrinos that typically pass through the Earth to travel a distance of $1000 \sim 13,000$ km. If there was no neutrino oscillation, the flux for downward and upward going neutrinos would be equal

as the decrease in the flux due to longer distance is nullified by the larger available surface area of the Earth. However, Super-Kamiokande measured an upward going flux of muon neutrinos as half of the downward going flux. Results from Super-Kamiokande and SNO irrevocably established the neutrino oscillation theory.

1.2.1 Theoretical formulation

Neutrinos come in three flavors ν_e, ν_μ and ν_τ. While they can only be observed in their flavor eigenstate, they propagate in their mass eigenstates in vacuum. Existence of additional light neutrino species is not prohibited but constrained by the measurement of decay width of Z boson at LEP and SLC electron-positron colliders which gives $N_\nu = 2.984 \pm 0.008$ [22]. This measurement allows for very heavy neutrino species with mass larger than half of Z boson mass or light neutrino species that do not interact via the Standard Model forces which are known as sterile neutrinos. Assuming no sterile neutrino, the mixing of the flavor and mass eigenstates of neutrinos is given by Eq. 1.3.

$$|\nu_\alpha\rangle = \sum_{i=1}^{n=3} U^*_{\alpha i}|\nu_i\rangle \qquad \alpha = e, \mu, \tau \tag{1.3}$$

where U represents the unitary PMNS matrix named after B. Pontecorvo, Z. Maki, M. Nakagawa and S. Sakata. Maki, Nakagawa and Sakata were the first to introduce this matrix for two generations of neutrino oscillation which was first predicted by Pontecorvo. This matrix can be parametrized using three mixing angles θ_{12}, θ_{13} and θ_{23} and a CP-violating phase δ_{CP}. If the neutrinos are Majorana particles, two additional phases α_{13} and α_{23} have to be added to this matrix.

$$\begin{pmatrix} \nu_e \\ \nu_\mu \\ \nu_\tau \end{pmatrix} = \begin{pmatrix} U_{e1} & U_{e2} & U_{e3} \\ U_{\mu 1} & U_{\mu 2} & U_{\mu 3} \\ U_{\tau 1} & U_{\tau 2} & U_{\tau 3} \end{pmatrix} \cdot \begin{pmatrix} \nu_1 \\ \nu_2 \\ \nu_3 \end{pmatrix} \tag{1.4}$$

where:

$$
\begin{aligned}
U &= \begin{pmatrix} c_{12}c_{13} & s_{12}c_{13} & s_{13}e^{-i\delta_{CP}} \\ -s_{12}c_{23} - c_{12}s_{23}s_{13}e^{i\delta_{CP}} & c_{12}c_{23} - s_{12}s_{23}s_{13}e^{i\delta_{CP}} & s_{23}c_{13} \\ s_{12}s_{23} - c_{12}c_{23}s_{13}e^{i\delta_{CP}} & -c_{12}s_{23} - s_{12}c_{23}s_{13}e^{i\delta_{CP}} & c_{23}c_{13} \end{pmatrix} \cdot \\
&\cdot \begin{pmatrix} 1 & 0 & 0 \\ 0 & e^{i\alpha_{21}/2} & 0 \\ 0 & 0 & e^{i\alpha_{31}/2} \end{pmatrix} \\
&= \begin{pmatrix} 1 & 0 & 0 \\ 0 & c_{23} & s_{23} \\ 0 & -s_{23} & c_{23} \end{pmatrix} \begin{pmatrix} c_{13} & 0 & s_{13}e^{-i\delta_{CP}} \\ 0 & 1 & 0 \\ -s_{13}e^{-i\delta_{CP}} & 0 & c_{13} \end{pmatrix} \begin{pmatrix} c_{12} & s_{12} & 0 \\ -s_{12} & c_{12} & 0 \\ 0 & 0 & 1 \end{pmatrix} \cdot \\
&\cdot \begin{pmatrix} 1 & 0 & 0 \\ 0 & e^{i\alpha_{21}/2} & 0 \\ 0 & 0 & e^{i\alpha_{31}/2} \end{pmatrix}
\end{aligned} \tag{1.5}
$$

where $c_{ij} = \cos\theta_{ij}$ and $s_{ij} = \sin\theta_{ij}$.
In vacuum, the propagation of a neutrino in a mass eigenstate, is given by:

$$|\nu_i(t)\rangle = e^{-\imath(E_i t - \vec{p}_i \cdot \vec{x})}|\nu_i(0)\rangle \tag{1.6}$$

where E_i is the energy, $\vec{p}_i$ is the three momentum and $\vec{x}$ is the distance traveled in time t. In the relativistic limit, $p_i \gg m_i$,

$$E_i = \sqrt{p_i^2 + m_i^2} \simeq p_i + \frac{m_i^2}{2p_i} \approx E + \frac{m_i^2}{2E} \tag{1.7}$$

As the mass of the neutrino is negligible, we can put $p \simeq E$ and assuming it travels at the speed of light $t \simeq L$ in natural units. Dropping the phase factors, Eq. 1.6 becomes:

$$|\nu_i(t)\rangle = e^{-\imath m_i^2 \frac{L}{2E}}|\nu_i(0)\rangle \tag{1.8}$$

Substituting Eq. 1.8 in Eq. 1.3, we get:

$$|\nu_\alpha(t)\rangle = \sum_{i=1}^{n=3} U_{\alpha i}^* e^{-\imath m_i^2 \frac{L}{2E}}|\nu_i(0)\rangle \tag{1.9}$$

As U is an unitary matrix, 1.3 can be inverted to express mass eigenstates in terms of flavor eigenstates, giving:

$$|\nu_\alpha(t)\rangle = \sum_\beta \sum_{i=1}^{n=3} U^*_{\alpha i} e^{-\imath m_i^2 \frac{L}{2E}} U_{\beta i} |\nu_\beta\rangle \tag{1.10}$$

Thus, after time t, the probability of a neutrino of flavor α being observed in flavor β is given by:

$$P_{\alpha\to\beta} = |\langle\nu_\beta|\nu_\alpha(t)\rangle|^2 = \sum_i U^*_{\alpha i} U_{\beta i} U_{\alpha j} U^*_{\beta j} e^{-\imath \Delta m^2_{ij} \frac{L}{2E}} \tag{1.11}$$

or equivalently,

$$\begin{aligned} P_{\alpha\to\beta} = \delta_{\alpha\beta} - 4\sum_{i>j} Re\Big(U^*_{\alpha i} U_{\beta i} U_{\alpha j} U^*_{\beta j}\Big) \sin^2\left(\frac{\Delta m^2_{ij} L}{4E}\right) \\ +2\sum_{i>j} Im\Big(U^*_{\alpha i} U_{\beta i} U_{\alpha j} U^*_{\beta j}\Big) \sin\left(\frac{\Delta m^2_{ij} L}{2E}\right) \end{aligned} \tag{1.12}$$

where $\Delta m^2_{ij} \equiv m_i^2 - m_j^2$ with $i, j = 1, 2, 3$.
From Eq. 1.11, it can be concluded that an evidence of neutrino oscillation proves non-zero mass of neutrino. The calculation of antineutrino oscillation probability yields the same result as Eq. 1.12 but with a (-) sign in front of the third term. Hence by measuring any asymmetry between neutrino and anti-neutrino oscillation probabilities, δ_{CP} phase can be estimated.

As mentioned previously, this is just the probability of neutrino oscillation in vacuum. When neutrinos propagate through matter, presence of electrons and nucleons in the matter impacts these oscillation probabilities. $\overset{(-)}{\nu}_e$ can interact via both neutral and charged currents due to the presence of e^- whereas $\overset{(-)}{\nu}_\mu$ and $\overset{(-)}{\nu}_\tau$ only interact via neutral current with matter. These differences in the neutrino interactions leading to changes in neutrino oscillation probabilities is known as matter effect or MSW effect after Mikheyev, Smirnov and Wolfenstein. The matter effect can be parameterized as a perturbation to the vacuum Hamiltonian to account for the excess potential V_e caused by charged currents for $\overset{(-)}{\nu}_e$. The potential due to neutral current can be ignored as it is the same for all flavors.

$$V_e = \pm\sqrt{2} G_F N_e \tag{1.13}$$

where (+) is applicable to ν_e, (-) for $\bar{\nu}_e$, G_F is the Fermi constant and N_e is the number of electrons in the medium. A complete treatment of the impact of matter effect on neutrino oscillation can be found in [23]. However, it is instructive to note that the matter effect makes the neutrino oscillation probability sensitive to the sign of mass splitting of neutrinos and not just the square of mass differences. Moreover, the matter effect impacts the neutrino and antineutrino oscillations differently, leading to a measured difference in the oscillation probabilities which is not due to lepton sector CP violation. It should also be noted that the Majorana phases do not affect the probabilities of neutrino oscillation.

1.2.2 Experimental measurements

Over the years, a wide variety of neutrino oscillation experiments have measured the parameters of the PMNS matrix and the neutrino mass differences. The current best knowledge of all these parameters is summarized in Table 1.1.

Parameter	best-fit	3 σ CL
$\sin^2\theta_{12}$	0.297	[0.250 - 0.354]
$\sin^2\theta_{23}$ [Normal hierarchy]	0.425	[0.381 - 0.615]
$\sin^2\theta_{23}$ [Inverted hierarchy]	0.589	[0.384 - 0.636]
$\sin^2\theta_{13}$ [Normal hierarchy]	0.0215	[0.0190 - 0.0240]
$\sin^2\theta_{13}$ [Inverted hierarchy]	0.0216	[0.0190 - 0.0242]
Δm^2_{21}	7.37 [10^{-5}eV^2]	[6.93 - 7.96] [10^{-5}eV^2]
$\Delta m^2_{31(23)}$ [Normal hierarchy]	2.56 [10^{-3}eV^2]	[2.45 - 2.69] [10^{-3}eV^2]
$\Delta m^2_{31(23)}$ [Inverted hierarchy]	2.54 [10^{-3}eV^2]	[2.42 - 2.66] [10^{-3}eV^2]
δ_{CP}/π [Normal hierarchy]	1.38	2σ : (1.0 - 1.9)
δ_{CP}/π [Inverted hierarchy]	1.31	2σ : (0.92 - 1.88)

Table 1.1: Current best fit values of neutrino mixing angles and the mass differences squared [15].

The δ_{CP} and the ordering of mass eigenstates of neutrino are still unknown. The hypothesis that $m_1 < m_2 < m_3$ is known as the normal hierarchy (NH) whereas $m_3 < m_1 < m_2$ is termed as inverted hierarchy (IH).

Neutrino oscillation experiments study neutrinos and(/or) antineutrinos produced by the Sun (solar neutrinos), cosmic-ray interactions with the atmosphere (atmospheric neutrinos), nuclear reactors (reactor neutrinos) or proton accelerator (accelerator neutrinos). Depending on the source, its energy spectra and the particular flavor oscillation, these experiments are sensitive to different parts of the PMNS matrix. A large number of experiments have contributed extensively to the current understanding of neutrino oscillation but due to the limited scope of this document, only the leading results from chose experiments would be highlighted in the following sections. A detailed review is provided by the Particle Data Group [15].

Measurement of Δm^2_{21} and θ_{12} parameters

ν_e produced by the nuclear reactions in the core of the sun has an energy of $\sim \mathcal{O}(1)$ MeV. Solar neutrino experiments measure the survival probability ($P(\nu_e \to \nu_e)$) of these neutrinos when they are detected on Earth. Aside from neutrino oscillation, this probability is also affected by the matter affect mentioned in Section 1.2.1 as these neutrinos traverse the high density core of the sun. The Sudbury Neutrino Observatory (SNO) located in Ontario, Canada detects solar neutrinos through their interactions on heavy water (D_2O). It is spherical detector with a radius of 6 m and uses 9,456 photomultiplier tubes (PMTs) to capture the Cherenkov radiation emitted from neutrino interactions. SNO measures solar

neutrinos through the following interaction channels:

$$\begin{aligned} \nu_e + d &\rightarrow p + p + e^-(CC) \\ \nu_\alpha + d &\rightarrow p + n + \nu_\alpha(NC) \\ \nu_\alpha + e^- &\rightarrow \nu_\alpha + e^-(ES) \end{aligned} \tag{1.14}$$

where $\alpha = e^-, \mu^-, \tau^-$ and ES stands for elastic scattering.

As shown in Eq. 1.14, CC interactions only occur for ν_e whereas NC and ES channels are equally available for all flavors of neutrino. SNO measured the flux of neutrinos observed through CC channels (ϕ_{CC}), NC channel (ϕ_{NC}) and ES channel (ϕ_{ES}) as below [24]:

$$\begin{aligned} (\phi_{CC}) &= 1.68^{+0.06}_{-0.06}(\text{stat.})^{+0.08}_{-0.09}(\text{syst.}) \times 10^6 \text{cm}^{-2}\text{s}^{-1} \\ (\phi_{NC}) &= 2.35^{+0.22}_{-0.22}(\text{stat.})^{+0.15}_{-0.15}(\text{syst.}) \times 10^6 \text{cm}^{-2}\text{s}^{-1} \\ (\phi_{ES}) &= 4.94^{+0.21}_{-0.21}(\text{stat.})^{+0.38}_{-0.34}(\text{syst.}) \times 10^6 \text{cm}^{-2}\text{s}^{-1} \end{aligned} \tag{1.15}$$

They compared the fluxes listed in Eq. 1.15 to calculate a flux for electron neutrino (ϕ_e) and for non-electron components ($\phi_{\mu\tau}$). Measurement of $\phi_{\mu\tau} = 3.26^{+0.25}_{-0.25}(\text{stat.})^{+0.40}_{-0.35}(\text{syst.}) \times 10^6 \text{cm}^{-2}\text{s}^{-1}$ provides larger than 5σ evidence of solar ν_e flavor change. The ν_e survival probability is dependent mainly on Δm^2_{21} and θ_{12} of the PMNS matrix with very weak dependence on θ_{13}. Using these values SNO measured the best-fit value of $\Delta m^2_{21} = 4.57 \times 10^{-5}\text{eV}^2$ and $\tan^2\theta_{12} = 0.447$ [25].

However, a much tighter constraints on the values of Δm^2_{21} and θ_{12} of the PMNS matrix can be obtained by combining the results from SNO with the Kamioka Liquid Scintillator Antineutrino Detector (KamLAND). KamLAND detects the $\bar{\nu}_e$ emitted from 55 commercial nuclear power units located at varying distances from the detector. It is a balloon shaped detector filled with 1 kton of liquid scintillator with 1,879 PMTs to capture the scintillation light located in Kamioka, Japan. It also has a 3.2 kton water Cherenkov outer detector to veto cosmic ray muons. Reactor neutrino experiments capture the $\bar{\nu}_e$ through inverse beta decay and study the survival probability of reactor $\bar{\nu}_e$ ($P(\bar{\nu}_e \rightarrow \bar{\nu}_e)$). KamLAND's flux averaged baseline of 180 km makes it sensitive to Δm^2_{21} and θ_{12} whereas a short baseline distance of $\sim$ 1km make reactor experiments like Daya Bay, Double Chooz and RENO sensitive to Δm^2_{31} and θ_{13}. In December 2002, KamLAND's first result with 162 ton-yr exposure reported [26]:

$$\frac{N_{obs} - N_{bkg}}{N_{NoOsc}} = 0.611 \pm 0.085(\text{stat.}) \pm 0.041(\text{syst.}) \tag{1.16}$$

where N_{obs} is the number of observed data events, N_{bkg} is the number of background events and N_{NoOsc} is the number of expected events in case of no $\bar{\nu}_e$ oscillations.

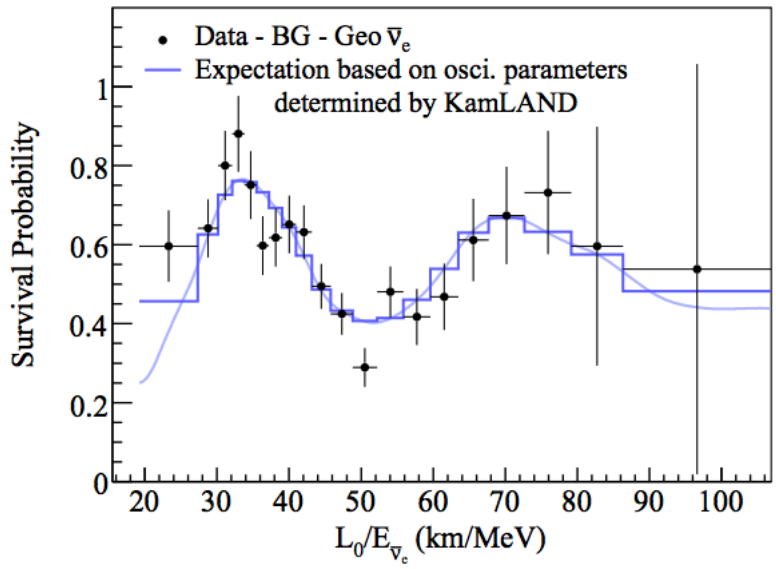

Figure 1.2: Ratio of the background and geo-neutrino-subtracted $\bar{\nu}_e$ spectrum to the no-oscillation expectation as a function of L_0/E with $L_0 = 180\,\mathrm{km}$ [2].

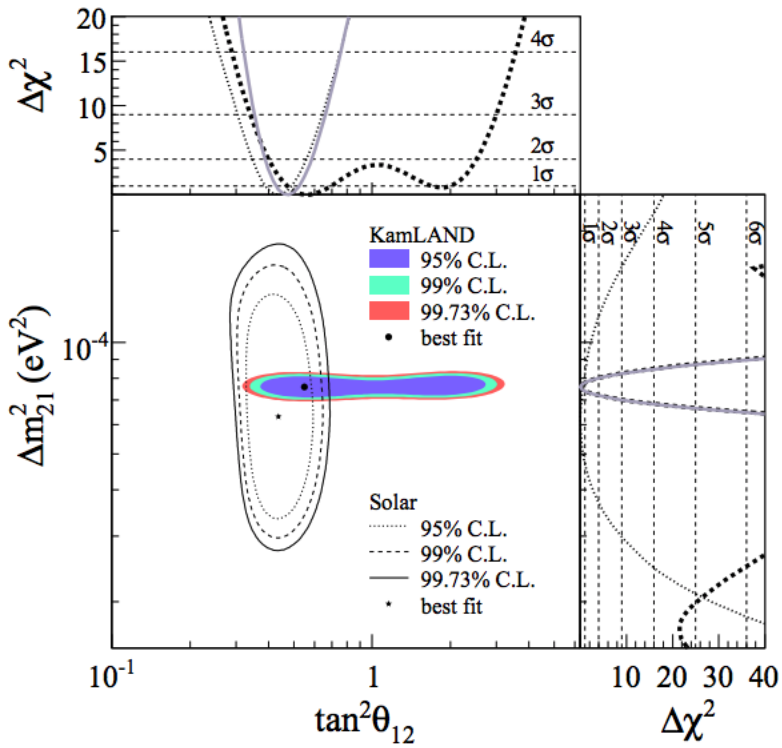

Figure 1.3: Allowed region for Δm^2_{21} and θ_{12} parameters from KamLAND and solar neutrino experiments. Side panels show $\Delta\chi^2$ for KamLAND (dashed), solar experiments (dotted) and combined (solid) [2].

Measurement of $|\Delta m^2_{32}|$ and θ_{23} parameters

These two parameters are highly correlated and are evaluated by experiments measuring the ν_μ disappearance probability. The neutrinos produced by the cosmic ray interaction in the atmosphere are a good source of muon neutrinos. In fact, the first measurement of ν_μ disappearance was made by the Super-Kamiokande experiment in 1998 and confirmed by atmospheric neutrino experiments such as MACRO [27] and Soudan 2 [28].

However, with the advent of accelerator neutrino experiments which can produce a beam of ν_μ in a controlled way, the measurement of $|\Delta m^2_{32}|$ and θ_{23} have been better constrained by them. K2K was the first successful long baseline accelerator experiment that confirmed the ν_μ disappearance result of Super-Kamiokande. T2K and NOνA produce a beam of ν_μ and measure both the probability of $\overset{(-)}{\nu}_\mu$ disappearance and $\overset{(-)}{\nu}_e$ appearance at a far detector. T2K currently has the world leading measurement of $\sin^2\theta_{23}$, which is dependent on the mass hierarchy. The T2K detector is described in detail in Chapter 2. Figure 1.4 shows a comparison of the measurements of $|\Delta m^2_{32}|$ and $\sin^2\theta_{23}$ (assuming the normal hierarchy) from atmospheric and accelerator neutrino experiments.

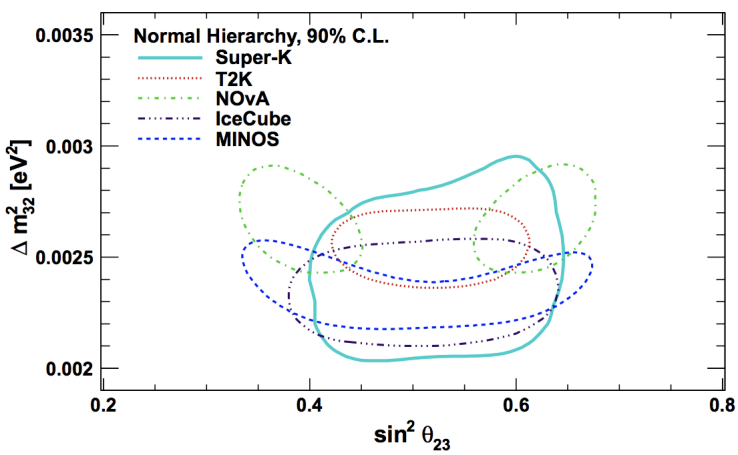

Figure 1.4: The 90% confidence region for $|\Delta m^2_{32}|$ and $\sin^2\theta_{23}$ parameters phase space given by measurement from different experiments. Figure adapted from [3].

Measurement of θ_{13} parameter

The short baseline reactor neutrino experiments measuring the survival probability of $\bar{\nu}_e$ from nuclear reactors are sensitive to $\sin^2 2\theta_{13}$ and Δm^2_{31}. The Daya Bay experiment consists of eight identical liquid scintillator detectors instrumented with PMTs placed in three different locations. The experiment detects the $\bar{\nu}_e$ emitted from six nuclear reactors of Daya Bay and Ling Ao Nuclear Power Plants. Two detector modules each are placed at a distance of $\sim 350 - 550$ m from the two nuclear reactor sources (near detectors) and four modules are placed at a distance of $\sim 1500 - 1900$ m distance from both sources (far detectors).

Although the first results for non-zero θ_{13} value with a statistical significance of 2.5σ was reported by T2K in 2011 [29], Daya Bay's measurement of $\sin^2 2\theta_{13} = 0.092 \pm 0.016(\text{stat.}) \pm 0.005(\text{syst.})$ in 2012 provided a 5.2σ evidence [30]. In fact, the latest Daya Bay results, Eq.

1.17 obtained by combining an exposure of 217 days with six antineutrino detectors and 1013 days with eight detectors provide the most precise measurement of θ_{13} available [31].

$$\begin{aligned} \sin^2 2\theta_{13} &= 0.0841 \pm 0.0027(\text{stat.}) \pm 0.0019(\text{syst.}) \\ |\Delta m^2_{ee}| &= 2.50 \pm 0.06(\text{stat.}) \pm 0.06(\text{syst.}) \times 10^{-3}\text{eV}^2 \end{aligned} \tag{1.17}$$

where $|\Delta m^2_{ee}| \simeq \cos^2\theta_{12}|\Delta m^2_{31}| + \sin^2\theta_{12}|\Delta m^2_{32}|$. The measured value of $|\Delta m^2_{ee}|$ predicts a value of $\Delta m^2_{32} = (2.45 \pm 0.06(\text{stat.}) \pm 0.06(\text{syst.})) \times 10^{-3}\text{eV}^2$ for the normal mass ordering and $\Delta m^2_{32} = -(2.56 \pm 0.06(\text{stat.}) \pm 0.06(\text{syst.})) \times 10^{-3}\text{eV}^2$ for the inverted mass ordering. This is consistent with the measurements from T2K and MINOS experiment.

Measurement of δ_{CP} parameter and mass ordering

A new generation of long baseline neutrino experiments are being built to accurately measure δ_{CP} parameter and the mass hierarchy of neutrinos. However a larger than expected value of θ_{13} parameter measured by the reactor experiments have allowed the present long baseline accelerator neutrino experiments to constrain these parameters. These accelerator neutrino experiments can produce a beam of both ν_μ and $\bar{\nu}_\mu$ by reversing the current of the magnet used in the focusing of charged particles that decay to form the neutrino. This allows them to measure both $P(\nu_\mu \to \nu_e)$ and $P(\bar{\nu}_\mu \to \bar{\nu}_e)$ appearance channels. By comparing measurements in these two channels an estimate of CP asymmetry can be made. The latest results from T2K using the θ_{13} values of reactor measurement disfavors the CP conserving value of $(0, \pi)$ by 2σ [4], as shown in Figure 1.5. This is the strongest constrain on δ_{CP} at this time.

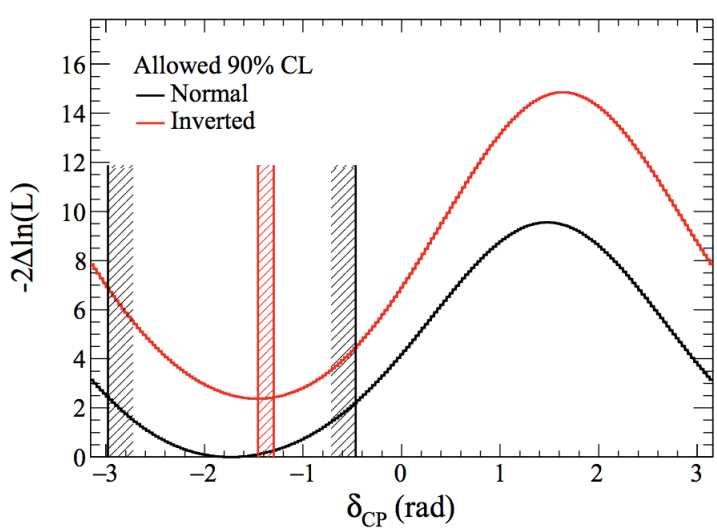

Figure 1.5: 90% confidence interval of the δ_{CP} measurement for the normal (black) and inverted (red) mass hierarchy. These values were obtained by the joint analysis of neutrino and antineutrino oscillations in both appearance and disappearance channels. Constraints for $\sin^2\theta_{13}$ from reactor measurements are implemented. Figure from [4].

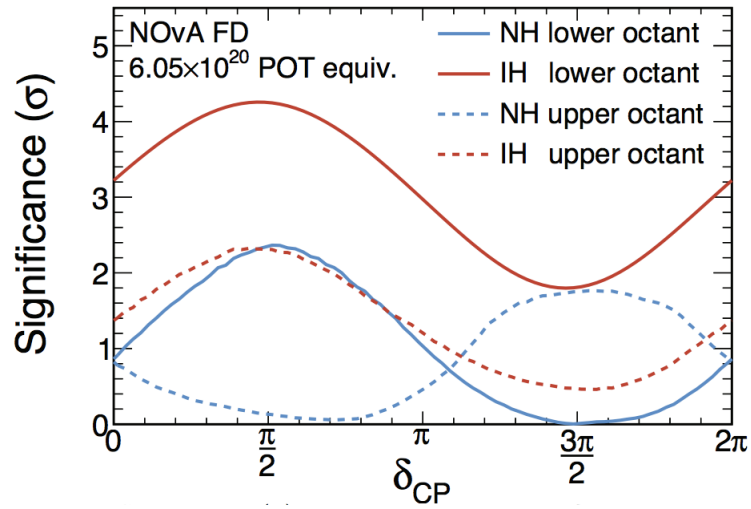

Figure 1.6: Significance at which Noνa disfavors the different values of δ_{CP} for the normal (blue) or inverted (red) hierarchy cases. The solid lines represent θ_{23} in the lower octant and dashed in the upper. Figure from [5].

The NOνA experiment with its higher energy and longer baseline, has a much better sensitivity to the mass hierarchy. A combined analysis of NOνA's ν_e appearance and ν_μ disappearance data with constraints from reactor θ_{13} measurements is shown in Figure 1.6. As NOνA has two statistically degenerate values of $\sin^2\theta_{23}$, seen in Figure 1.4, it has four possible combinations of two mass hierarchy (NH or IH) and octant of θ_{23} ($\theta_{23} > \pi/4$ or $\theta_{23} < \pi/4$). The inverted hierarchy is disfavored at $> 93\%$ for the lower octant [5].

1.3 Neutrino - Nucleus Interactions

The next big goal of the long baseline neutrino experiments is the measurement of the δ_{CP} parameter and the mass hierarchy. To extract oscillation parameters, these experiments measure the near and far detector spectra and solve for:

$$N^{far}(\Theta) = \int \Phi(E_\nu)\sigma(E_\nu)P_{\nu_\alpha\to\nu_\beta}(E_\nu)\epsilon(E_\nu)U(E_\nu,\Theta)dE_\nu \tag{1.18}$$

where $N^{far}(\Theta)$ is number of events at the far detector as function of some observable(s) Θ, $\Phi(E_\nu)$ is the incoming neutrino flux as a function of the incoming neutrino energy measured at the near detector, $\sigma(E_\nu)$ is the cross section as a function of this energy, ϵ captures the efficiency of the detector and $U(E_\nu,\Theta)$ is the detector smearing matrix relating the true E_ν to the observable variable Θ. A Monte Carlo simulation predicts the distribution of detector observable Θ, typically reconstructed neutrino energy for a particular set of values of the oscillation parameters. These oscillation parameters are varied until a best-fit match is found with the data distribution to obtain the best-fit values.

As shown by Eq. 1.18, to precisely measure $P(\nu_\alpha \to \nu_\beta)$, a good knowledge of the incoming neutrino flux, neutrino interaction cross sections, the efficiency and the response functions of the far detector is required. Currently, neutrino cross section parameters contribute

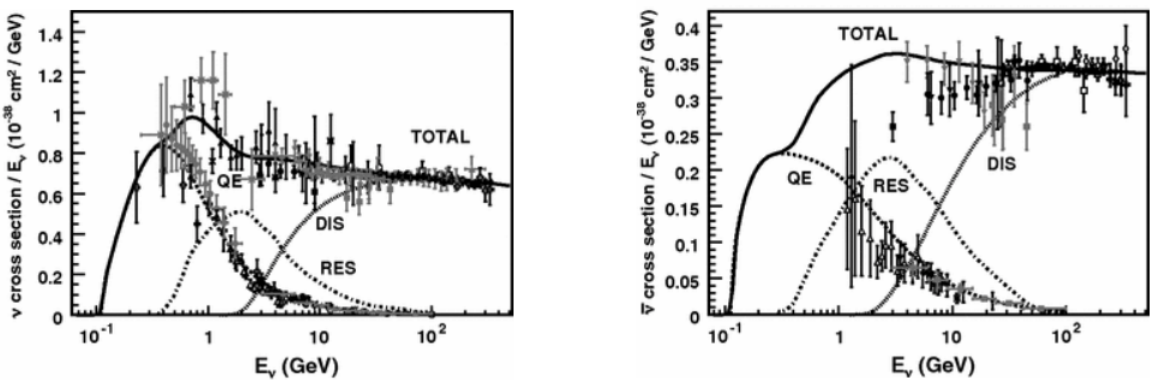

(a) neutrino cross section

(b) antineutrino cross section

Figure 1.7: Total neutrino and antineutrino CC cross section divided by the neutrino energy as a function of energy for different interaction modes as predicted by NUANCE [6]. All data available up to 2012 is overlaid. Figures taken from [7].

$(5-10)\%$ uncertainties in the oscillation parameter measurements at T2K and NOνA. With more data decreasing the statistical uncertainties rapidly, the precision of the parameters may soon be limited by the systematics with the largest contribution from cross section uncertainties. Particularly, the future long baseline neutrino experiments, such as DUNE [32] and Hyper-Kamiokande [33], require a $\sim (2-3)\%$ uncertainty on neutrino cross sections to achieve their predicted sensitivities for δ_{CP} and mass hierarchy.

1.3.1 Interaction Modes

As described in Section 1.1, a neutrino can only interact via weak force. Weak interactions can proceed via exchange of W^+/W^- boson (Charged Current) or Z boson (Neutral Current). The phase space available to interact via different modes is dependent on the energy of the incoming neutrino. The neutrino experiments use neutrino-nucleus interaction simulations or the event generators to simulate large productions of neutrino interactions based on the available theoretical models. The most widely used event generators are NEUT [34], GENIE [35], GiBBU [36, 37], NuWro [38], and Nuance [6]. Figure 1.7 shows the distribution of total neutrino and antineutrino CC cross section divided by neutrino energy as a function of this energy [7].

T2K experiment, described in Chapter 2, has a mean peak energy of 0.6 GeV and employs NEUT event generator to simulate neutrino-nucleus interactions. In view of this, the discussion ahead will focus on interaction modes dominating at this energy and the theoretical models implemented in NEUT.

Elastic and quasi-elastic scattering

The primary mode of interaction of neutrino for energies of $\sim 0.1-1.5$ GeV is to scatter elastically from a nucleon. In the CC interaction, a charged lepton of the same flavor as the incoming neutrino is emitted from the exchange of W^+/W^-. As the outgoing particle is

(a) CC quasi-elastic $\nu - n$ interaction

(b) NC elastic $\nu - p$ interaction

Figure 1.8: Feynman diagram to represent the CC quasi-elastic and NC elastic interaction of neutrino with a nucleon.

different from the incoming particle, this interaction is termed 'quasi-elastic' or CCQE. The NC interaction is referred as elastic scattering.

Even at this basic level, an analytical calculation of the CCQE cross section is complicated by the fact that the nucleon is a composite object. Llewellyn Smith model [39] parameterizes this cross section in terms of variables that can be measured by β-decay and electron scattering experiments.

Resonance production

With the increase in neutrino energy, the neutrinos can excite the target nucleon to a resonance state (N^* or Δ). The resonance state emits mesons, most often a single pion, to return to the ground state. These interactions occur via both CC and NC channels resulting in the following possible modes for a $\nu - n(p)$ interactions:

The three charged current single pion resonant interactions are given by Eq. 1.19 - 1.21 and an example is shown in Figure 1.9.

$$\nu_l + p \rightarrow l^- + p + \pi^+ \tag{1.19}$$

$$\nu_l + n \rightarrow l^- + p + \pi^0 \tag{1.20}$$

$$\nu_l + n \rightarrow l^- + n + \pi^+ \tag{1.21}$$

Equation 1.22 - 1.25 give the four neutral current single pion resonant interaction channels:

$$\nu_l + p \rightarrow \nu_l^- + p + \pi^0 \tag{1.22}$$

$$\nu_l + n \rightarrow \nu_l^- + n + \pi^0 \tag{1.23}$$

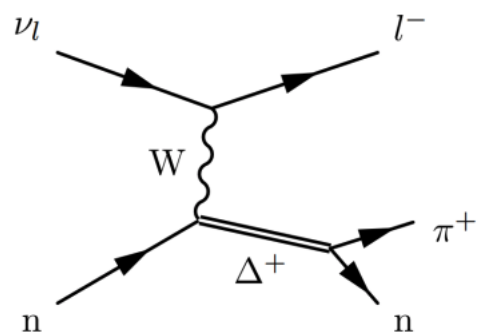

Figure 1.9: Feynman diagram to represent the CC single pion resonant interaction channel.

$$\nu_l + p \rightarrow \nu_l^- + n + \pi^+ \tag{1.24}$$

$$\nu_l + n \rightarrow \nu_l^- + p + \pi^- \tag{1.25}$$

The Rein-Sehgal (RS) model [40] is used by the event generators to simulate resonance interactions. It includes 18 Δ resonances below 2.0 GeV but ignores the masses of charged leptons.

Coherent scattering

The above modes of interactions are for neutrinos interacting on a single nucleon. For a nuclear target, an extra interaction mode becomes available for the neutrinos where they can scatter off the whole nucleus. This makes the nucleus recoil but otherwise leaves it intact. Depending on the energy of the incoming neutrino, coherent scattering can also produce a pion in the final state. A very low four momentum transfer (Q^2) is required for coherent scattering. This requirement constrains the direction of all outgoing particles to be extremely forward going, i.e. small scattering angle with respect to incoming neutrino. These constraints lower the cross section for neutrino to interact via this channel.

The single pion production via coherent scattering channel is given by :

$$\nu_l + A \rightarrow \nu_l + A + \pi^0 \tag{1.26}$$

$$\nu_l + A \rightarrow l^- + A + \pi^+ \tag{1.27}$$

The Rein-Seghal coherent model [41] is used to simulate this interaction by the event generators. Berger and Sehgal [42] introduced a correction due to lepton masses on the single pion production by neutrinos. The resonance and coherent scattering interactions together form the 'single pion production' (SPP) channels for the event generators. Nominal NEUT uses the Rein-Sehgal model [40, 41] with correction from Berger-Sehgal [42] and an additional new form factor [43].

In Oct 2018, M. Kabirnezhad [44], introduced new modifications to the single pion production models. This work includes interference terms between resonant and non-resonant

modes of pion production that were earlier neglected. These changes would be implemented in the next production of NEUT.

Deep inelastic scattering

As the energy of the incoming neutrino increases, it is able to resolve the individual quark constituents of the nucleon and interact with them directly via exchange of $W^{\pm}/Z$ bosons. This is known as deep inelastic scattering (DIS) and it breaks apart the nucleus to produce jets of hadronic shower as the interaction products. This is the dominant mode of interaction for $E_{\nu} > 10$ GeV and has been well measured by the experimental data, as seen in Figure 1.7.

1.3.2 Nuclear Effects

The quasi-elastic and resonance modes of interactions, outlined in Section 1.3.1, describe the interaction of neutrino with a single nucleon. However, this target nucleon is typically present inside a nucleus. Nuclear matter affects the cross section of these processes in many different ways and must be accounted for correctly to predict the neutrino interaction cross sections.

Fermi motion

The nucleons inside the nucleus are in a state of constant motion which contributes an additional boost to the neutrino nucleon interaction in the lab frame. Various models are used to implement the effect of Fermi motion on the neutrino-nucleon cross sections. Relativistic Fermi gas (RFG) is a frequently used model where nucleons within the nucleus are modeled as non-interacting fermions inside a constant nuclear potential. Using simple Fermi-Dirac statistics, the momentum states are filled from ground state up until all nucleons are filled. The highest filled momentum state is known as the Fermi momentum, p_F. RFG is implemented using model by Smith and Moniz [45] in the event generators. An improvement of this model calculates the nuclear potential using the local nuclear density which is a function of the radial distance of nucleon. This is known as local Fermi gas (LFG) model [46]. Both these models still treat nucleons as non-interacting fermions. Model from Benhar and collaborators [47], known as spectral function (SF) model, incorporates the effect of nucleon interaction potentials using the impulse approximation. While it assumes that the neutrino interacts with only one nucleon but it allows for short-range correlations between nucleons to alter the energy and momentum distribution for the nucleon involved in the interaction. Default NEUT generator uses SF model from Benhar to account for the Fermi motion.

Final state interactions

After the interaction, the outgoing particles still have to traverse the length of the nucleus in which they are produced. The dense nuclear matter can scatter, absorb or re-interact with these outgoing particles. It can also emit extra hadrons which were not a product of the initial interaction. These processes are collectively known as final state interactions (FSI), shown in Figure 1.10.

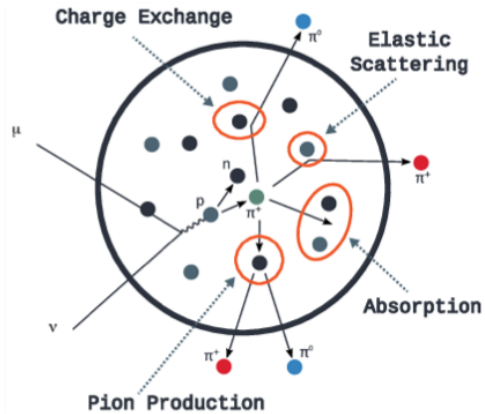

Figure 1.10: Final State Interactions inside a nucleus

Cascade models are used to simulate FSI in event generators. In these models, each hadron at the interaction vertex is propagated through the nuclear matter independently. The probability for a possible set of interactions such as charge exchange, absorption or elastic scattering is calculated at each step based on the nuclear matter density and all by-products are simulated. This process continues until the hadron leaves the nucleus.

Nucleon-nucleon correlations and nuclear screening

A neutrino can interact with a pair of correlated nucleons inside a nucleus. The kinematics of this interaction is quite different from that of an interaction on a single nucleon. Interactions on two correlated nucleons is known as 2p-2h or 'two-particle two-hole' interactions. New models by Nieves et al. [48, 49] and Martini et al. [50] have been proposed to cover the effect of 2p-2h interactions. However, an additional effect to account for the change in electroweak coupling strengths due to nuclear screening has to be added to both Nieves and Martini model to make it compatible with the heavy target neutrino scattering data. Random phase approximation (RPA) [48, 50] is added as a function of Q^2 to alter the neutrino-nucleon cross section due to this screening effect of the nuclear medium. The 2p-2h and RPA models are added as effective models or lookup weight tables to the event generators. The process of characterizing the effects of these parameters is still ongoing and is improving with the publication of new datasets focusing on these measurements [51, 52].

1.3.3 Neutral Current Single π^0 Measurements

As seen in Section 1.3.1, neutrino interactions on nucleon given by Eq. 1.22 and 1.23 produce a single π^0 particle via neutral current channel. Furthermore, coherent neutrino interactions on heavy target nucleus can also produce the π^0 particle via process in Eq. 1.26. These interaction channels form the signal measured in this analysis.

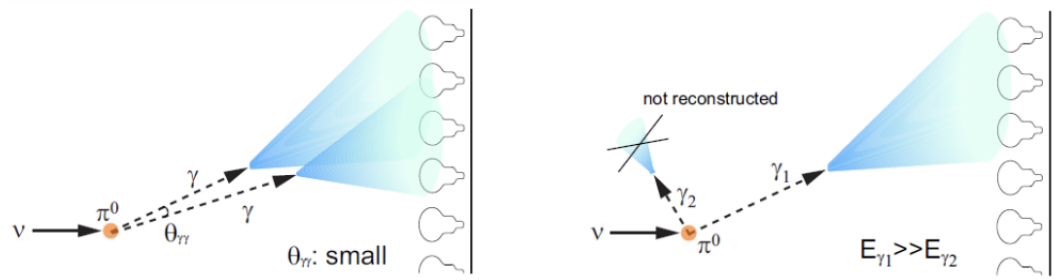

(a) collinear decay

(b) asymmetric decay

Figure 1.12: Schematic figure to represent collinear and asymmetric decay of π^0 particle into two photons [8].

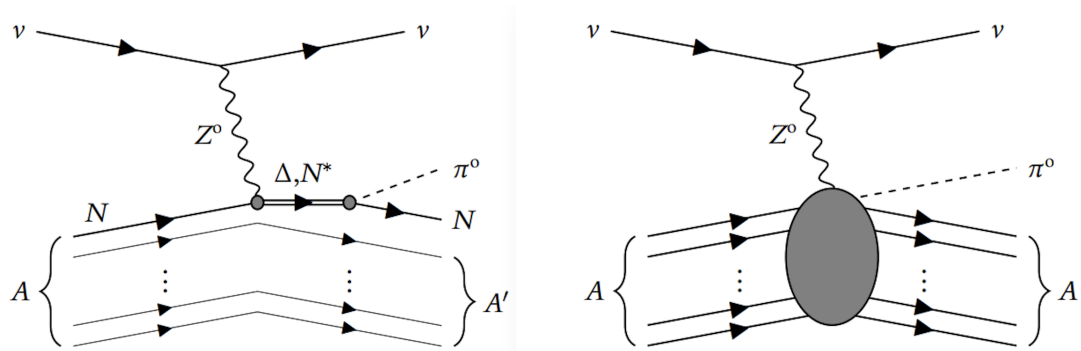

(a) resonant production

(b) coherent production

Figure 1.11: Feynman diagrams to represent the two different modes of π^0 production via neutral current neutrino interaction on a nuclei.

These interactions are important backgrounds for long baseline neutrino experiments measuring $P(\nu_\mu \rightarrow \nu_e)$ appearance probability, such as T2K. The neutral pions produced in these interactions decay into two photons. These photons pair produce to form e^+/e^- pairs which then bremsstrahlung to emit more photons, forming an electromagnetic shower. An asymmetric decay of π^0 particle leading to a faint backward going photon or a highly collinear decay causing an overlap of the two photon showers, mimics the signature of an e^- in the ν_e appearance measurement.

For a water Cherenkov detector such as Super-Kamiokande, detailed in Section 2.3, the Cherenkov radiation from an electromagnetic shower forms a fuzzy ring while a muon has a sharp ring signature. In the case of π^0 decay depicted in Figure 1.11, fuzzy rings from decay photons can be misidentified as coming from e^- in the ν_e appearance. Figure 1.13, shows an example of event display of Super-Kamiokande experiment for a simulated μ^-, e^- and π^0 particle.

The experimental history of measurement of cross section of neutral current single π^0 (NC1π^0) production is quite sparse. A few measurements of the the ratio of NC1π^0 to a CC channel cross section exist from ANL [53, 54] and Gargamelle [55] bubble chamber

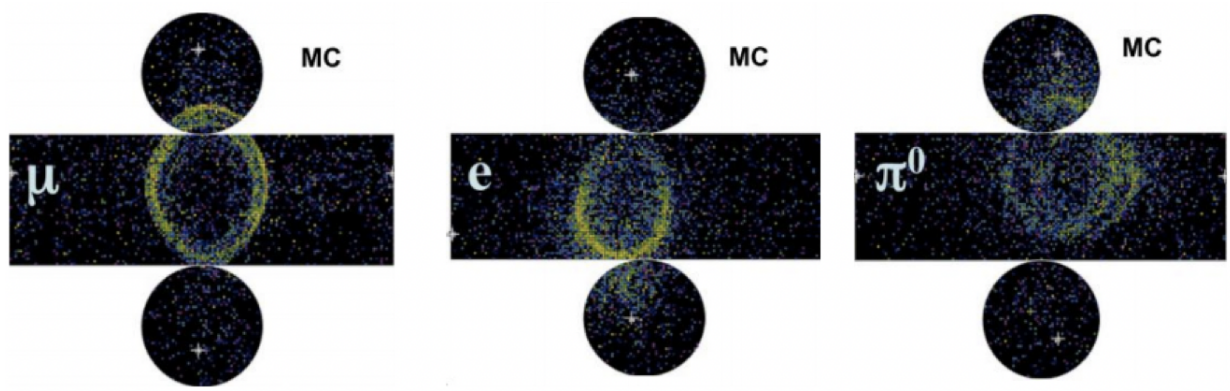

Figure 1.13: A sample event display of Super-Kamiokande experiment showing Cherenkov radiation signature for a simulated event with μ^-, e^- and π^0 particle.

experiments, and BNL [56, 57] and CERN PS [58] spark chamber experiments. These are summarized in Table 1.2 and compared to the prediction from NUANCE [6] generator.

Experiment	Target	NC/CC Ratio	Value
ANL	H_2	$\sigma(\nu_\mu p \to \nu_\mu p \pi^0)$ / $\sigma(\nu_\mu p \to \mu^- p \pi^+)$	0.51 ± 0.25 [53]
ANL	H_2	$\sigma(\nu_\mu p \to \nu_\mu p \pi^0)$ / $\sigma(\nu_\mu p \to \mu^- p \pi^+)$	0.09 ± 0.05 [54]
NUANCE	free nucleon	$\sigma(\nu_\mu p \to \nu_\mu p \pi^0)$ / $\sigma(\nu_\mu p \to \mu^- p \pi^+)$	0.20 [6]
Gargamelle	$C_3H_8CF_3Br$	$\sigma(\nu_\mu N \to \nu_\mu N \pi^0)$ / 2 $\sigma(\nu_\mu n \to \mu^- p \pi^0)$	0.45 ± 0.08 [55]
CERN PS	Al	$\sigma(\nu_\mu N \to \nu_\mu N \pi^0)$ / 2 $\sigma(\nu_\mu n \to \mu^- p \pi^0)$	0.40 ± 0.06 [58]
BNL	Al	$\sigma(\nu_\mu N \to \nu_\mu N \pi^0)$ / 2 $\sigma(\nu_\mu n \to \mu^- p \pi^0)$	0.17 ± 0.04 [56]
BNL	Al	$\sigma(\nu_\mu N \to \nu_\mu N \pi^0)$ / 2 $\sigma(\nu_\mu n \to \mu^- p \pi^0)$	0.248 ± 0.085 [57]
NUANCE	free nucleon	$\sigma(\nu_\mu N \to \nu_\mu N \pi^0)$ / 2 $\sigma(\nu_\mu n \to \mu^- p \pi^0)$	0.41 [6]

Table 1.2: Measurements of ratio of cross section of NC/CC channel using data from bubble chamber(ANL, Gargamelle) and spark chamber (BNL, CERN PS) experiments. $N(n, p)$ runs over interactions on both neutron and proton. The ANL results were reanalyzed with a better understanding of neutron background whereas BNL results were updated after considering multi-π background. The presented data from Gargamelle is also reanalyzed and is corrected for free nucleon. NUANCE provides the Monte Carlo prediction for free nucleon case. Table is adapted from [9].

The first absolute cross section measurements of NC1π^0 was obtained by the re-ananlysis of Gargamelle's propane-freone bubble chamber data by Hawker in 2002 [55], shown in Figure 1.14.

In 2005, K2K [59] followed by SciBooNE, in 2010 [60, 61] published the results of ratio of cross section of NC1π^0 to CC inclusive channels. K2K is the only experiment to make this measurement on water before T2K. However, it was made for a wide beam of incoming neutrino energy ($E_\nu \sim 1 - 1.5$) GeV. Their results are summarized in Table 1.3.

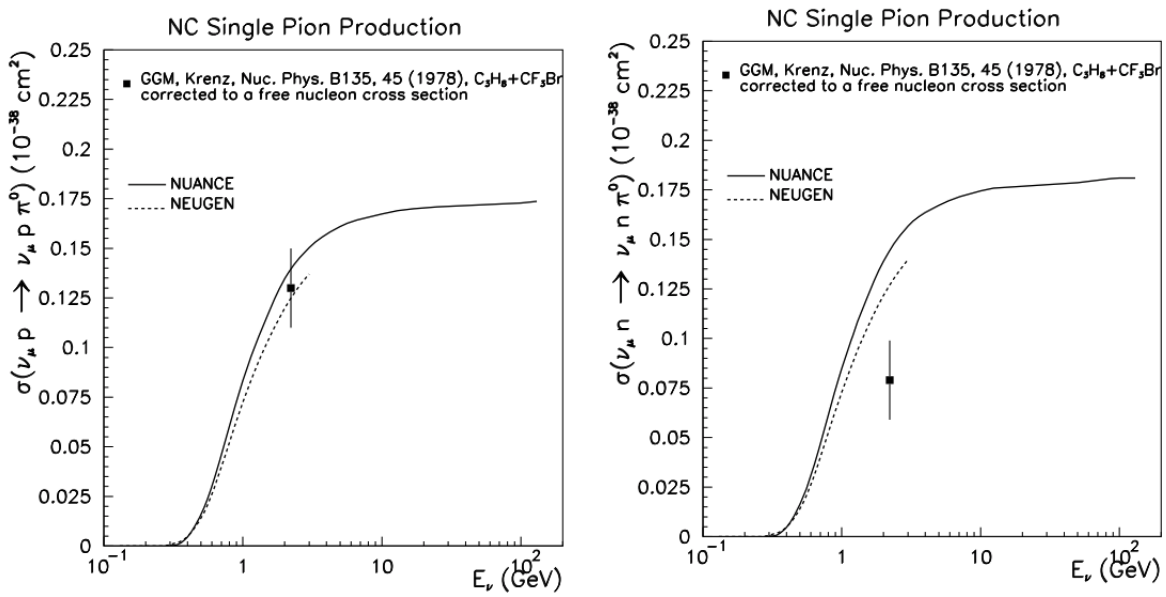

(a)
$\sigma(\nu_\mu p \to \nu_\mu p \pi^0)$

(b)
$\sigma(\nu_\mu n \to \nu_\mu n \pi^0)$

Figure 1.14: NC1π^0 cross section obtained from the re-ananlysis of Gargamelle data on propane+freone, corrected to a free nucleon. Figure from [9].

Experiment	Target	$< E_\nu >$ (GeV)	NC/CC Ratio	Value
K2K	H_2O	1.3	σ(NC1π^0) / σ(CC incl.)	0.064 ± 0.001 ± 0.007 [59]
SciBooNE	C_8H_8	1.1	σ(NC1π^0) / σ(CC incl.)	0.077 ± 0.005 ± 0.005 [60]

Table 1.3: Measurement of NC/CC ratio by K2K (2005) and SciBooNE (2010) experiments. NEUT predicts a ratio of 0.065 for K2K and 0.068 for SciBooNE energies. K2K has the only measurement on water besides T2K.

MiniBooNE published the absolute cross section of NC1π^0 channel for both ν_μ and $\bar{\nu}_\mu$ interactions on mineral oil in 2010 [16]. These results are summarized in Table 1.4. ArgoNEUT published the ratio of NC1π^0 to CC Inclusive and absolute measurements of cross section from both ν_μ and $\bar{\nu}_\mu$ interactions on Argon in 2017 [62].

Mode	$< E_\nu >$ (in GeV)	Total Cross Section ($\times 10^{-40}$cm^2/nucleon)
ν	0.81	4.76 ± 0.05 (stat.) ± 0.76 (syst.)
$\bar{\nu}$	0.66	1.48 ± 0.05 (stat.) ± 0.23 (syst.)

Table 1.4: Absolute cross sections for the NC1π^0 interaction on mineral oil by MiniBooNE experiment [16].

T2K's previous measurement of NC1π^0 rate was published in 2018 [10]. This measure-

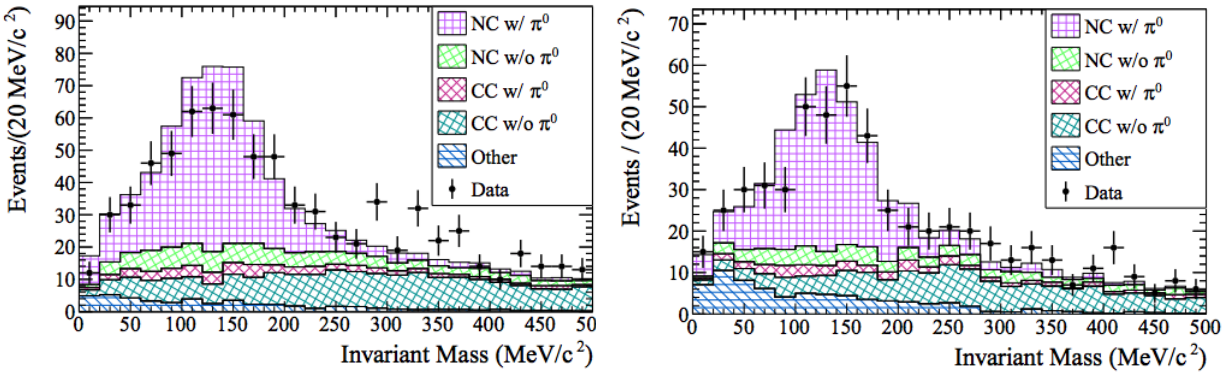

(a)
PØD water-in configuration

(b)
PØD water-out configuration

Figure 1.15: Comparison of data and nominal T2K Monte Carlo for the distribution of NC1π^0 invariant mass [10].

ment was made using the Pi0 Detector (PØD), described in Section 2.4 which operates in two different configuration - PØD water-in and PØD water-out. This enables the extraction of interactions that occur on water.

The previous analysis measured the data to Monte Carlo ratio for the number of NC1π^0 interaction events on water. It used 2.64×10^{20} protons-on-target (POT) for PØD water-in and 3.49×10^{20} POT for PØD water-out configurations. The events were selected with an efficiency of $6.01 \pm 0.01\%(4.79 \pm 0.02\%)$ and a purity of $48.7 \pm 0.17\%(46.1 \pm 0.3\%)$ for the water-in (water-out) sample. The results obtained in this analysis for different PØD configurations are summarized in Table 1.5.

PØD config	Expected	Observed	Ratio (Obs/Exp)
water-in	433	342 ± 33(stat.) ± 88(syst.)	$0.79 \pm 0.08 \pm 0.20$
water-out	290	246 ± 26(stat.) ± 61(syst.)	$0.85 \pm 0.09 \pm 0.21$
on-water	157	106 ± 41(stat.) ± 69(syst.)	$0.68 \pm 0.26 \pm 0.44$

Table 1.5: NC1π^0 events in PØD in the previous T2K analysis [10].

A 12% uncertainty on T2K beam flux for this measurement is added, in addition to the uncertainties listed above. The results of this analysis are systematically limited. The largest systematics for this analysis came from the selection cuts and background shape estimation. Varying the value of the cut leads to large differences in data and Monte Carlo events passing the cut, which contributes to the systematics.

The remainder of this thesis will describe in detail the T2K experiment and the current iteration of NC1π^0 analysis. Apart from additional data from recent T2K runs, the reconstruction and selection cuts were updated. A new fitter using Bayesian inference from Markov Chain Monte Carlo (MCMC) sampling method was developed to handle the data - Monte Carlo fitting and the systematics more comprehensively. These changes will be

highlighted in the relevant sections of this thesis. Chapter 2 will describe the T2K experiment with a focus on the Pi0 Detector (PØD) used for this analysis. Event selection for the NC1π^0 signal sample and the associated efficiencies, and the background control sample are detailed in Chapter 3. The likelihood function formulation and the algorithm used for MCMC sampling is described in Chapter 4. Chapter 5 explains the parameters of the fit and the calculation of related systematic uncertainties. Chapter 6 reports the results and errors obtained in this analysis. We conclude by summarizing the analysis and laying out its future prospects in Chapter 7.

Chapter 2

The T2K Experiment

"Data!data!data!" he cried impatiently. "I can't make bricks without clay." - Sir Arthur Conan Doyle, The Adventures of Sherlock Holmes

T2K (Tokai-to-Kamioka) is a long baseline neutrino experiment built with the purpose to detect the ν_e appearance in a ν_μ beam [63]. A beam of muon neutrinos is produced at Japan Proton Accelerator Research Complex (J-PARC) located in Tokai, Japan. An ensemble of detectors at 280 m downstream of the target forms the near detector. Super-Kamiokande (SK), a water Cherenkov detector, located 295 km away from the target in Kamioka, Japan serves as the far detector. The main goal of the experiment was to measure θ_{13}, along with the precision measurement of $\sin^2 2\theta_{23}$ and Δm^2_{23}. A large value of θ_{13} has enabled T2K to make measurements towards constraining the δ_{CP} parameter. Aside from oscillation physics, it has a rich program to measure neutrino-nucleus cross section on different targets at the near detector. It also conducts searches for sterile neutrino and makes measurement of neutrino time of flight.

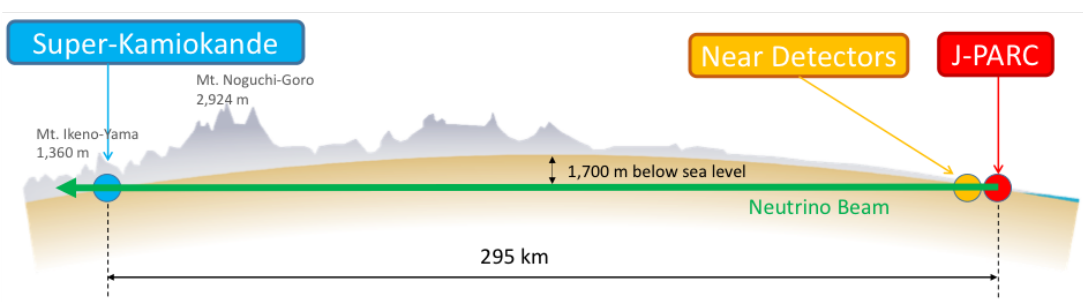

Figure 2.1: A schematic view of the T2K experiment.

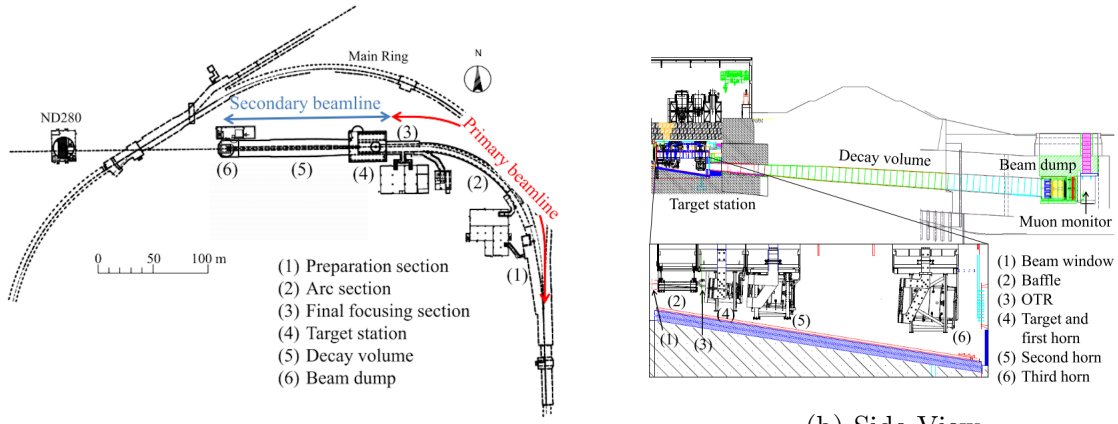

(a) Top View

(b) Side View

Figure 2.2: An overview of the primary and secondary beamline of T2K.

A schematic of the T2K experiment is shown in Figure 2.1. Each component of the experiment is described in detail in the following sections.

2.1 Neutrino Beamline

A linear accelerator (LINAC) accelerates a H^- beam up to 400 MeV and then supplied to the rapid-cycling synchrotron (RCS). The beam is converted to H^+ at the RCS injection by charge stripping foils. RCS accelerates the proton beam to 3 GeV and delivers a fraction of them to the main ring (MR) synchrotron. Proton beam is accelerated to 30 GeV in the MR and then extracted into the primary neutrino beamline. Each spill is $5\mu s$ and consists of 8 bunches. The stability of the beam is guaranteed by a series of beam monitors that measure the beam intensity, position, profile and beam loss.

In the secondary beamline, the protons strike the graphite target (91.4 cm long, 2.6 cm in diameter with a density of 1.8 g/cm^3)to mostly produce $\pi^\pm, K^\pm$. The mesons produced are charge selected and focussed into a decay volume by a series of three 2.1 T magnetic horns. For a positive horn current, $I = 250$ kA, (tunable to 320 kA), mostly π^+ and K^+ are selected which decay to ν_μ. This beam configuration is known as forward horn current or FHC. If the current in the magnetic horn is reversed (reverse horn current or RHC), the mesons of the opposite charge would be selected, thereby allowing the production of an antineutrino beam.

The mesons are sent through a 96 m long decay volume where they decay into neutrinos.

$$\begin{aligned} &\pi^+ \to \mu^+ + \nu_\mu; K^+ \to \mu^+ + \nu_\mu (\text{FHC}) \\ &\pi^- \to \mu^- + \bar{\nu}_\mu; K^- \to \mu^- + \bar{\nu}_\mu (\text{RHC}) \end{aligned} \tag{2.1}$$

A wrong-sign contamination of mesons, decay of μ^+ into ν_e or decay of kaon via another mode that produces ν_e contaminates the ν_μ beam with small components of $\bar{\nu}_\mu$ and ν_e. A beam dump is placed at the end of decay volume to stop all hadrons and muons < 5 GeV.

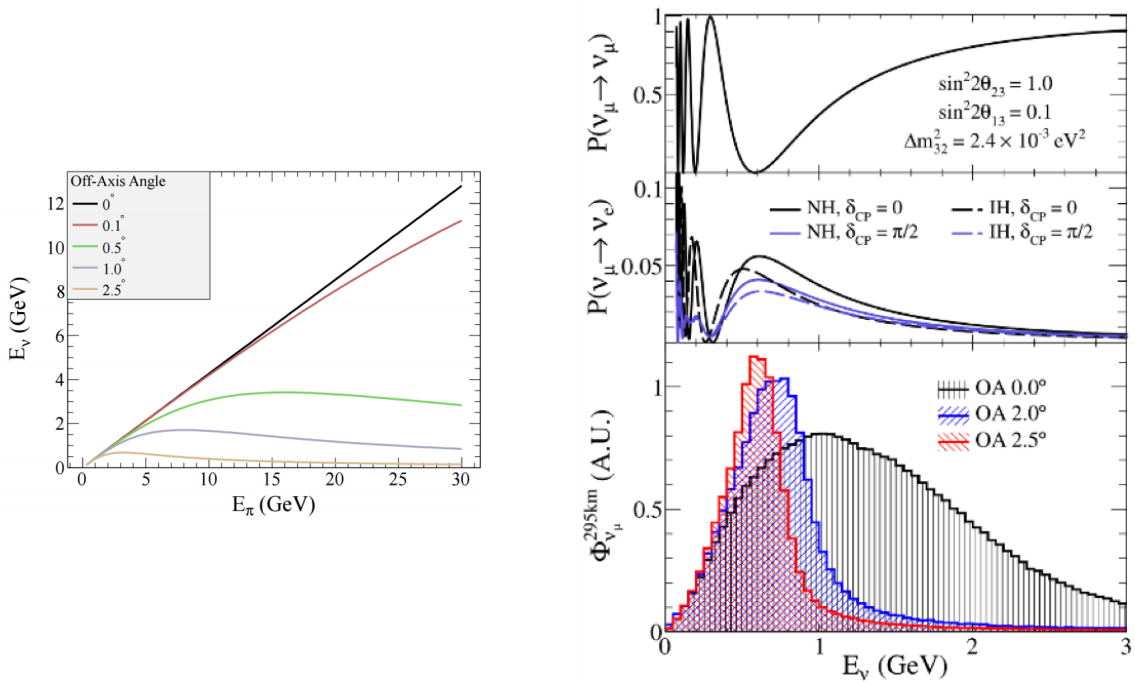

Figure 2.3: Feynman diagram to represent the CC quasi-elastic and NC elastic interaction of neutrino with a nucleon.

A muon monitor (MUMON) is placed just downstream of the beam dump to measure the direction of muons above 5 GeV and monitor the beam profile.

As the ν_μ beam is produced from a two body decay of pions, the neutrino energy is dependent on the pion energy, as given by Eq.2.2.

$$E_\nu = \frac{m_\pi^2 - m_\mu^2}{2(E_\pi - p_\pi \cos\theta)} \tag{2.2}$$

where E_ν is the energy of the outgoing ν_μ, E_π is the pion energy, p_π the pion momentum, m_π the pion mass, m_μ is the muon mass and θ is the angle between pion and the outgoing neutrino.

While it is impossible to get a mono-energetic beam of neutrinos, we can reduce the dependence on E_π by varying θ as seen in the left panel of Figure 2.3. T2K utilizes this off-axis effect by designing the beam centre 2.5° away from ND280 and SK detectors. This gives a narrow beam flux, shown in the right panel of Figure 2.3, peaked at ~ 0.6 GeV which maximizes the oscillation probability for a baseline of 295 km. T2K was the first experiment to use the off-axis angle to narrow the beam energy spread.

Lastly, it is important to carefully simulate the steps involved in the beam production to correctly predict the T2K flux. FLUKA 2008 [64,65] is used to model the proton interactions with the target. The propagation of the mesons through the secondary beamline is simulated using GEANT3 [66]. The interactions of exiting particles with the surrounding material is modeled using GCALOR [67]. Additionally, data from NA61/SHINE experiment [68, 69] which measures the hadron production of a 30 GeV proton beam on a replica of T2K target, is used to tune the hadron interaction models to provide a more accurate flux prediction.

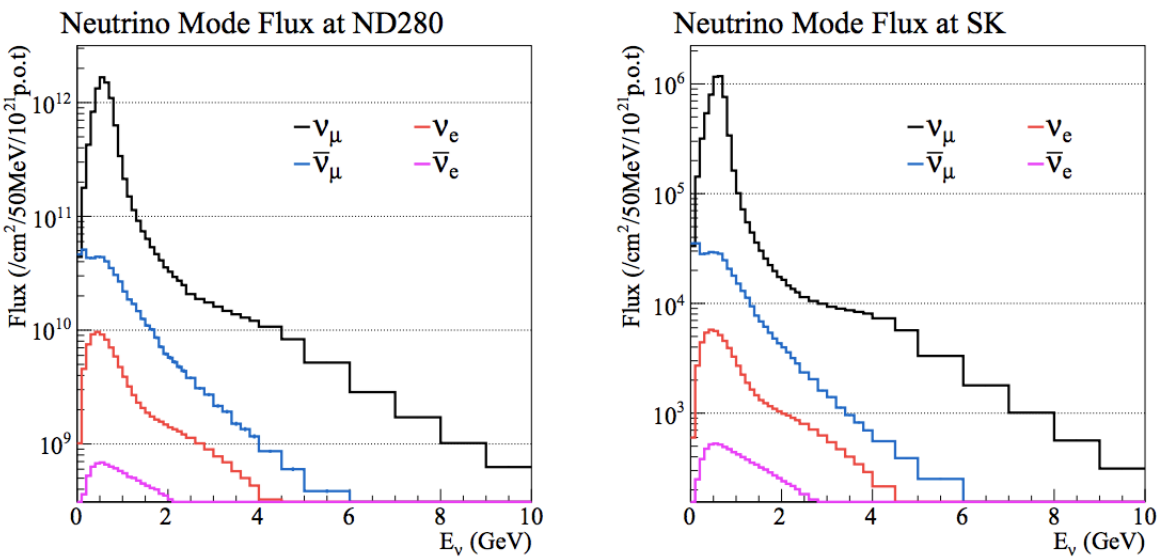

Figure 2.4: The predicted off-axis neutrino (unoscillated) beam flux at ND280 and SK.

Figure 2.4 shows the ν_μ beam flux at ND280 and SK detector.

2.2 The Near Detector

The near detector complex is located 280 m downstream of the graphite target. An on-axis Interactive Neutrino Grid (INGRID) detector monitors the beam profile and intensity whereas the off-axis detector measures various neutrino interactions thereby constraining the neutrino flux and interaction models. ND280 is enclosed inside a 0.2 T magnet which was refurbished from the UA1 experiment at CERN. The bending of charged particles in the presence of the magnetic field aids in the determination of their kinematics. All ND280 detectors that detect particles by capturing scintillation light use wavelength shifting fibers (WLS) threaded inside the scintillator bar for light collection. The signal is read out by Hamamatsu Multi-Pixel Photon Counter (MPPC) attached to the end of WLS. The stability of MPPCs inside a magnetic field and their compact size make them a suitable choice for all ND280 detectors.

2.2.1 INGRID : On-axis detector

The INGRID is composed of 16 identical INGRID modules made up of nine iron plates interlaid with 11 scintillator planes, and one proton module formed entirely from the scintillator plane. 14 INGRID modules are arranged in a cross with the proton module placed in the center to detect muons and protons. The two supplementary INGRID modules are placed on the outside the main cross to measure the axial symmetry of the beam. It spans an area of 10 m $\times$ 10 m. INGRID monitors the center of the beam with a precision of $\sim$ 0.4 mrad.

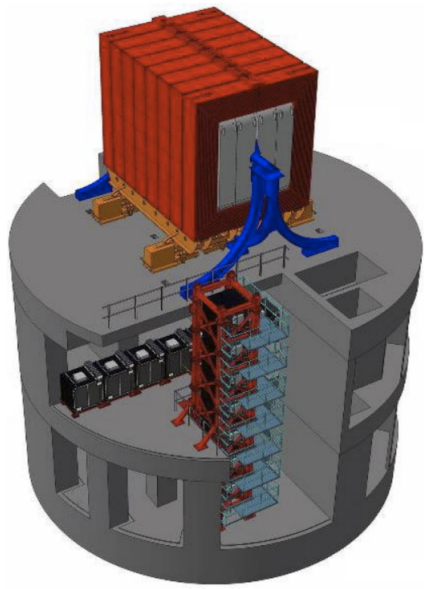

Figure 2.5: The near detector complex of T2K. The bottom floor holds the on-axis detector (INGRID) while on top is the ND280 off-axis detector enclosed inside the magnet.

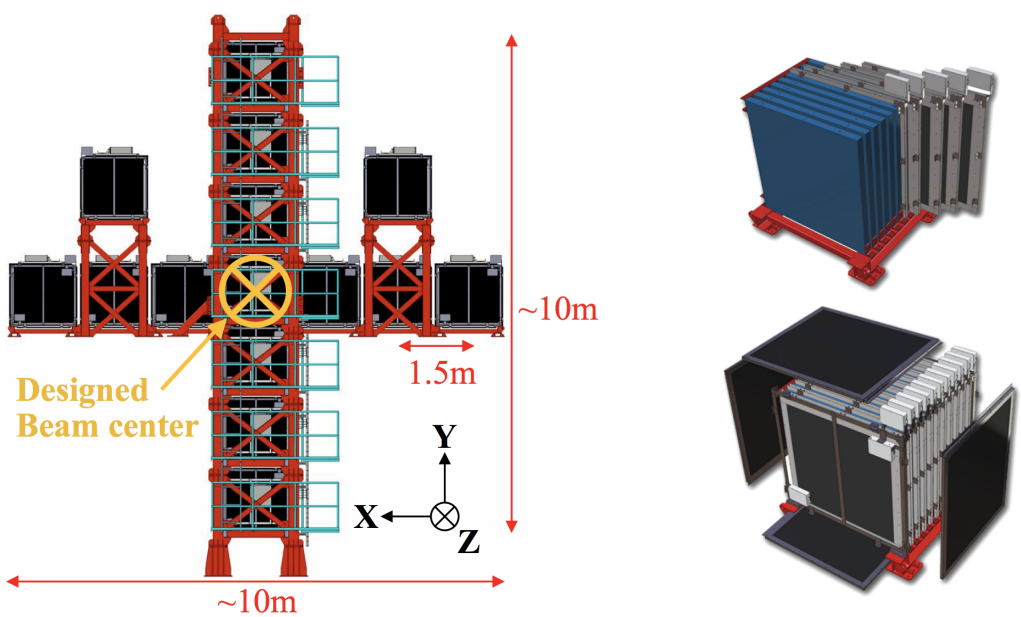

Figure 2.6: INGRID.

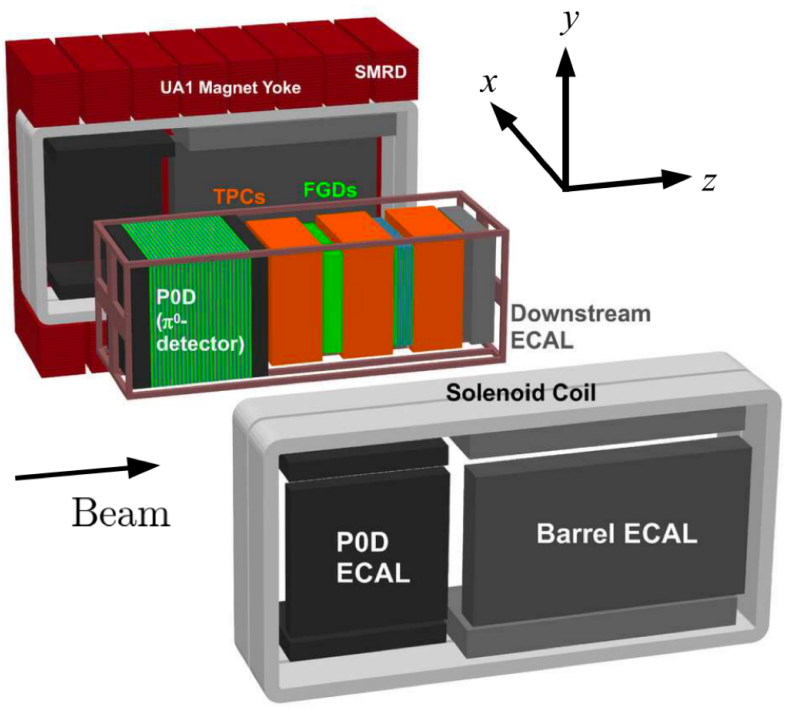

Figure 2.7: The ND280 off-axis detectors at T2K.

2.2.2 ND280 : Off-axis detector

The ensemble of detectors placed at 2.5^o off-axis to the beam at the near detector complex are collectively known as ND280. The Pi-zero Detector (PØD) is the most upstream detector followed by a tracker comprising of two Fine Grained Detectors (FGD) and three Time Projection Chamber (TPC) modules. Both PØD and tracker are surrounded by several Electromagnetic Calorimeter (ECal) modules. The UA1 magnet that encloses the whole detector is interlaid with Side Muon Range Detector (SMRD) panels to tag high angled exiting muons and veto cosmic ray muon or event from interactions on the surrounding materials.

As this analysis focuses on the PØD, it'll be described in a separate Section 2.4. Downstream of the PØD is the tracker region where the two FGD's are interlaid with three TPC modules. The FGDs provides the required target mass for neutrino interactions and provide tracking for charged particles close to the vertex. For an accurate measure of individual charged particle tracks, the FGDs have a fine granularity to provide good resolutions. Both FGD's are built from 1864.3 mm long polystyrene scintillator bars with a cross section of 9.61 mm $\times$ 9.61 mm to achieve the required granularity. The bars are arranged in a horizontal and vertical axis perpendicular to the beam direction to form a 'XY module'. Each direction of the 'XY module' is made up of 192 individual scintillator bars. The first FGD (FGD1) consists of 15 XY modules while FGD2 has 7 XY modules alternating with 6 2.5 cm thick water layers. They both have an outer dimension of 2300 m (w) $\times$ 2400 m (h) $\times$

365 mm (l in the beam direction) and a mass of 1.1 tons of target material. FGD's provide particle identification for short track particles such as protons and pions that do not leave the FGD. A much better resolution is provided by TPCs for particles that exit FGD. The three TPCs are identical to each other and are placed alternating with FGDs to precisely track particles that exit the FGD after a neutrino interaction. The TPCs are filled with a gas mixture of Ar:CF4:iC4H10 in the ratio of 95:3:2 and contain a central cathode creating a uniform electric field of 280 V/cm in the drift region, aligned with the outer magnetic field provided by the UA1 magnet. The charged particles entering the TPC ionize the gas creating electrons that drift towards the readout planes. Hence, the TPCs have the capacity to track particles in 3D and are useful for precise measurements of number and kinematics of the charged particles. An event display for a event which interacts in the first FGD and travels through the tracker is shown in Figure 2.8.

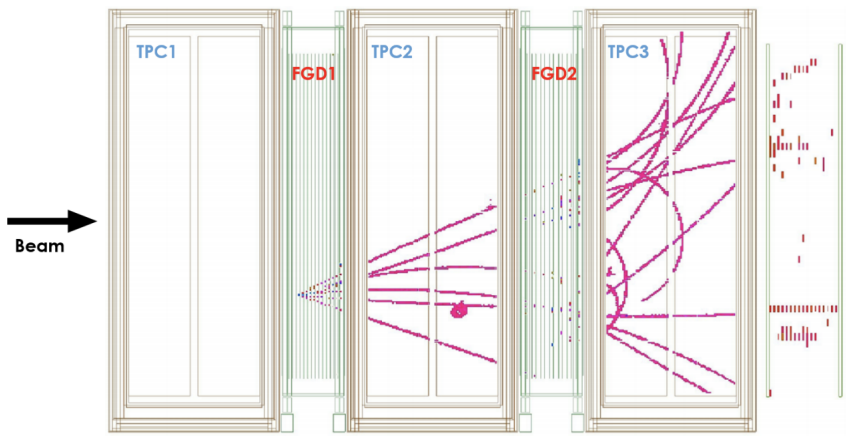

Figure 2.8: An event display of a (likely)DIS event in the tracker part of ND280 off-axis detectors consisting of three TPCs and two FGDs.

.

The PØD, FGD and TPCs are surrounded by 13 independent ECal modules from all sides. Six barrel ECals surround the tracker region and six PØDECals are placed to cover PØD from all four directions. One last ECal module (DsECal) is placed at the most downstream end of the ND280 detector, as shown in Figure 2.7. All ECal modules are made of layers of plastic scintillator alternating with lead absorber sheets. They are useful for measuring the direction and charge of particles that exit the detector they surround. The layers of lead sheet which have a short radiation length, convert photons into e^+/e^- showers so that they can be detected before escaping the detector. Barrel ECal modules have 1.75 mm lead sheets and composed of 31 layers which provides a 9.7 radiation length. The DsECal has the same thickness of lead but provides a total radiation length of 10.6 from 34 layers. Only six layers are used for PØDECal but the thickness of lead sheet is increased to 4 mm to obtain a total of 3.6 radiation lengths.

2.3 Super-Kamiokande : The Far Detector

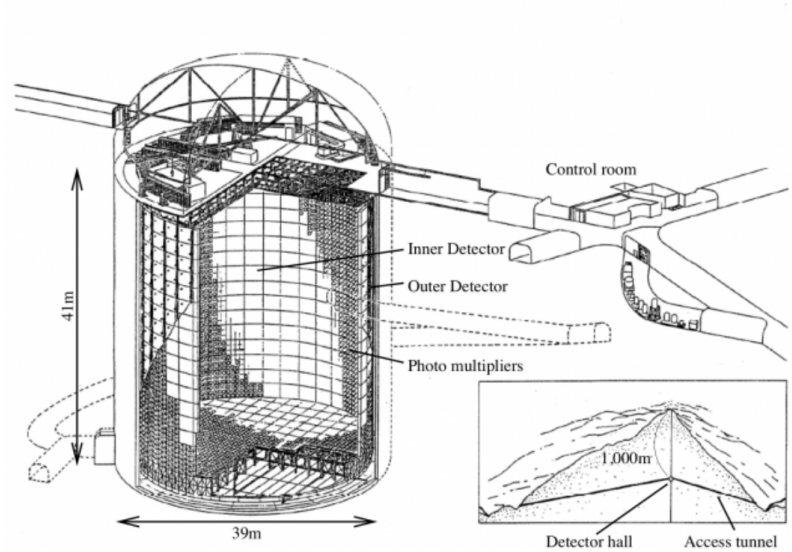

Figure 2.9: The Super-Kamiokande detector.

Super-Kamiokande is located 295 km away from the neutrino target on the west coast of Japan. It is placed 1 km underground, in Mozumi mine to shield against the cosmic rays. It consists of cylindrical tank with a height of 41.4 m tall and diameter of 39.3 m which is filled with 50 Kton of ultra-pure water. It is a water Cherenkov detector which is lined with photomultiplier tubes (PMTs) to capture the Cherenkov radiation emitted by the charged particles when they travel faster than the speed of light in a dielectric medium. SK is divided into two concentric parts - the Outer Detector (OD) and the Inner Detector (ID). The ID is a 33.8 m wide and 36.2 m high cylinder whose surface is covered with 11,146 PMTs of 50 cm diameter. It is surrounded by $\sim$ 2.5 m thick OD which is covered with 1,885 outward facing 20 cm PMTs. A 55 cm thick stainless steel structure separates the ID from the OD and functions as the structure holding the PMTs and the electronics. The OD serves as the veto to reject cosmic events or any interactions on rock in the surrounding environment.

2.4 PØD : The Pi0 Detector

The PØD is the primary detector used to make measurements in this analysis. It is the most upstream of the ND280 detectors, shown in Figure 2.7. This section will highlight the construction, data acquisition and provide a brief description of the PØD reconstruction. The complete details of PØD construction and electronics can be found in [11].

The PØD is subdivided into four parts, known as SuperPØDules. These SuperPØDules are Upstream ECal (USECal), Upstream Water Target (USWT), Central Water Target (CWT) and a Central ECal (CECal), Figure 2.11. As downstream typically refers to the downstream end of the whole ND280 detector, PØD uses upstream and central to distinguish between its two halves. Triangular polystyrene scintillator bars with a height of 17 $\pm$ 0.5 mm and

33 ± 0.5 mm width are placed next to each other with alternating side up to form a layer of scintillator bars, seen in inset of Figure 2.11. There are 134 bars in the horizontal X layer and 126 vertical bars in the Y layer. The two layers are joined using epoxy to form a single module, known as PØDule. Each scintillator bar has a 2.6 mm diameter hole to thread the wavelength shifting (WLS) fiber. As shown in Figure 2.10, the WLS is coupled to the Hamamatsu MPPCs at the other end leading to Trip-t front end electronic readout boards [70]. These boards are built from Trip-T chip originally designed for Tevatron D0 Experiment. A total of 10,400 channels for each scintillator bar are read-out in PØD.

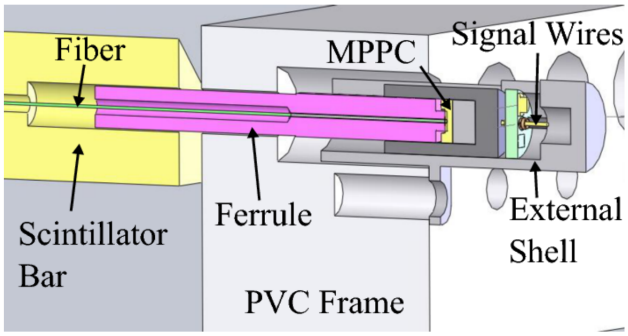

Figure 2.10: A schematic depicting connection of wavelength shifting (WLS) fiber connection to the multi-pixel photon counter (MPPC). Figure from [11].

The USECal and CECal are identical modules placed at either end of the PØD in the beam direction. They consist of seven PØDules alternating with seven 4.5 mm thick lead sheets. The water SuperPØDules are built by placing a PØDule alternating with a water layer and a 1.28 mm thick brass sheet. USWT has 13 such modules while CWT has only 12 modules. The water is contained in bags which are made from high-density polyethylene (HDPE) bladders and are designed to provide an average thickness of 3 cm of water layer in the beam direction. A vertical HDPE strut is built to hold the water bags in place. Each strut holds two water bags side-by-side. Thus, there are a total of 50 water bags in 25 water target layers from both USWT (13 layers) and CWT (12 layers). The PØDules apart from providing the active tracking also serve as additional structural support to the detector. The HDPE strut has holes to insert sensors to measure water level and PVC pipes to fill and drain the water bags. Thus, PØD is constructed such that the water bags can be drained and filled with water periodically. Therefore, measurements can be made with both water-in and water-out configurations of PØD and the neutrino interactions only on water can be extracted. The dimensions of the PØD are 2103 mm (w) x 2239 mm(h) x 2400 mm(l in the beam direction) and the mass of the detector with and without water is 15,800 kg and 12,900 kg respectively.

The coordinate axes used to specify the detector configuration is shown in Figure 2.7. The radiation length of a photon is approximately 25 cm in the water target SuperPØDules when filled with water and 38 cm when the water is drained. In the x and y axis, the fiducial distance is optimized to be 25 cm from the edges for a electron or photon based analysis. However, as the edges can be ill defined in places where the scintillator planes do not align perfectly, this distance is calculated from the center of the PØD. In the beam direction, z

Coordinate	Center (mm)	Minimum (mm)	Maximum (mm)	Total Fiducial Length (mm)
X	-36	-836	764	1600
Y	-1	-871	869	1740
Z	-2116	-2969	-1264	1705

Table 2.1: PØD Fiducial Volume in Global ND280 Coordinates

axis, fiducial distance is chosen as the distance from the center of first upstream water target PØDule to the center of the last central water target PØDule. Further details can be found in [71]. Table 2.1 lists the fiducial distance in all three coordinates.

2.4.1 P0D Reconstruction

GEANT4 [66] is used to simulate the geometry of all near detectors. The neutrino flux estimated through the beam Monte Carlo, mentioned in Section 2.1, is propagated through the entire geometry of the detector. Interaction events are generated by NEUT Monte Carlo [34], based on neutrino cross section models, described in Section 1.3, specific to the target nuclei in each sub-detector. GEANT4 also simulates the energy deposit of particles as they pass through the active region, such as the scintillator bars, WLS fibres, MPPCs and electronics or the TPC electron drift for each of the specified detector geometry. A simulation of electronic noise is also added to the Monte Carlo prediction.

To process both Monte Carlo and data files, a series of calibration constants and alignment parameters are applied individually for each of the sub-detectors. These calibrated digitized hits are then passed to the reconstruction software. Each sub-detector maintains a dedicated reconstruction package to meet its individual need. A global reconstruction for the whole off-axis ND280 detector is built using Rec-Pack toolkit [72].

An analysis can use a combination of the global and local detector reconstruction for its purpose. Tracker based analysis in the near detector depend heavily on the global reconstruction for event selection. However, events with photons or electrons that produce electromagnetic showers in PØD are not well reconstructed by global reconstruction. Hence, this analysis only uses the output from local PØD reconstruction. A significant fraction of thesis work was utilized in making local PØD reconstruction compatible with an analysis tools software package called 'High Level Analysis at Near Detector' or (HighLAND). The process and the utility of this work is briefly described in the Appendix A at the end of the thesis.

An outline of the PØD event reconstruction is provided here. Further details are available in [73]. The calibrated hits are used as inputs for reconstruction. These hits are separated by electronic cycles and a cleaning algorithm is employed to remove noise hits. The PØD reconstruction is performed in two stages - Track reconstruction followed by a Shower reconstruction, as shown in Figure 2.12. All the hits are first passed through a track reconstruction algorithm. Since PØD records hits in two separate 2D layers (X-Z and Y-Z) of scintillator bars, reconstruction is first performed in two dimensional space and then matched to form a 3D object. A Kalman fitter is used to identify relatively longer tracks into kLightTrack

Figure 2.11: The Pi0 Detector (P0D)

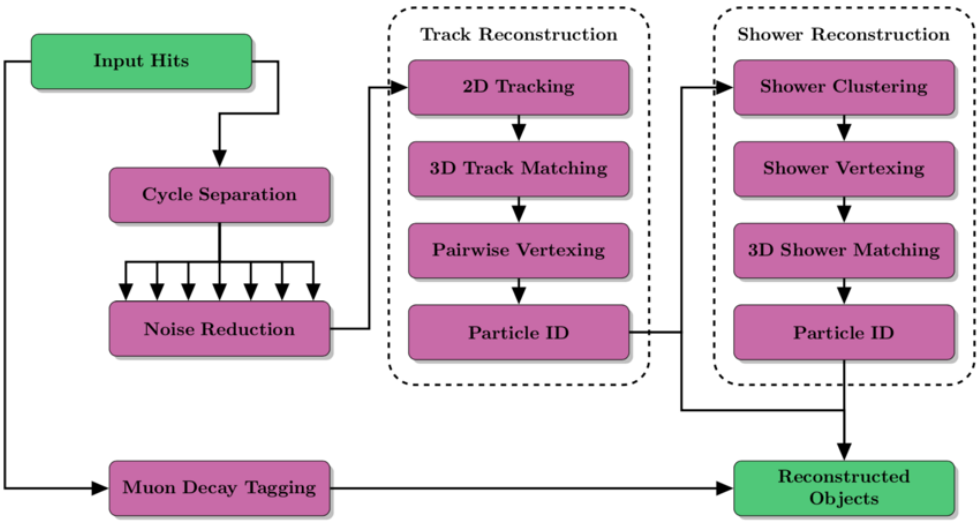

Figure 2.12: P0D Reconstruction Algorithm

(typically muons), kHeavyTrack (typically protons) and kEM (showering particles). A parametric fit is performed on all short tracks and they are tagged as kOthers. Particles tagged as kLightTrack and kHeavyTrack by the reconstruction are sent directly to the output.

All the hits belonging to kEM and kOthers category then go through a shower reconstruction algorithm. A shower particle is reconstructed from 3 to 5 clusters. A cluster is a group of hits that are closer to each other than another group of hits. The clustering is done in two dimensional space and an interaction vertex is located. Finally, two dimensional showers are matched to form a 3D shower particle.

To identify good quality showers from mis-reconstructed particles, a particle identification(PID) algorithm assigns weights to all reconstructed shower particle based on the quantities described below:

1. First charge asymmetry = $\frac{(Q_{last}-Q_{first})}{Q_{last}}$
2. Middle charge asymmetry = $\frac{(Q_{last}-Q_{middle})}{Q_{last}}$

where, Q_{first} is the charge deposited in the first cluster, Q_{last} is the charge deposited in the last cluster, and Q_{middle} is the charge deposited in the middle cluster. For a 4 cluster particle, the second cluster is defined as the middle cluster.

These measurements are done separately for the showers with 3, 4 and 5 clusters. Monte Carlo truth was used to compile a table of the probabilities of the charge asymmetry values for true EM showers and mis-reconstructed EM showers. Adding the (log of) probability values for both of the above asymmetry gives us the weight for EM PID (kEM) tag and non-EM PID (kShower) tag.

Additionally, the PØD reconstruction tags events which exit the detector. An event is considered to be exiting the sides of the PØD, if it has any hits in the two outermost scintillator bars in the x and y axis of the detector. Any hit below a threshold of 7 PEU (photo-electric unit) charge deposit is considered noise as it could be caused by a misfire or fluctuation in MPPC, and hence ignored. Moreover, if the centroid position of the first and last cluster of the reconstructed particle is within 10 cm of the x or y edges, then the event is tagged as exiting the detector from the sides.

Chapter 3

Signal Selection

"Well, I must endure the presence of a few caterpillars if I wish to become acquainted with the butterflies." - Antoine de Saint-Exupéry, The Little Prince

This analysis measures the neutrino interaction event rate on water for neutral current channel that produces a single π^0 in the final state. The π^0 particle decays into two photons, each of which produce an electromagnetic (EM) shower in the PØD. Using the nominal NEUT Monte Carlo, a sequence of selection cuts are optimized to select a sample enriched in NC1π^0 events.

As elaborated in Section 1.3.2, nuclear effects obfuscate the true interaction modes, thus the signal is defined by the particles that exit the nucleus. Specific cross section models have to be invoked to unravel the true interaction mode at the nucleon from the particles observed exiting the nucleus. As these models have not been confirmed by independent data, dependence on such models must be minimized. Thus, the final measurements are made for observed interaction topologies rather than their true interaction mode.

The NC1π^0 interaction signal for this analysis is defined as :

- 1 π^0 exiting the nucleus;
- No outgoing charged leptons;
- No other mesons;
- Any number of nucleons.

3.1 Signal Sample

The signature for selecting a NC1π^0 event in PØD is two reconstructed EM-like showers that are assumed to be the two photons coming from a π^0 decay. Selection cuts are applied to obtain a relatively pure sample of the NC1π^0 events in PØD. The cuts are optimized to maximize efficiency and purity under the reconstructed π^0 invariant mass peak. As the target mass in PØD water-out configuration is less, the radiation length of the photon is higher and it travels a farther distance. Hence, the reconstruction cuts are optimized separately for the two configurations of PØD. All cuts that are applied to obtain sample enriched in NC1π^0 events are stated in the list below. The purpose and effects of each cut will be discussed ahead.

1. **3D Vertex:** A reconstructed 3D vertex in PØD
2. > 1 **particle:** The event should have more than one reconstructed shower particle
3. **Fiducial Volume:** The reconstructed vertex should be in the fiducial volume of PØD
4. **Containment:** All the particles in the event should be completely contained in the PØD
5. π^0 **direction:** Reconstructed direction of $\pi^0 < 60^0$ w.r.t beam axis
6. μ **decay cluster:** Reject events with one or more muon decay cluster
7. **Charge Ratio:** 79 % (74%) of the charge in the event, for the PØD water-in (water-out) configuration, should come from the two highest momentum shower particles
8. **Particle ID:** The two highest momentum shower particles should be EM-like
9. **Shower Separation Distance:** The showers have a separation in space of 90 mm for PØD water-in and 130 mm for PØD water-out configuration.

The 3D vertex cut ensures a well reconstructed event with hits in both X-Z and Y-Z plane of the PØD. At least two reconstructed shower particles are necessary to reconstruct a π^0 particle and its invariant mass, momentum and direction.

Fiducial Volume, Containment and π^0 direction cuts are optimized to ensure good detector performance. The fiducial volume for reconstructing a shower in the PØD was defined in Table 2.1. The distribution of events for data and Monte Carlo in the PØD along the beam axis is shown in Figure 3.1. The excess of data events in the most upstream location in PØD is due to neutrino interactions on the surrounding material are not simulated in the Monte Carlo. The falling off number of events in the downstream position is caused by the requirement that the event be completely contained in the PØD. This trend is matched well between data and Monte Carlo events.

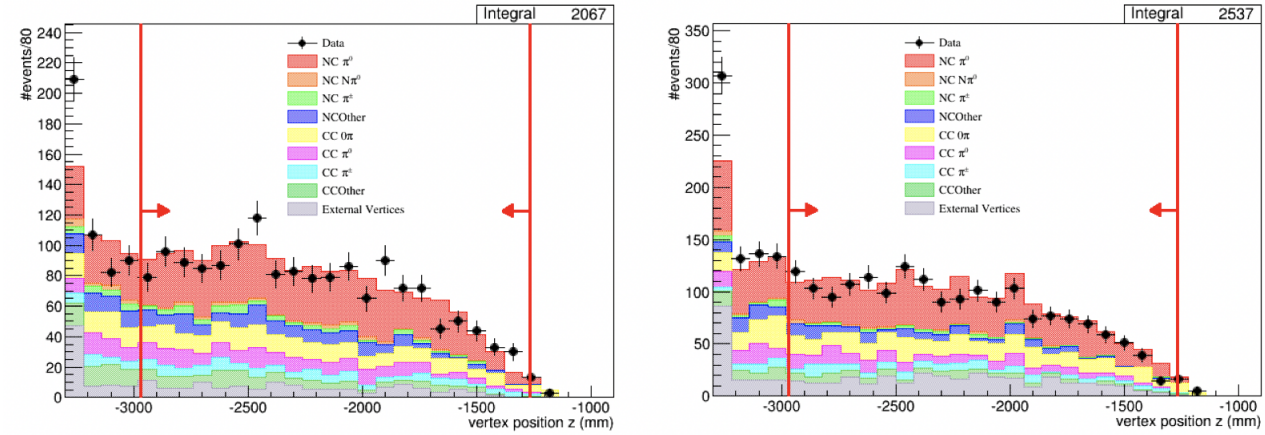

(a) PØD water-in configuration

(b) PØD water-out configuration

Figure 3.1: Distribution of π^0 interaction vertex position in the direction of beam. The histograms are area normalized. The excess of data seen in the first bin (most upstream position of ND280 detector) is due to the neutrino interactions on the surrounding environment not being simulated in the Monte Carlo. The fiducial distance (red line) cut removes these events.

The direction of the π^0 is restricted to less than 60° with respect to the beam axis. Due to the structure of the PØD scintillator bars, the reconstruction performance deteriorates if a particle traveling at a high angle deposits multiple hits in the same scintillator bar. Overall, the reconstruction performs well up to the angle of 75°. To be conservative the cut was fixed at 60° or identically $\cos\theta_z = 0.5$ [12].

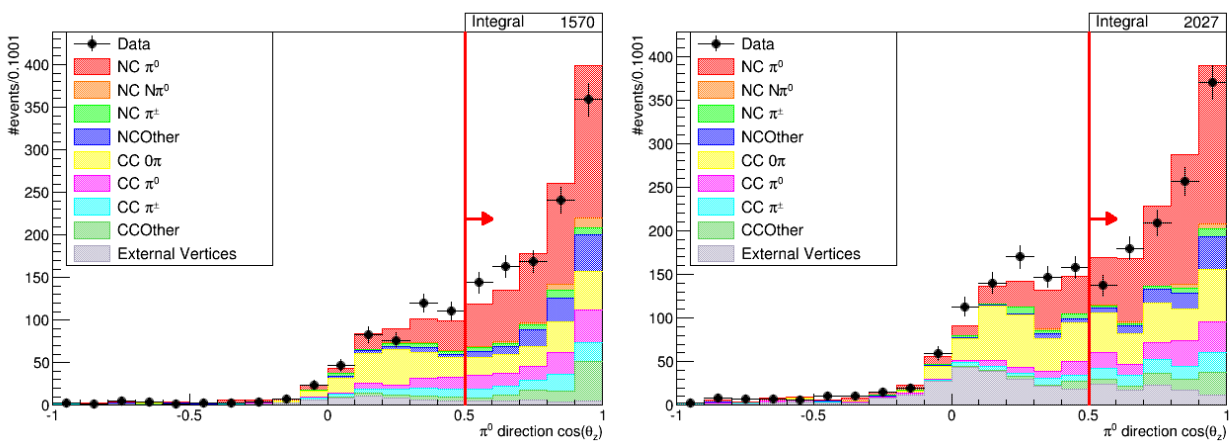

(a) PØD water-in configuration

(b) PØD water-out configuration

Figure 3.2: Distribution of π^0 direction after all other cuts are applied. The histograms are area normalized.

The μ decay cluster cut rejects all events with a time delayed cluster which are expected from the decay of a muon. This intends to remove charged current events from the sample,

Figure 3.3. Events failing this cut but passing all other cuts were used as background control sample to constrain the background events in the fit. Further aspects of this will be discussed in Section 3.2.

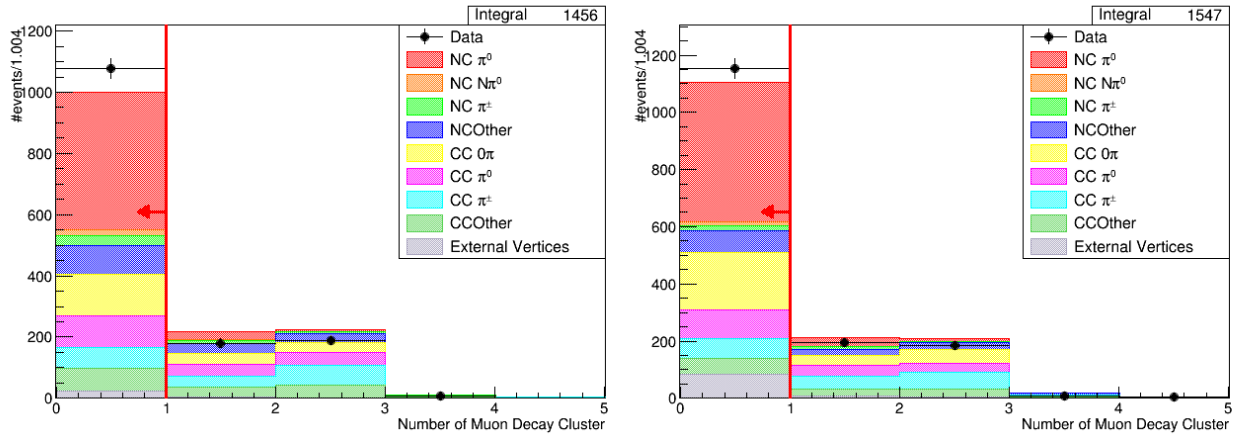

(a) PØD water-in configuration

(b) PØD water-out configuration

Figure 3.3: Distribution of the number of μ decay cluster after all other cuts are applied. The histograms are area normalized.

The cut on the charge deposited by the shower particles is constructed to remove events with too many particles. Most of the charge deposited in the event are required to come from two highest momentum shower particles. The total charge in an event can be divided into three parts :

1. Charge in two highest momentum showers
2. Charge in other reconstructed particles
3. Charge in hits which do not belong to any reconstructed particle

The total charge in the event is thus = (1) + (2) + (3)

The distribution of events as a function of the charge in pair of the above categories is shown in Figure 3.4.

A cut is placed on the fraction of the total charge deposited by the two highest momentum showers [1 / (1+2+3)] at 79%(74%) for the water-in(water-out) samples, shown in Figure 3.5. This cut was modified from the previous analysis to include hits which are not part of any reconstructed particles to evaluate the total charge in the event.

The shower reconstruction algorithm of PØD reconstruction identifies particles as kEM (EM-like showering objects) or kShower (non-EM objects that do not shower). A particle identification weight is assigned to each reconstructed shower object quantifying the likelihood with which the kEM or kShower hypotheses is measured, as explained in Section 2.4.1. A metric for determining if a reconstructed shower object is EM-like is constructed by taking the difference between the kEM and kShower PID Weight. A cut is placed at -1.1 and both the highest momentum showers must pass this cut individually, as shown in Figure 3.6.

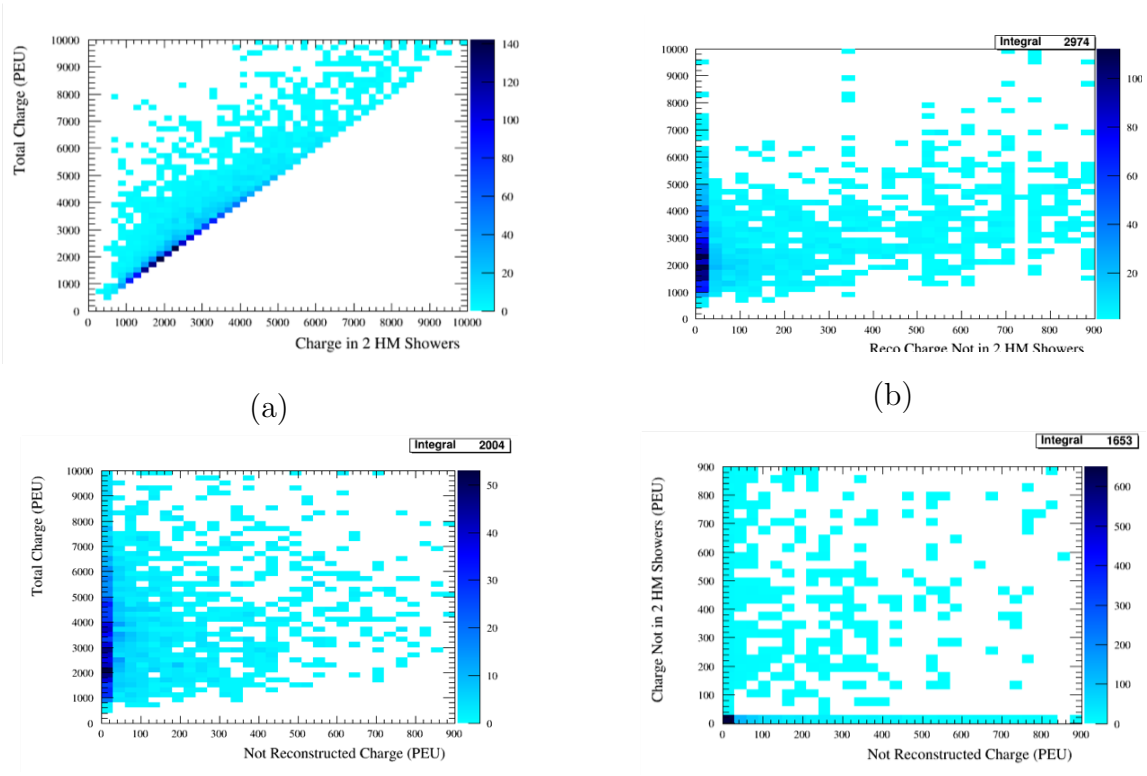

(a) (b) (c) (d)

Figure 3.4: 2D distributions comparing allocation of charge in events. (a) Total charge vs. charge in 2 highest momentum (HM) shower particles. (b) Total charge vs. charge in other reconstructed particles (c) Total charge vs. charge not reconstructed as particles (d) Charge in other reconstructed particles vs. charge not reconstructed as particles

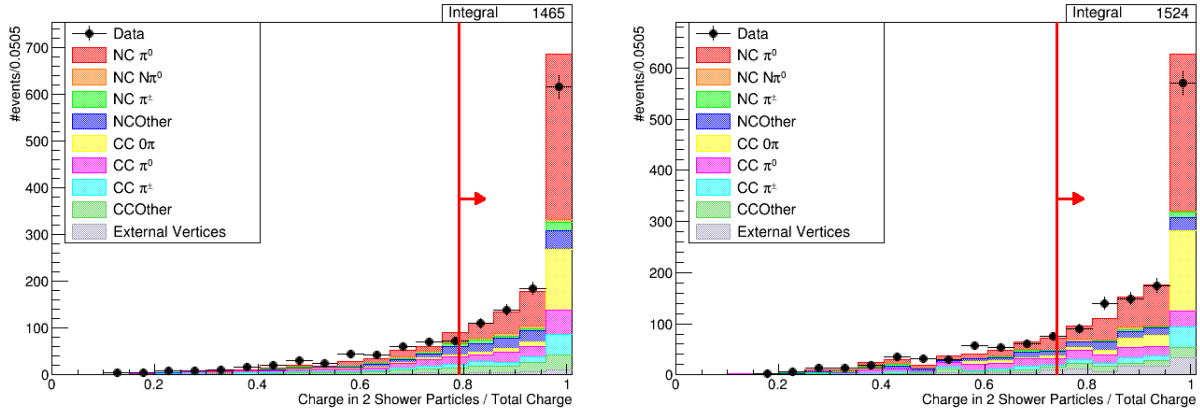

(a) PØD water-in configuration (b) PØD water-out configuration

Figure 3.5: Distribution of the ratio of charge in two highest momentum showers to total charge in the event after all other cuts are applied. The histograms are area normalized.

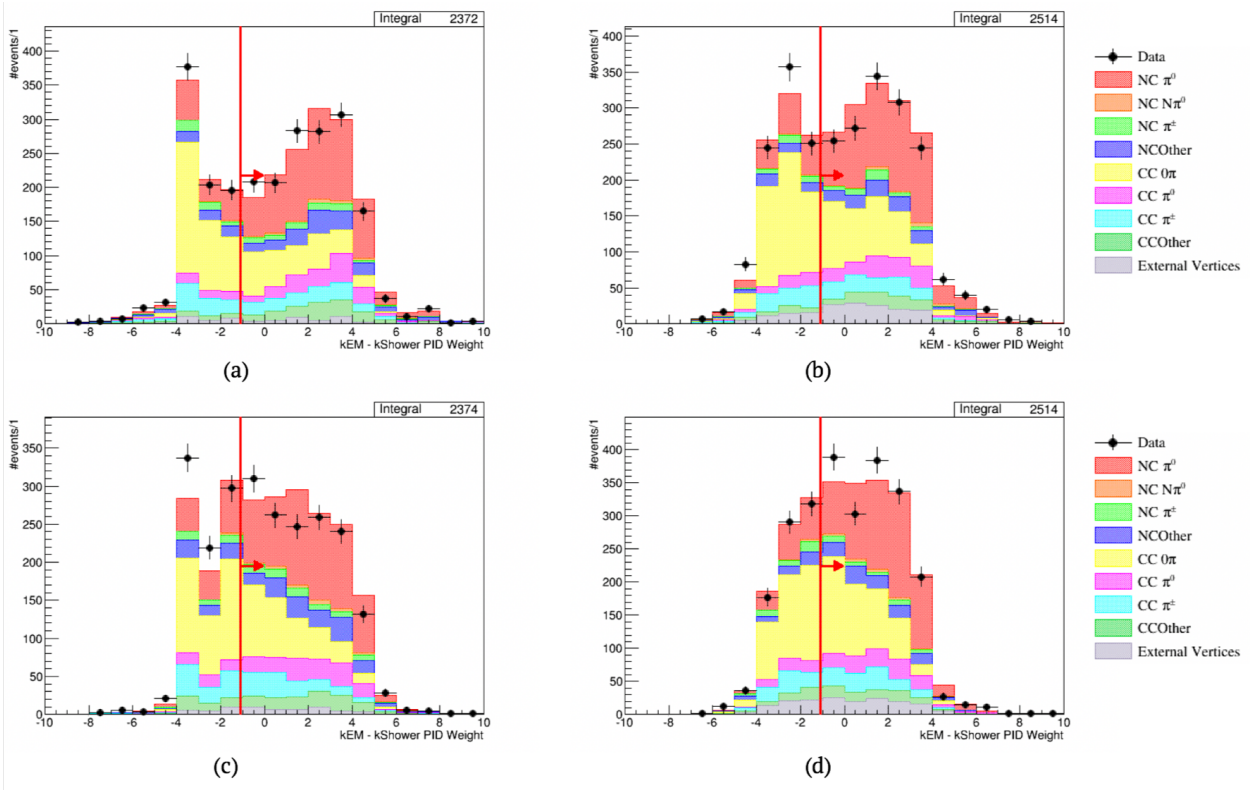

Figure 3.6: kEM PID weight - kShower PID weight distribution after all other cuts are applied for (a) highest momentum shower particle for PØD water-in (b) highest momentum shower particle for PØD water-out (c) second highest momentum shower particle for PØD water-in (d) second highest momentum shower particle for PØD water-out. The plots are area normalized

The shower separation cut was completely redesigned from its definition in the previous generation analysis. Earlier it was defined as the minimum distance between two hits in separate shower particles. The problem with this method is that the measurement is contingent on a single hit of the particle which could be noise. This contributed to the high systematic error on the previous measurement. This cut was modified to include information from all the hits in the shower particles weighted by their charge. Based on the position and the charge of the hits, a covariance matrix can be constructed which encodes the information of the distribution of the hits weighted by their charge. Using the centroid and covariance matrix, a boundary of the shower can be drawn. Minuit is used to fit the minimum distance between the two boundaries of the shower particles. A schematics is shown in figure 3.7.

This calculation is performed separately for each plane (X-Z and Y-Z) because although we require the vertex to be reconstructed in 3D, a particle can have hits in only one of the two 2D plane. Moreover, as previously mentioned, a shower particle is constructed from $\sim 3-5$ clusters. The boundary is drawn for each cluster of both particles. We calculate the minimum distance between all the clusters of both shower particles, for each 2D plane separately. Then the maximum of the two distances in the XZ and YZ plane is taken as the distance between the two shower particles. This is done because even if one of the projections

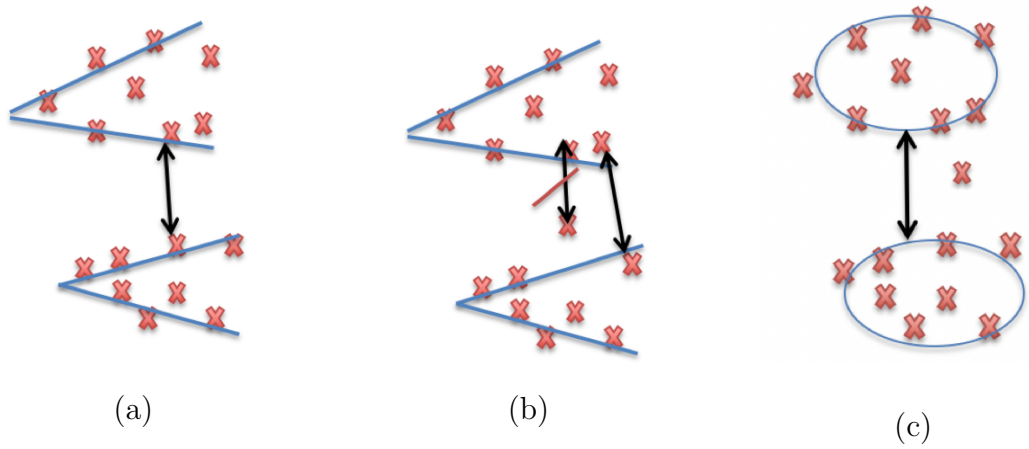

Figure 3.7: (a) Distance between two showers using minimum hit distance as defined by previous analysis . This is dependent on individual hits. (b) Measurement could be incorrect due to presence of noise. (c) New definition using position of all charge weighted hits.

of two 3D objects overlap i.e. minimum distance is zero, they could still be separated in 3D space, as shown in the Figure 3.8.

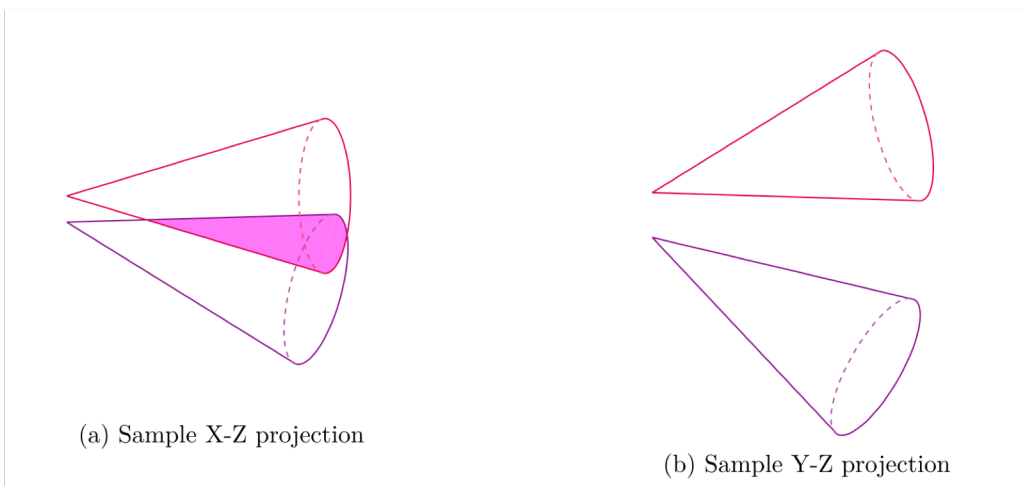

Figure 3.8: Shower particles which are spatially separated in 3D could still have an overlap in one 2D projection. Figure taken from [12].

The cut is placed at 90 mm for the PØD water-in and 130 mm for the PØD water-out configurations respectively.

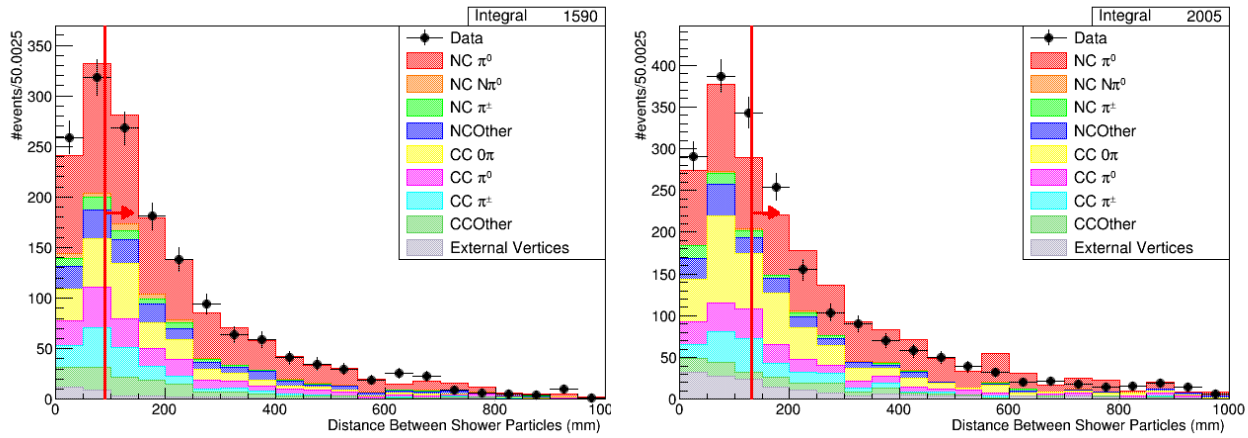

(a) PØD water-in configuration

(b) PØD water-out configuration

Figure 3.9: Distribution of minimum separation between two reconstructed shower particles after all other cuts are applied. The plots are area normalized.

3.1.1 Selection Efficiencies

The data to be used for this analysis consists of following T2K runs:

T2K Run	PØD Water-In (POT)	PØD Water-Out (POT)
Run 1	0.17 E+20	
Run 2	0.43 E+20	0.36 E+20
Run 3		1.58 E+20
Run 4	1.62 E+20	1.73 E+20
Run 8	1.31 E+20	3.03 E+20
Total	3.53 E+20	6.70 E+20

Table 3.1: Proton on Target (POTs) collected by T2K data runs in neutrino mode that are used for this analysis. Data for Run 5 - Run 7 was taken in antineutrino mode which is not analyzed for this analysis.

The signal enriched samples are obtained by applying the cuts described in the previous section. The reconstructed π^0 invariant mass distribution for the selected sample is shown in Figure 3.28. Distribution of true energy of the incoming neutrino that produce the events in the selected sample is shown in Figure 3.11.

There are many different ways to define the efficiency of the selection. Numbers useful for evaluating efficiencies and purity of selected samples are listed in Table 3.2 and 3.3. Table 3.2 gives the number of true NC1π^0 signal events that were generated by the Monte Carlo with specific topologies while the Table 3.3 lists the true signal events which were reconstructed by the software in those topologies.

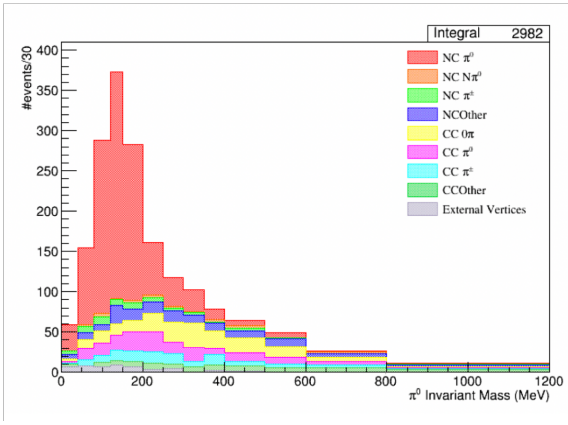

(a) PØD water-in configuration

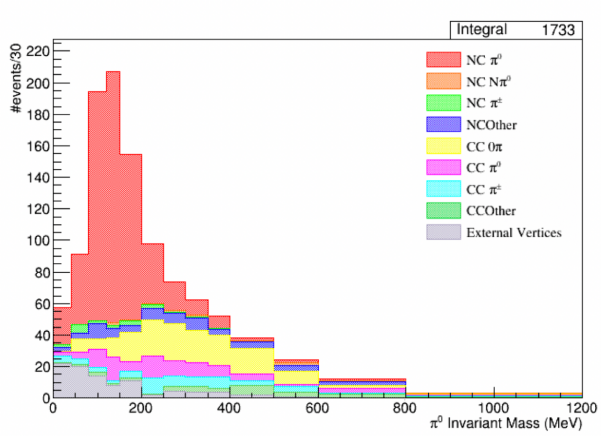

(b) PØD water-out configuration

Figure 3.10: Distribution of invariant mass of reconstructed π^0 particles after applying all selection cuts for Monte Carlo only.

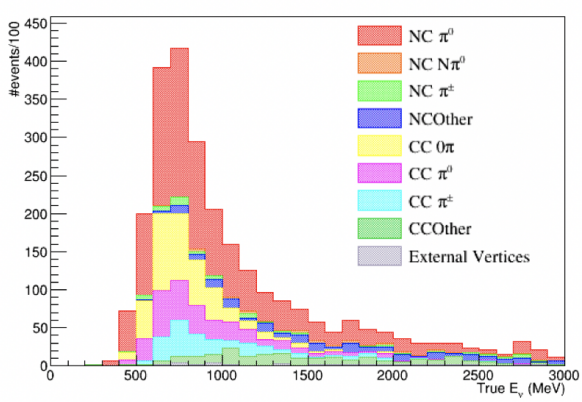

(a) PØD water-in configuration

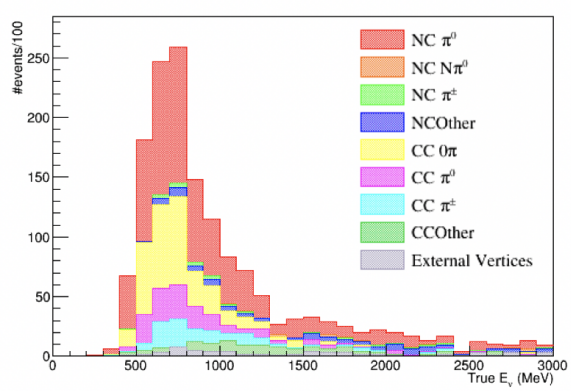

(b) PØD water-out configuration

Figure 3.11: Distribution of true incoming neutrino energy for events passing all selection cuts for Monte Carlo only.

	Water-In	Water-Out
Signal events w/ vertex generated in PØD	56586	45009
Signal events w/ vertex generated in PØD FV	24817	15962
Signal events w/ vertex generated in PØD FV + π^0 dir $< 60°$	14276	9043

Table 3.2: Number of NC1π^0 events generated by Monte Carlo in the topology described in Column 1.

	Water-In	Water-Out
Signal events w/ vertex reconstructed in PØD FV	21410	14812
Signal events after all cuts	1363	766
Signal events after all cuts w/ Invariant Mass < 500 MeV	1320	748
Total events after all cuts	3037	1737
Total events after all cuts w/ Invariant Mass < 500 MeV	2496	1528

Table 3.3: Number of NC1π^0 events with reconstructed topology described in Column 1.

The previous analysis limited the fit to a reconstructed Invariant Mass of less than 500 MeV. Thus a direct comparison to those numbers is provided. The purity of the sample is defined as the ratio of signal events to all events in the final selected sample. Table 3.3 shows that the purity of selected sample is $(52.9 \pm 1.8)\%((48.9 \pm 2.2)\%)$ for PØD water-in(water-out) configuration. The ratio of all selected signal events to those generated in PØD fiducial volume is 5.3% (4.7%) for water-in (water-out) configuration. Comparing these numbers to previous result stated in Section 1.3.3, it can be seen that the purity of the water-in sample increased by 4% while the efficiency decreased by $< 1\%$. For the water-out sample, the purity increased by 2% with the efficiency remaining constant. However, it is important to look at the efficiency of the sample with respect to the π^0 kinematics. Figure 3.12 shows the π^0 kinematics phase space of all signal events generated in PØD fiducial volume by NEUT and the signal events in the selected sample. The efficiency of selecting NC1π^0 events in this phase space is shown in Figure 3.13.

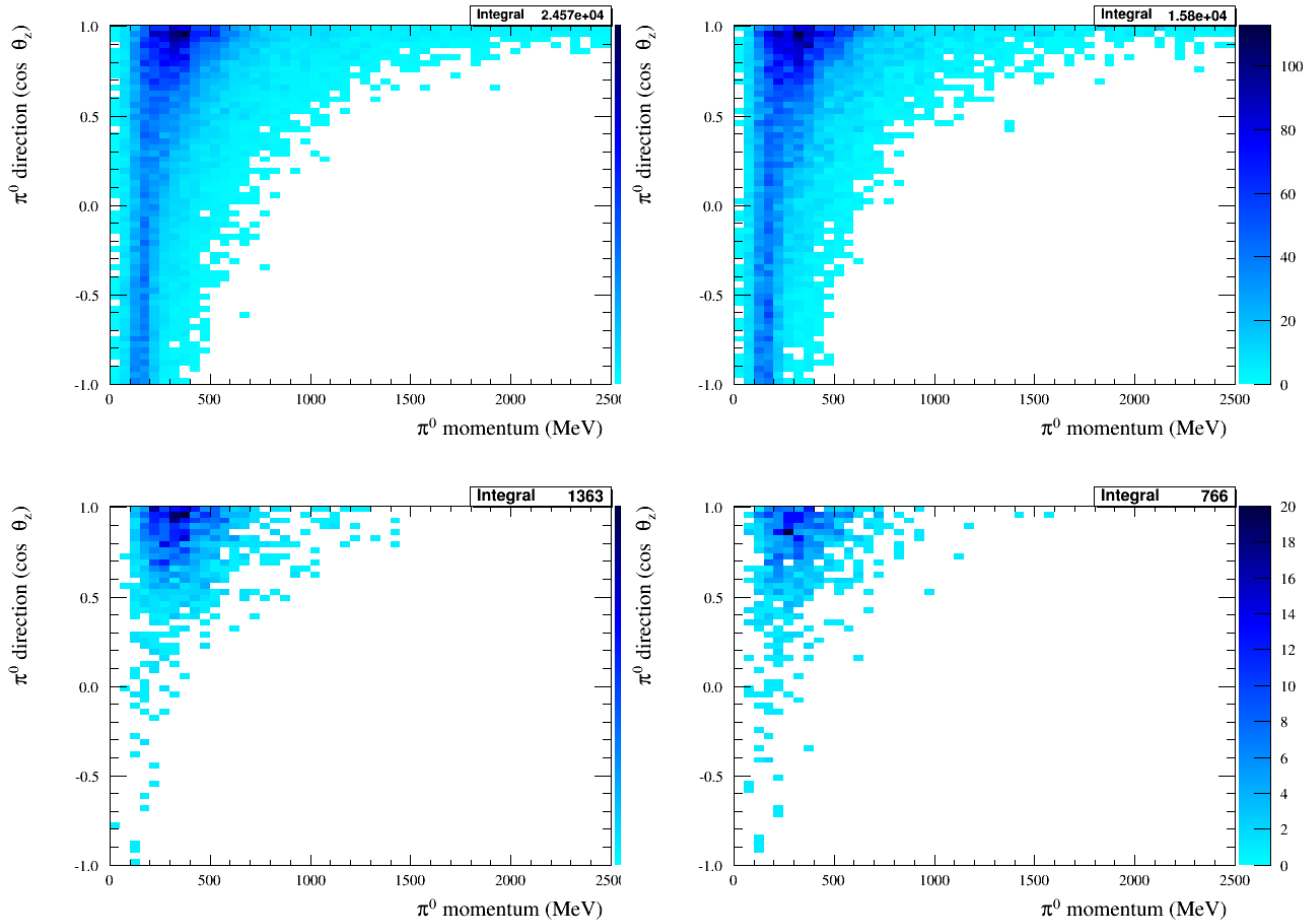

Figure 3.12: π^0 kinematics phase space for signal events generated in true PØD fiducial volume (top) and signal events in selected sample (bottom) for PØD water-in (left) and water-out(right) configuration.

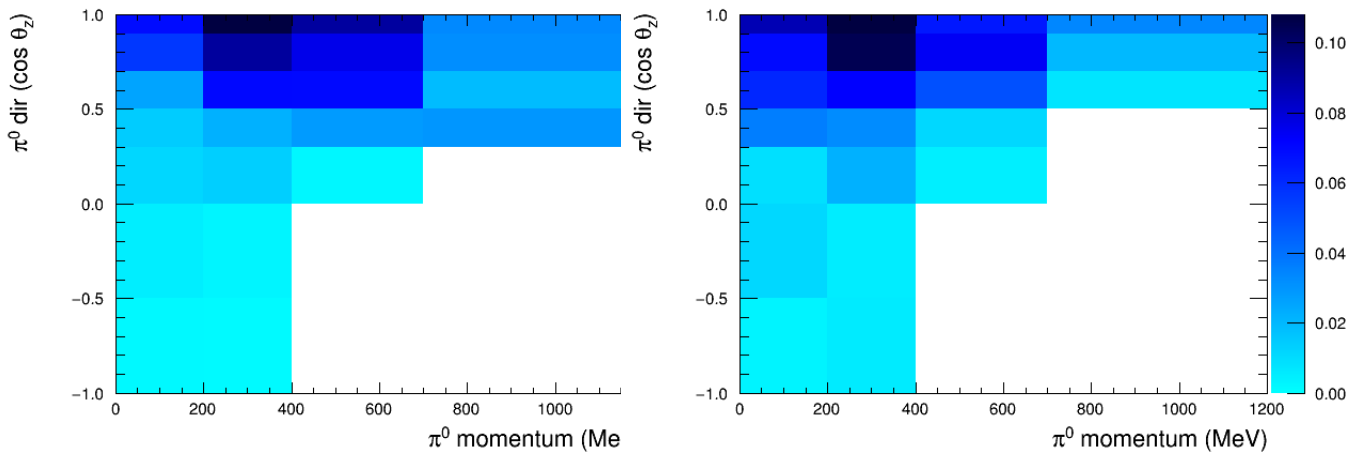

Figure 3.13: Ratio of signal events in the selected sample to all signal events generated in PØD fiducial volume in π^0 kinematics phase space for PØD water-in (left) and water-out (right) configuration.

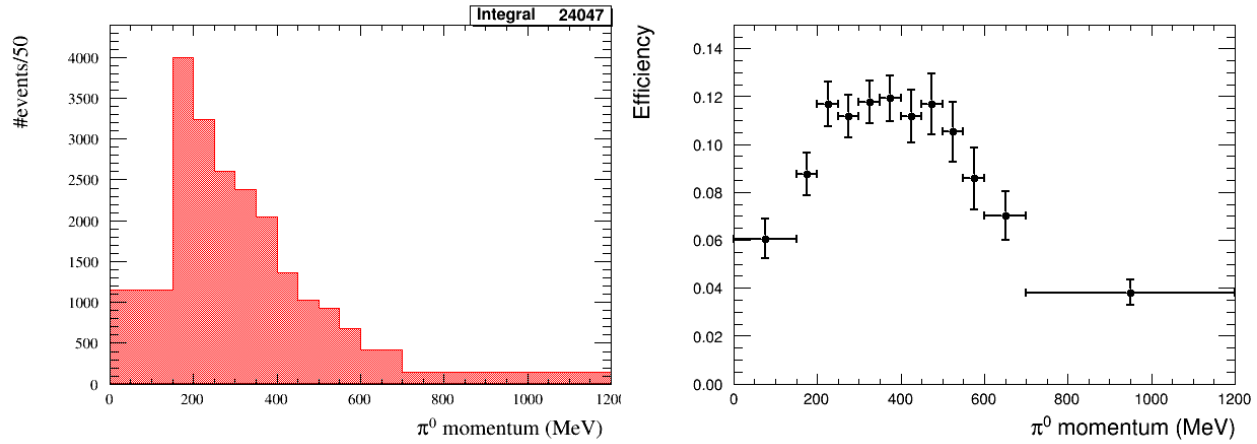

Figure 3.14: True π^0 momentum distribution of signal events generated in PØD fiducial volume with π^0 direction $< 60^0$ to z axis (left) and the efficiency of selecting signal events (right) as a function of true pizero momentum for PØD water-in configuration.

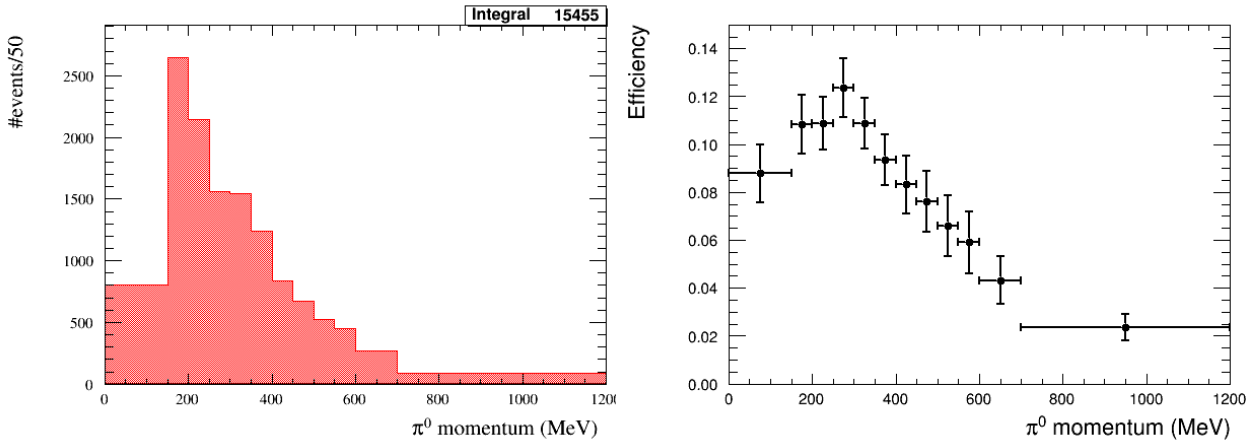

Figure 3.15: True π^0 momentum distribution of signal events generated in PØD fiducial volume with π^0 direction $< 60°$ to z axis (left) and the efficiency of selecting signal events (right) as a function of true pizero momentum for PØD water-out configuration.

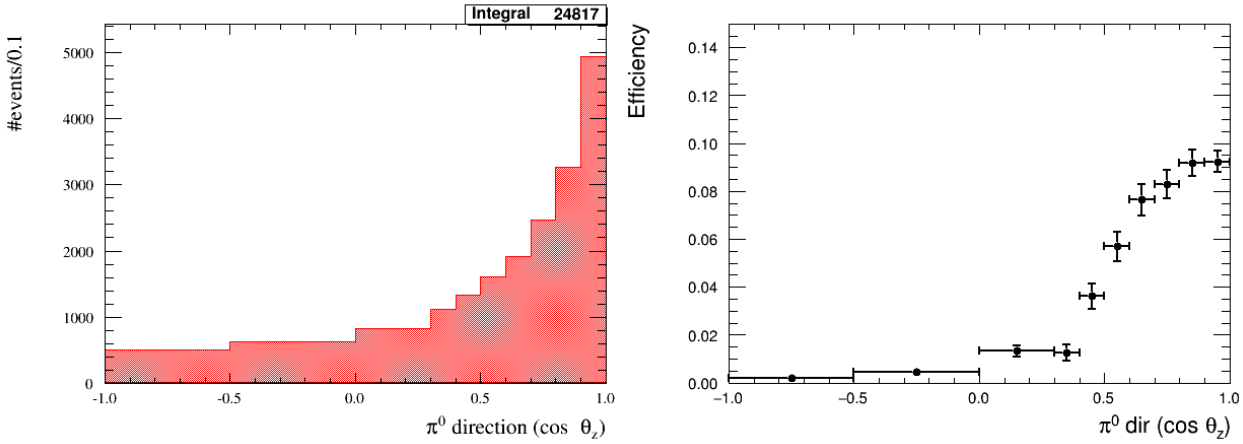

Figure 3.16: True π^0 direction distribution of signal events generated in PØD fiducial volume (left) and the efficiency of selecting signal events (right) as a function of true pizero direction for PØD water-in configuration.

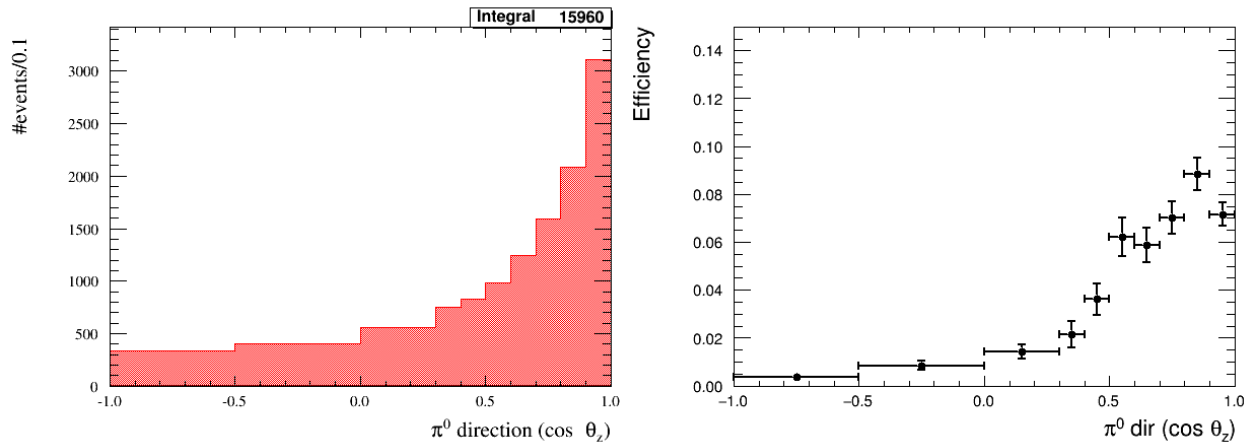

Figure 3.17: True π^0 direction distribution of signal events generated in PØD fiducial volume (left) and the efficiency of selecting signal events (right) as a function of true pizero direction for PØD water-out configuration.

It is important to carefully consider the efficiency of the selected sample. The selected signal events have to be corrected by their selection efficiency before a comparison to cross section models can be made. A small value of efficiency would result in just the Monte Carlo being reproduced. Ideally, the efficiency of signal selection would only be a function of detector resolutions without any dependence on π^0 kinematics or interaction variables that affect the underlying cross section such as four-momentum transfer (Q^2) or the invariant mass of the interacting particles W. This limits excessive dependence on models during efficiency correction which is an inherently Monte Carlo dependent step. However, for a low statistic analysis such as NC1π^0, it remains a difficult task. Evidently, the efficiency of selecting high angle and backwards going π^0 is very small due to the cut on reconstructed π^0 angle to be $< 60°$. The efficiency also takes a dip for very high π^0 momentum. As shown in Figure 3.18, high momentum π^0 particles are extremely forward going. This implies that the angle between two decay photons, knowns as the opening angle, is very small. For such small values of opening angle, the reconstruction is likely to mis-reconstruct two decay photons as one single shower particle. Cut on minimum shower separation and PØD containment also affect the efficiency of high momentum π^0 particles.

For the purpose of this analysis, the efficiency is defined as the ratio of selected signal events to all signal events generated with a vertex in PØD fiducial volume and the π^0 direction $< 60°$ to z axis. Table 3.2 and Table 3.3 shows that the efficiency is $(9.2\pm0.3)\%((8.3\pm0.3)\%)$ for PØD water-in(water-out) configuration where the errors are statistical.

The Q^2 and W distribution for NC1π^0 interaction, along with the efficiency in those variables are presented in Figures 3.19, 3.20, 3.21 and 3.22. The efficiency in these parameters while not absolutely flat is relatively stable between adjacent bins with substantial population of events.

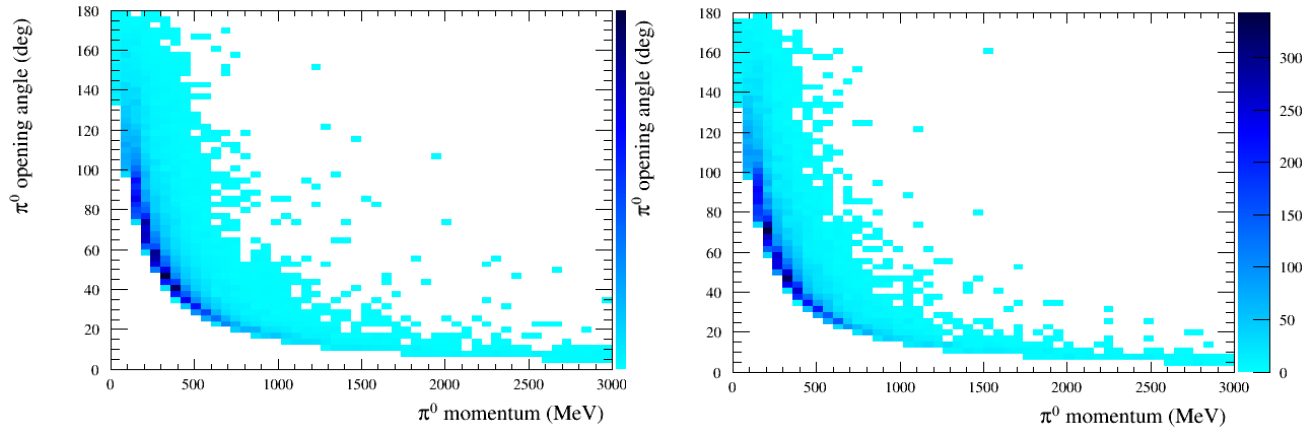

(a) PØD water-in configuration

(b) PØD water-out configuration

Figure 3.18: Distribution of true simulated opening angle of π^0 decay particles w.r.t. π^0 momentum for signal events generated in PØD fiducial volume. High momentum π^0 particles are extremely forward going.

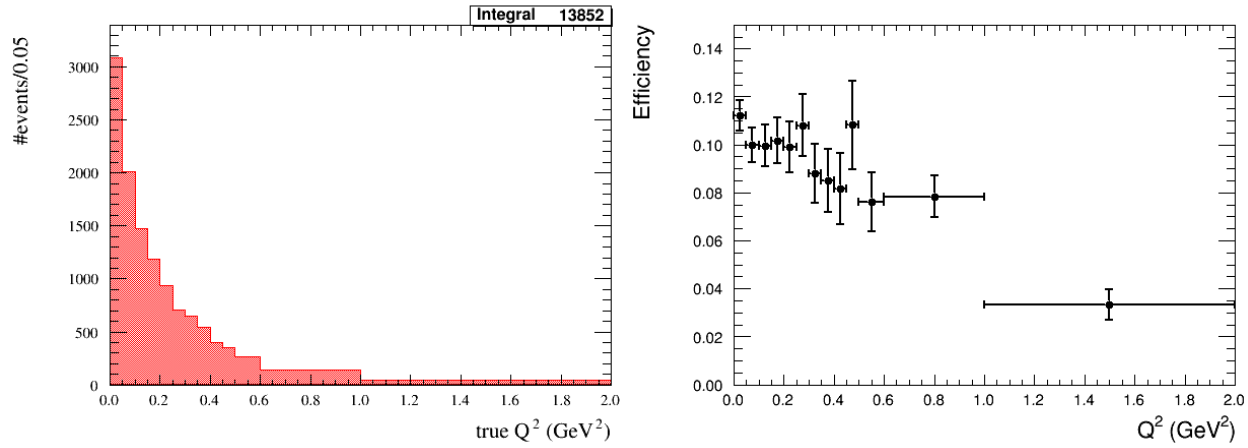

Figure 3.19: True Q^2 distribution of signal events generated in PØD fiducial volume with π^0 direction $< 60^0$ to z axis (left) and the efficiency of selecting signal events (right) as a function of true Q^2 for PØD water-in configuration.

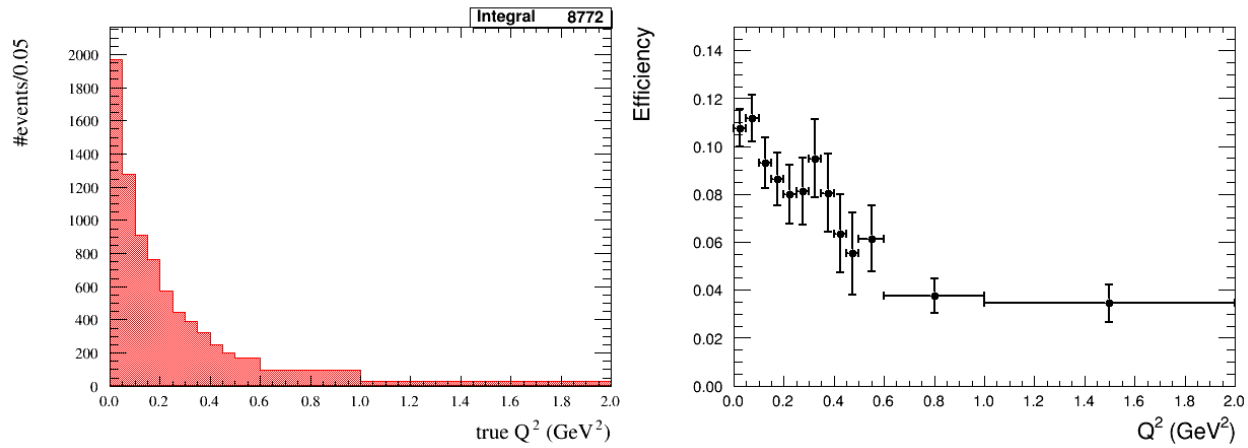

Figure 3.20: True Q^2 distribution of signal events generated in PØD fiducial volume with π^0 direction $< 60^0$ to z axis (left) and the efficiency of selecting signal events (right) as a function of true Q^2 for PØD water-out configuration.

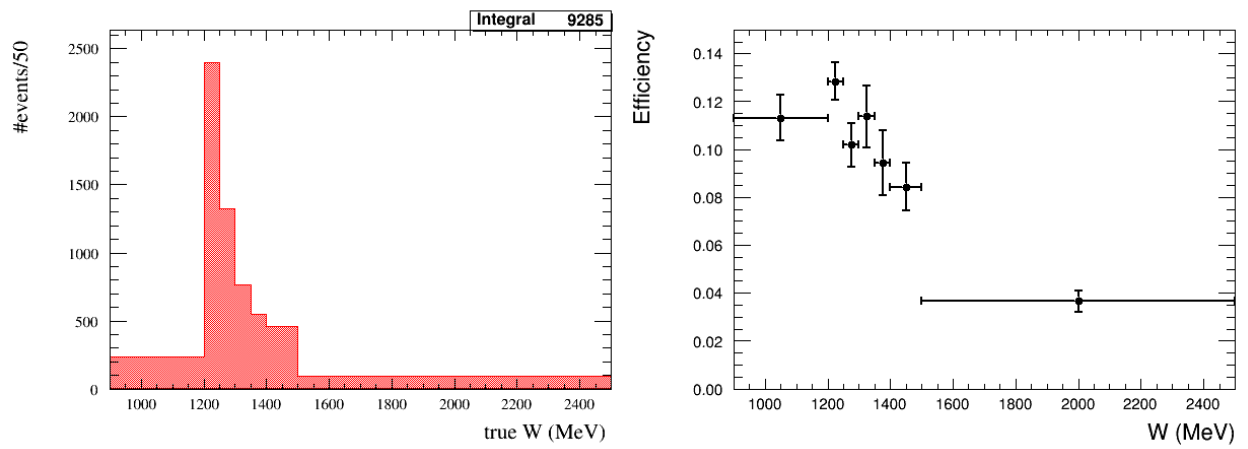

Figure 3.21: True W distribution of signal events generated in PØD fiducial volume with π^0 direction $< 60^0$ to z axis (left) and the efficiency of selecting signal events (right) as a function of true W for PØD water-in configuration.

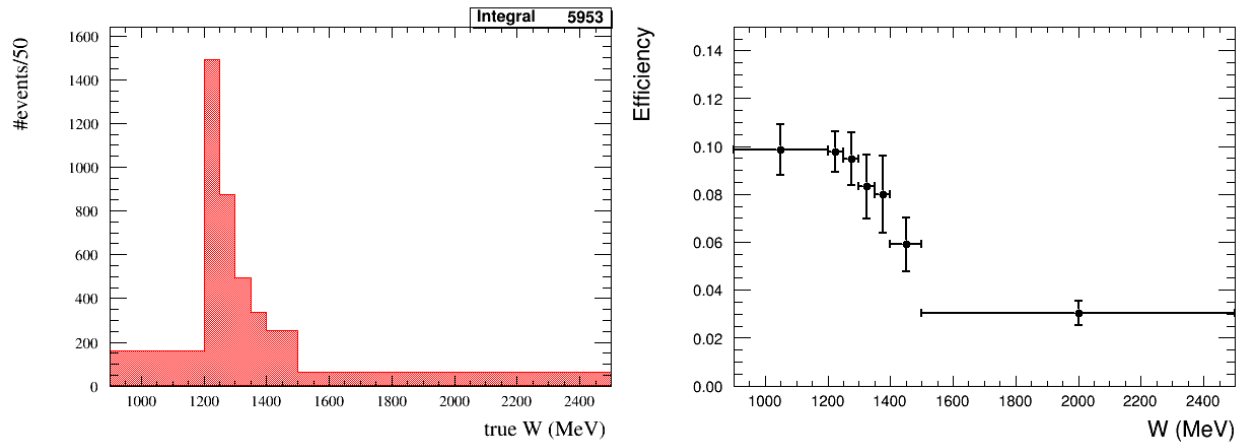

Figure 3.22: True W distribution of signal events generated in PØD fiducial volume with π^0 direction $< 60^0$ to z axis (left) and the efficiency of selecting signal events (right) as a function of true W for PØD water-out configuration.

3.1.2 Reconstructed particles - True π^0 Association

The two selected shower particles are assumed to be the π^0 decay photons. Their deposited charge and direction are combined to reconstruct the π^0 particle. However, this is not an accurate assumptions for all events. This is not a problem for background events as they are falsely reconstructed as two shower events to begin with. For signal events, it is essential to correctly identify the π^0 decay photons to obtain meaningful values for the π^0 invariant mass and kinematics. It is not a straightforward task as both showers could be reconstructed from the same photon in case of an asymmetric decay, or one shower could be formed from the hits of the proton or even from a secondary π^0. For tracker based analysis, the same gamma can leave multiple signature e^+/e^- tracks and/or shower in the ECal. The recombination of all the reconstructed objects to form the π^0 particle is a complicated exercise. In the PØD, it is simpler to match the photons to the primary π^0 as they shower quickly and the selection cuts require all particles to be contained within the PØD. This makes the PØD performance better than other ND280 detectors. Figure 3.23, shows how the true particles contribute to the reconstructed shower particles.

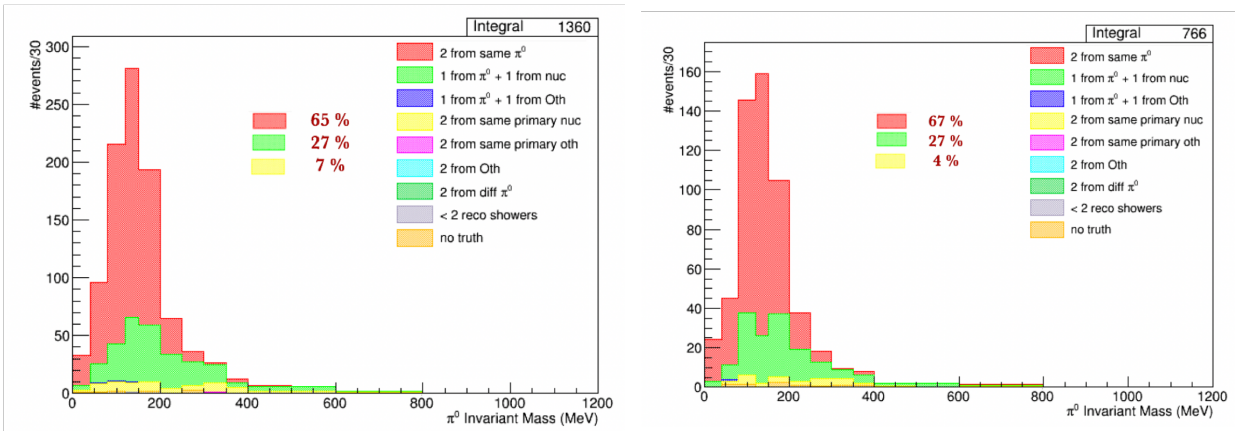

Figure 3.23: π^0 Invariant Mass distribution of signal events in selected sample, detailing contributions of true particles to reconstructed shower particles, for PØD water-in (left) and water-out (right) configurations.

For the selected signal events, 65%(67%) times both reconstructed shower particles come from the same primary π^0 and 27%(27%) of times it is a combination of π^0 decay photons and the nucleon. So for over 90% of the times we correctly identify the decay gammas. The contamination of hits from the proton is substantial but this is usually in the cases where the proton is collinear with one of the gammas and has a relatively smaller momentum to not get classified as an independent particle. This is evident from the π^0 momentum and direction resolution plots. In Figure 3.24, comparing the momentum resolution for all selected signal events with those signal events where both reconstructed shower come from the same primary π^0 (Red category in Figure 3.23), it is evident that the bias in the resolution towards slightly higher values for reconstructed momentum as compared to true π^0 momentum comes from the contribution of the proton hits in reconstructed shower particle. The reconstructed π^0 direction agrees well with the true direction, Figure 3.26, showing that most of mis-reconstructed protons are collinear with the decay gammas. It is the π^0 direction cut which cuts off the lower tail of the relative π^0 direction resolution, Figure 3.27, as expected.

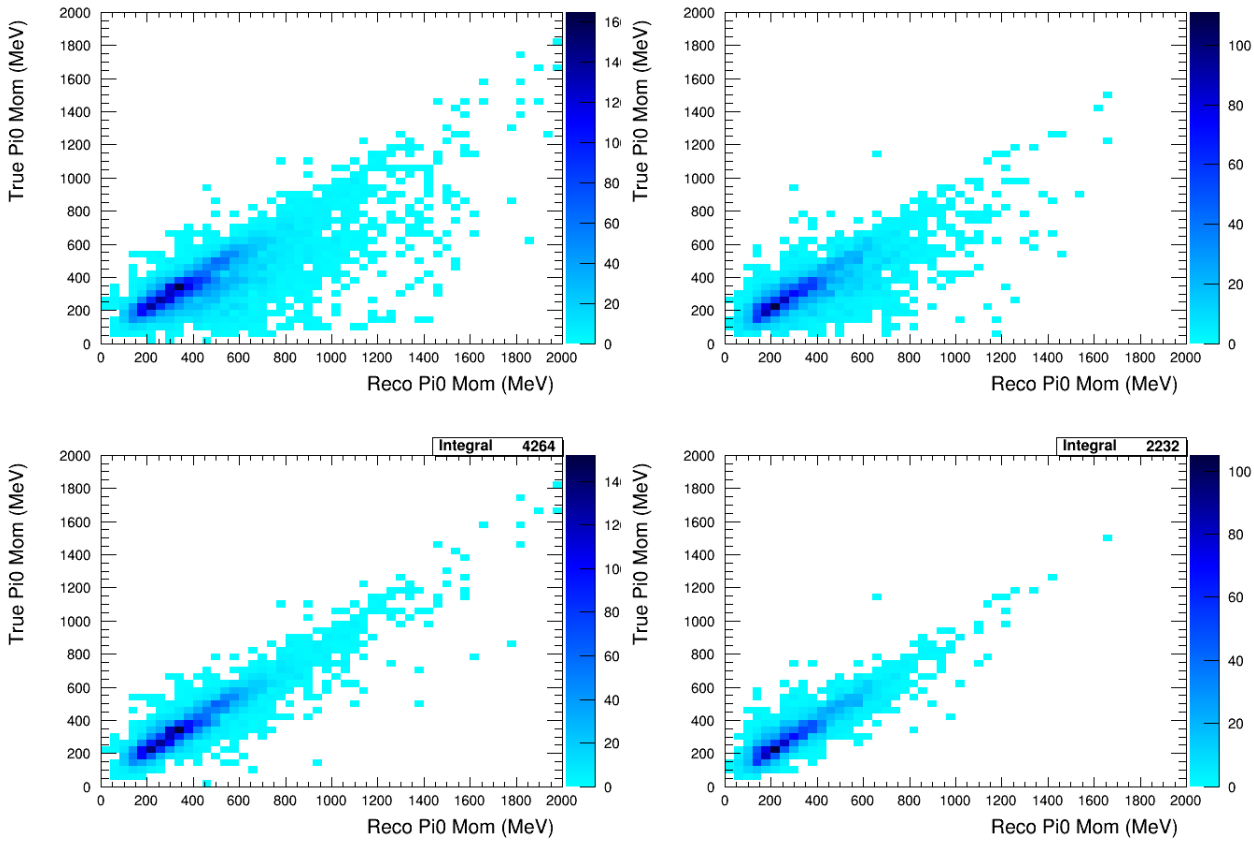

Figure 3.24: True vs. reconstructed π^0 momentum for all selected signal (top) and for signal events where both reconstructed shower come from the same primary π^0 (bottom) for PØD water-in (left) and water-out (right) configurations.

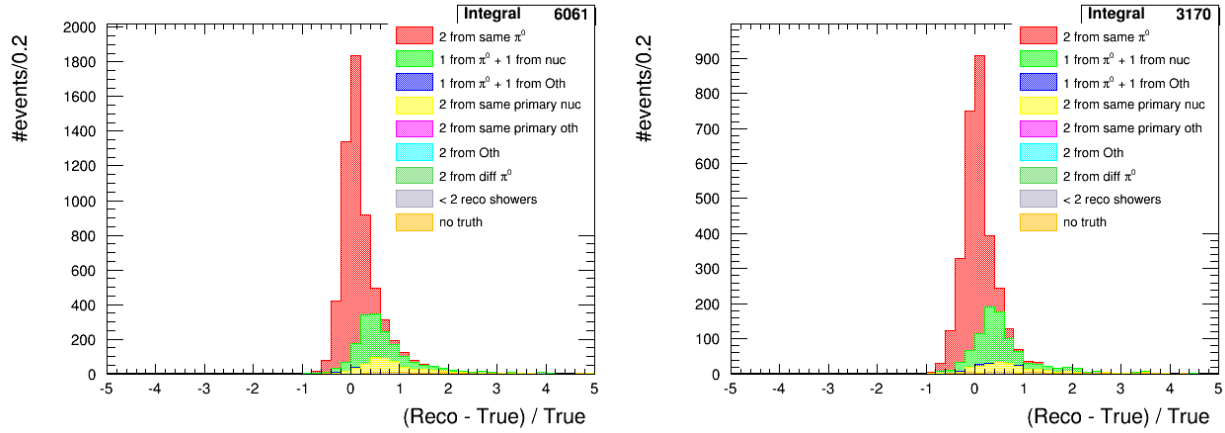

Figure 3.25: Relative momentum resolution for all selected signal events for PØD water-in (left) and water-out (right) configurations.

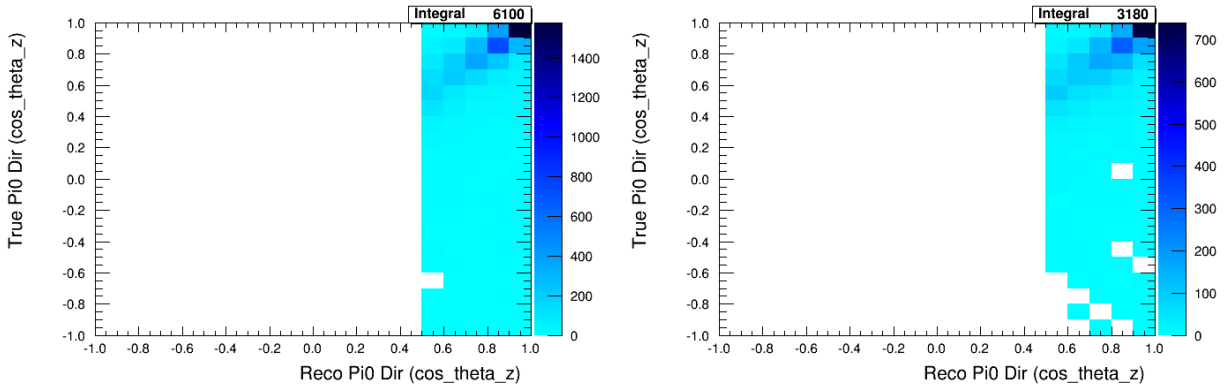

Figure 3.26: True vs reconstructed π^0 direction for all selected signal events for PØD water-in (left) and water-out (right) configurations.

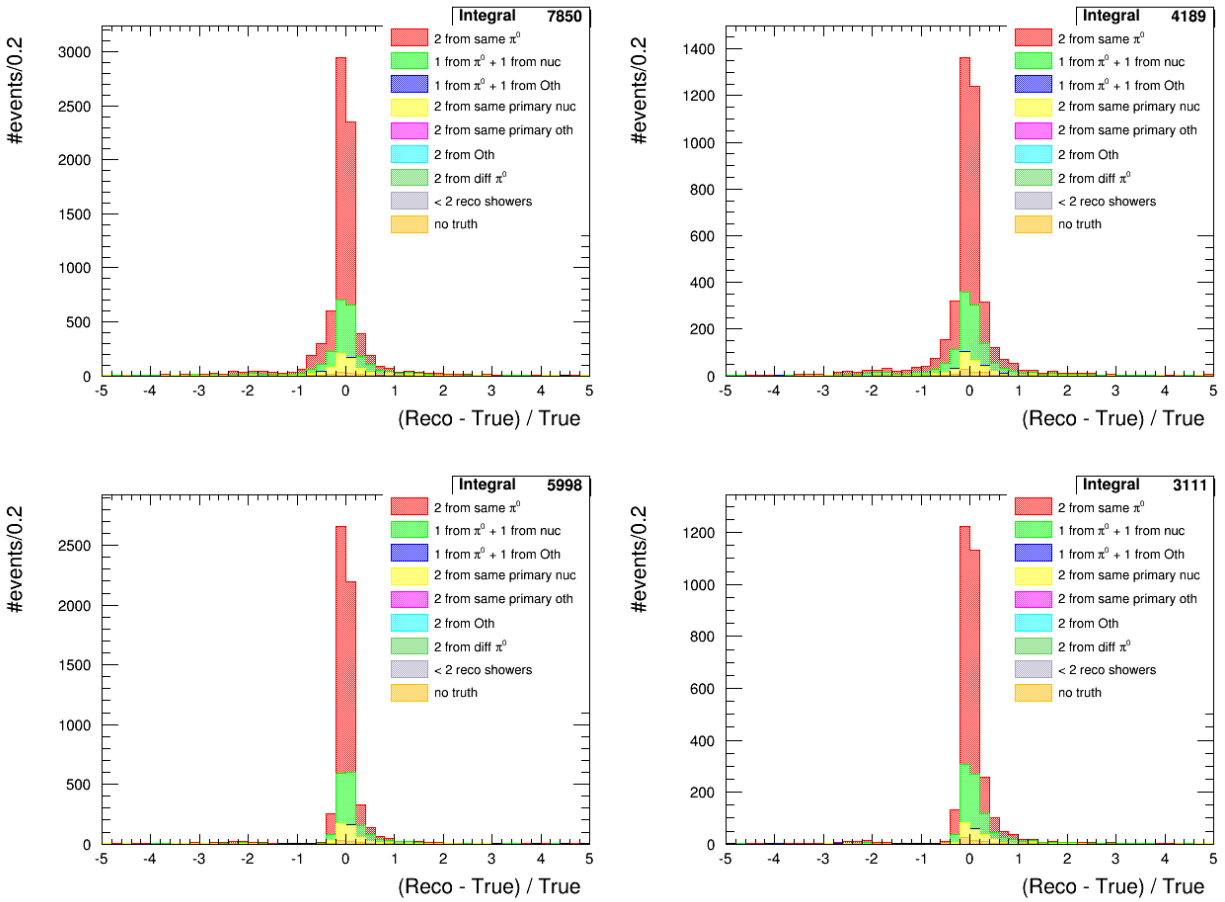

Figure 3.27: Relative π^0 direction resolution for all selected signal events before applying π^0 direction cut (top) and after applying the cut (bottom), for PØD water-in (left) and water-out (right) configurations.

3.2 Background Control Sample

A control sample is used to constrain the background in the selected sample. This control sample is selected by inverting the μ decay cut i.e. events that pass all other cuts, listed in Section 3.1 but have at least one time delayed cluster tagged by muon decay cluster reconstruction algorithm.

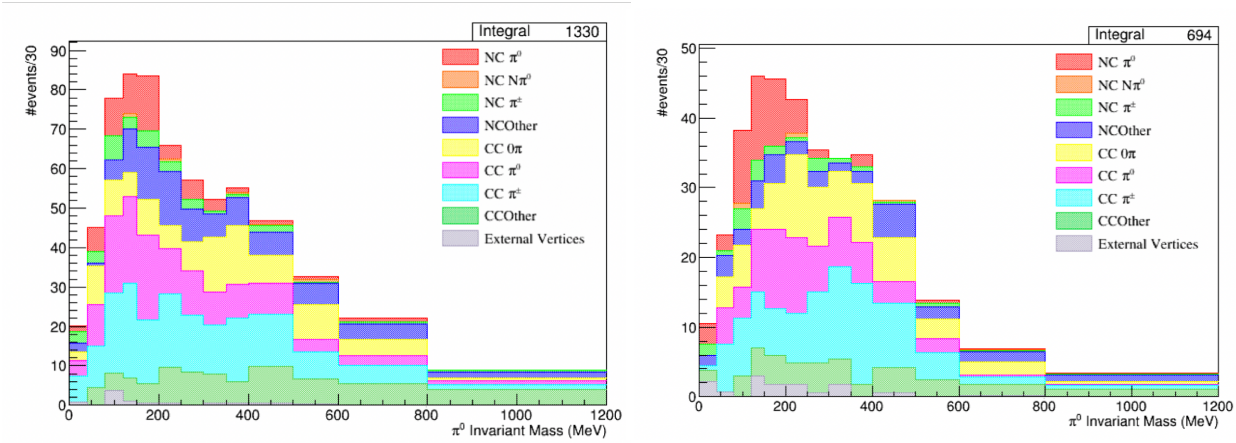

(a) PØD water-in configuration

(b) PØD water-out configuration

Figure 3.28: Reconstructed π^0 invariant mass distribution of the background control sample.

The background control sample constrains the selected sample in two important ways. An overall normalization constraint is provided by introducing two parameters - fake μ decay tag and μ decay tag efficiency. The fake μ decay tag parameter constrains the ratio of the signal in the selected and the background control sample as it can move signal events from background control sample to selected sample which had a fake μ decay cluster tag from reconstruction. While the μ decay tag efficiency constrains the ratio of background events in the two samples by moving background events from selected sample to background control sample which were mis-classified due to reconstruction inefficiencies. These parameters, with priors on their values, are entered into the fit which simulatenously fits the selected and the background control sample of Monte Carlo and data, described in further detail in Chapter 5. The other task of the background control sample is to constrain the errors on the cross section parameters used to evaluate cross section systematic uncertainties. The important criteria for a control sample to provide good constraints to selected sample is that it should be composed of similar interactions and the particles occupy the same kinematic phase space in both samples because the parameters that constrain the background control sample are extrapolated to background events in the selected sample. Table 3.4 compares the fraction of various interaction topologies present in the background events of the selected sample as compared to background events in the background control sample. CC 0π is the largest background in the selected sample while CC$\pi^\pm$ is the largest fraction present in the background control sample. Other event topology fractions are comparable to each other.

As the largest contributor, the kinematics phase space of muons in CC0π and CC$\pi^\pm$ interaction topologies in the selected and background control sample is highlighted, Figure

Event Topology	SS Water-In	BCS Water-In	SS Water-Out	BCS Water-Out
CC0π	24.5%	16.2%	32.3%	21.3%
CC 1π^0	18.8%	18.6%	16.4%	17.8%
CC $\pi^\pm$	12.2%	25%	11.2%	27.3%
CC Other	13.4%	18.7%	8.8%	13.9%
NC $N\pi^0$	3.9%	0.5%	2.2%	0.6%
NC $\pi^\pm$	5.4%	4.1%	3.2%	3.8%
NC Other	17.6%	15.5%	12.4%	12.1%
External to P0D	4.2%	1.3%	13.6%	3.2%

Table 3.4: Percentage breakdown of background events in the selected sample (SS) and background control sample (BCS) for P∅D water-in and water-out configuration. CC 0π is the largest background in the SS while CC$\pi^\pm$ is the largest fraction in the BCS. Other event topology fractions are relatively equal.

3.29 and 3.30. The CC0π selected sample has a high momentum muon tail which seems to be absent from the background control sample. This could be a statistical fluctuation since the opposite could be seen from the CC1$\pi^\pm$ sample which "arguably" has a high momentum tail in background control sample. It is pertinent to note the effect of momentum distribution of muons on the variable in which the fit is performed i.e. the reconstructed π^0 invariant mass distribution. Figures 3.31 and 3.32 show 2D distributions of muon momentum vs. reconstructed invariant mass for selected and background control sample for both P∅D water-in and water-out configurations. It is safe to conclude that the shape of invariant mass distribution is independent of muons kinematics. Hence, a small difference in the kinematics phase space of muon between selected sample and background control sample will not adversely affect the fit as it does not alter the background shape beneath the signal in π^0 mass distribution. The dependence of π^0 invariant mass distribution on true Q^2 of the neutrino interaction in CC0π and CC1$\pi^\pm$ was also investigated resulting in the same conclusion.

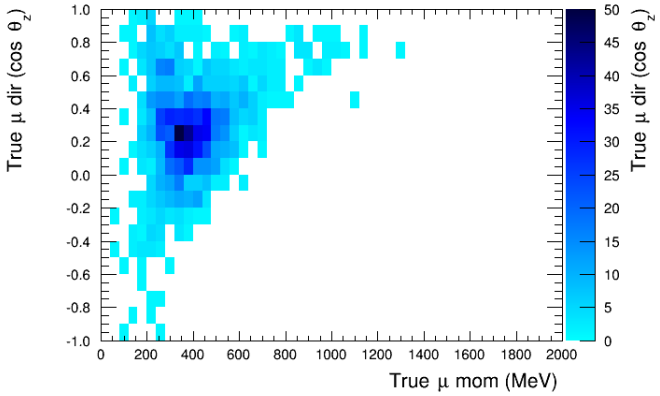

(a) PØD water-in configuration

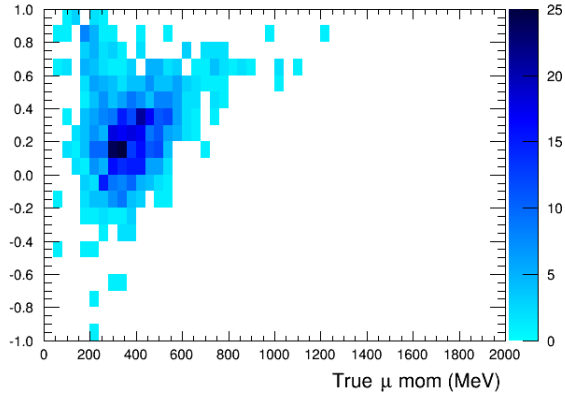

(b) PØD water-out configuration

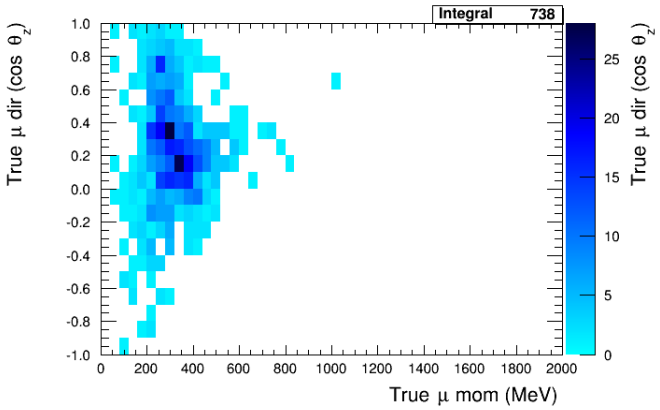

(c) PØD water-in configuration

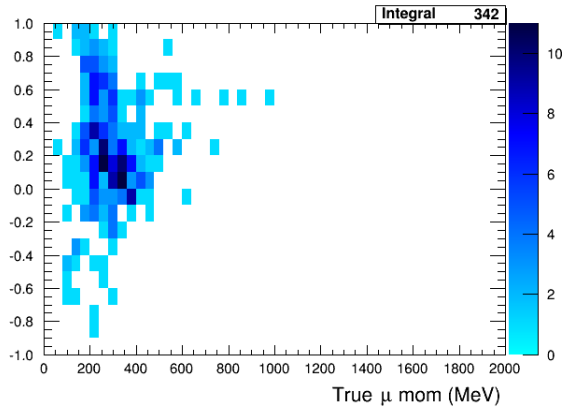

(d) PØD water-out configuration

Figure 3.29: Muon kinematics phase space for CC0π events in selected sample (top) and background control sample (bottom). CC0π events from background control sample are used to constrain the background in selected sample.

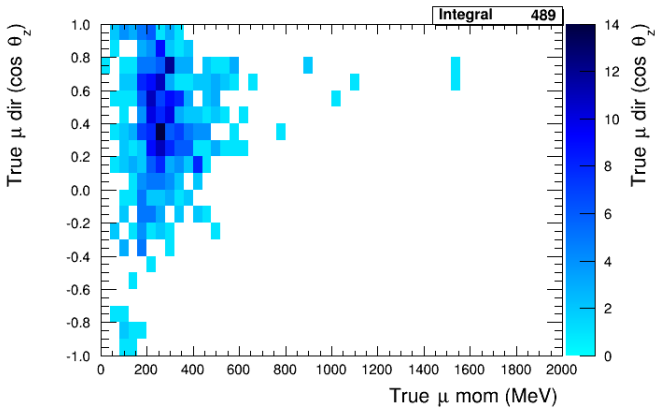

(a) PØD water-in configuration

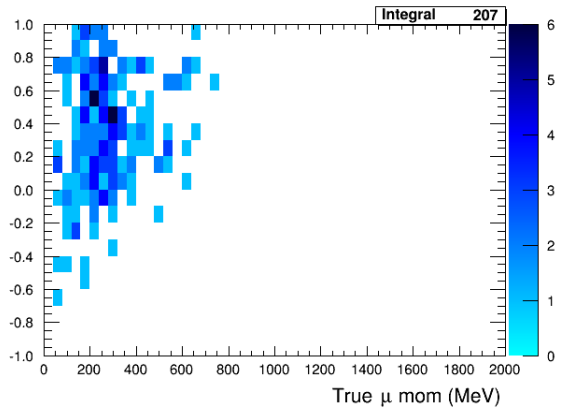

(b) PØD water-out configuration

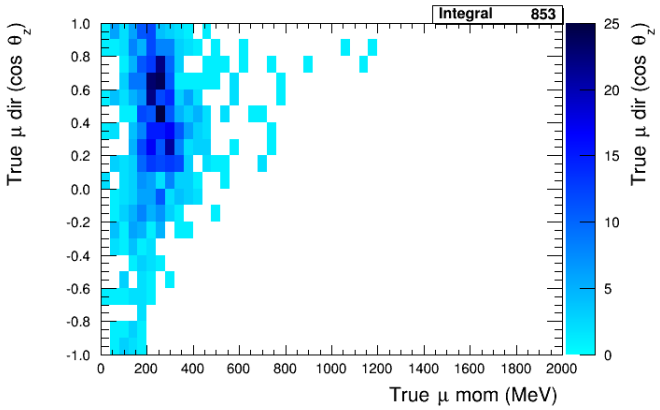

(c) PØD water-in configuration

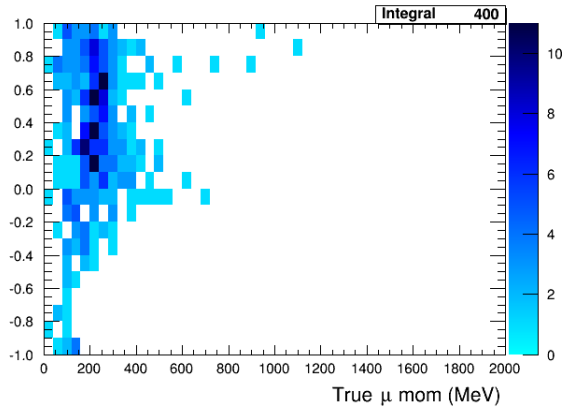

(d) PØD water-out configuration

Figure 3.30: Muon kinematics phase space for CC1$\pi^{\pm}$ events in selected sample (top) and background control sample (bottom).CC1$\pi^{\pm}$ events from background control sample are used to constrain the background in selected sample.

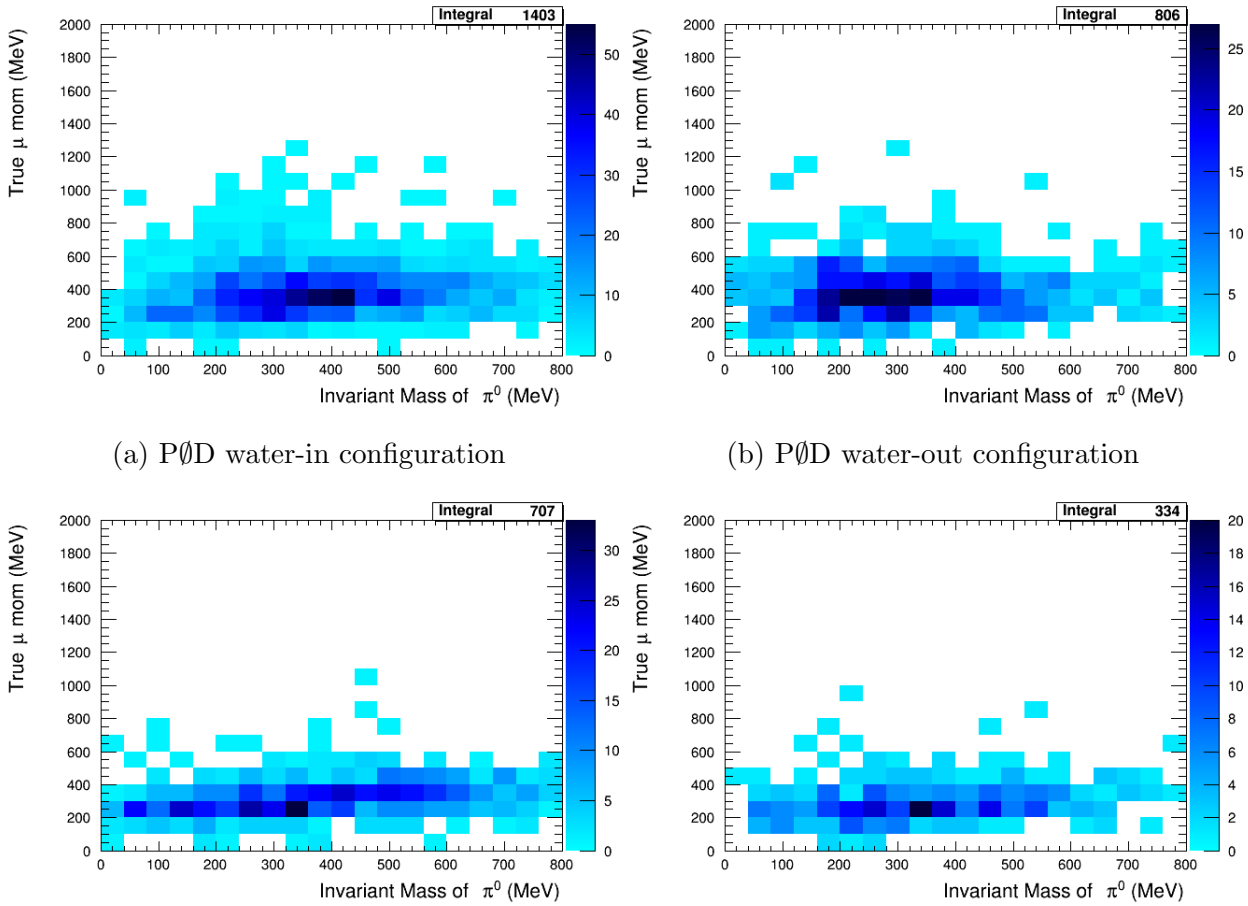

(a) PØD water-in configuration

(b) PØD water-out configuration

(c) PØD water-in configuration

(d) PØD water-out configuration

Figure 3.31: True muon momentum vs. reconstructed π^0 invariant mass for CC0π events in selected sample (top) and background control sample (bottom).

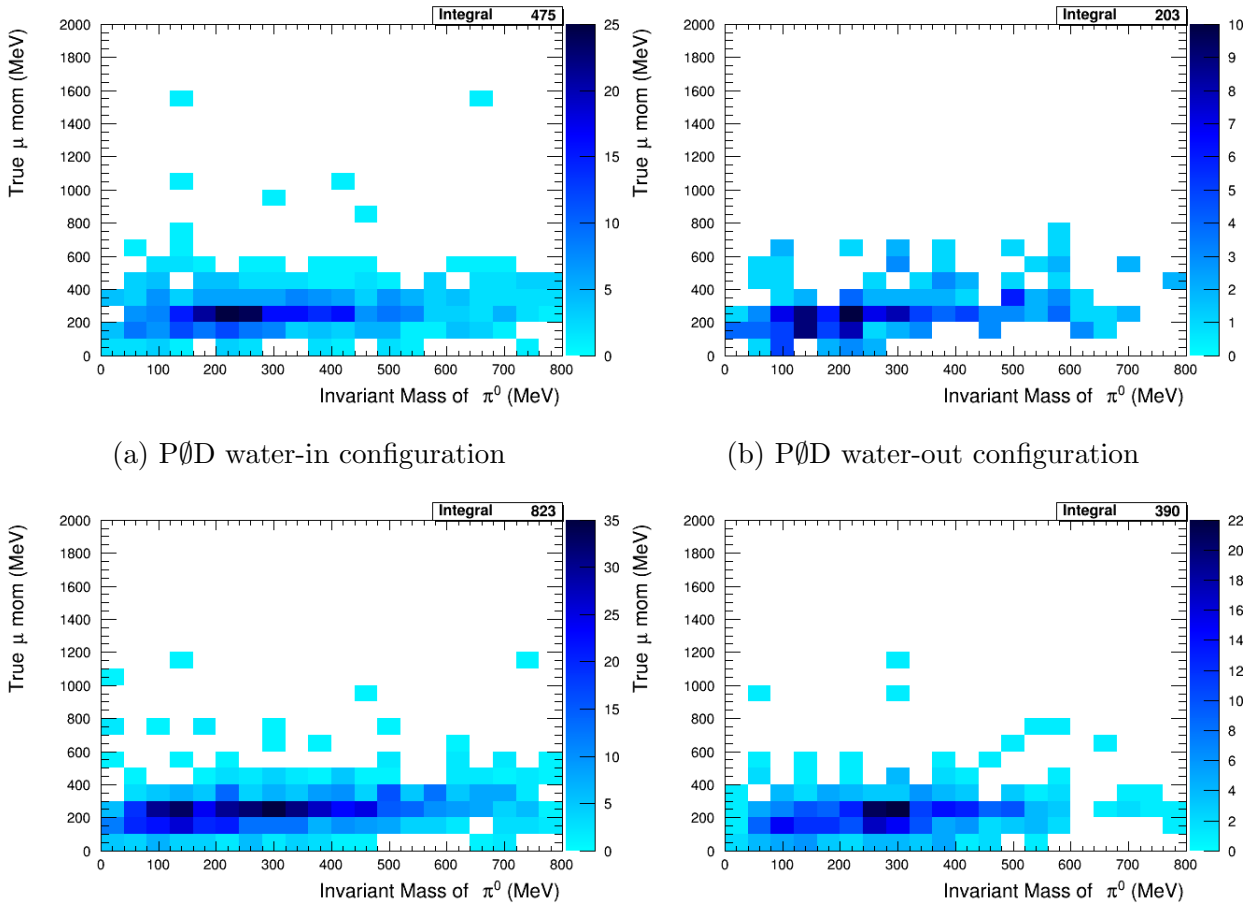

(a) PØD water-in configuration

(b) PØD water-out configuration

(c) PØD water-in configuration

(d) PØD water-out configuration

Figure 3.32: True muon momentum vs. reconstructed π^0 invariant mass for CC1$\pi^{\pm}$ events in selected sample (top) and background control sample (bottom).

Chapter 4

Bayesian Inference for Parameter Estimation

"Today's posterior is tomorrow's prior" - Lindley (1970)

This analysis uses samples from both PØD water-in and water-out configuration. The previous analysis had fit the data for PØD water-in and PØD water-out separately and did a statistical subtraction to obtain the number of signal events on-water. This method treated the systematic uncertainty on the two configurations independently which were added in quadrature for the on-water subtraction. For this iteration, a new fitting method to simultaneous fit both PØD configuration samples was developed. Since this analysis has been limited by detector systematic uncertainties, a bayesian approach using Markov Chain Monte Carlo (MCMC) methods provided a comprehensive way to calculate the error on the signal measurement during the fit by introducing nuisance parameters.

In this chapter, the Bayesian inference techniques and the basics of MCMC will be introduced. The fundamental MCMC algorithm used in this analysis is outlined followed by the mathematical formulation of the likelihood function. For a comprehensive round-up on the mechanics of the fitter, all the fit parameters and the way they alter the likelihood are briefly presented. Details of the physics motivation of each parameter and the priors used for each of them would be described in a separate chapter following this one.

4.1 The Markov Chain Monte Carlo Method

The Monte Carlo methods generate samples from a given probability distribution. In the limit of large numbers, these samples can be used to approximate the properties of the full distribution. A Markov Chain Monte Carlo (MCMC) method utilizes a Markov chain to

sample the parameter space more efficiently than a purely random walk. The trademark Markov chain is a stochastic process that uses the values of the parameters at the current step to propose the next set of values for all the parameters.

Bayesian inference uses Bayes' theorem, Eq. 4.1, to update the probability of an hypothesis as more evidence is presented.

$$P(\theta|x) = \frac{P(x|\theta)P(\theta)}{P(x)} \tag{4.1}$$

where θ is the model parameter and x is the data. The formula is presented for a single model parameter but can straightforwardly be generalized to any number of parameters. The resulting $P(\theta|x)$ distribution is also known as the posterior distribution, often shortened to posterior. Hence, to compute the posterior distribution we require $P(x|\theta)$, which is the likelihood function, the prior $P(\theta)$ and $P(x)$ which is also known as the evidence. The prior distribution encodes all information on the model parameters that we have before we fit it to the current data set. $P(x)$ can be calculated as an integral over all possible values of the parameters i.e.,

$$P(x) = \int_{\Theta} P(x, \theta) d\theta \tag{4.2}$$

This is a non-trivial integral and usually does not have a closed-form solution.

MCMC algorithms sample the posterior distribution without computing the integral in Eq. 4.2. The most basic MCMC algorithm is the Metropolis-Hastings algorithm described in the next section. The process that eliminates the need of calculating Eq. 4.2 is highlighted in the description of the MCMC algorithm.

4.1.1 Metropolis-Hastings Algorithm

This algorithm was first developed by N. Metropolis et. al. in 1953 [74] and the work was extended by W. K. Hastings in 1970 [75].

- Initialize $\theta = \theta_0$
- Propose a new step $\theta' = \theta_0 + \theta_{step}$
- Calculate the likelihood for the new value θ'
- Calculate the acceptance ratio $\alpha = \frac{P(x|\theta')P(\theta')}{P(x|\theta_0)P(\theta_0)}$
- Accept or reject:
  - Generate a uniform random number r on [0,1]
  - If $r \leq \alpha$, accept the new step
  - If $r > \alpha$, reject the new step

The calculation of the acceptance ratio α, eliminates the need to calculate the integral $P(x) = \int_{\Theta} P(x, \theta) d\theta$.

$$\frac{\frac{P(x|\theta')P(\theta')}{P(x)}}{\frac{P(x|\theta_0)P(\theta_0)}{P(x)}} = \frac{P(x|\theta')P(\theta')}{P(x|\theta_0)P(\theta_0)} \tag{4.3}$$

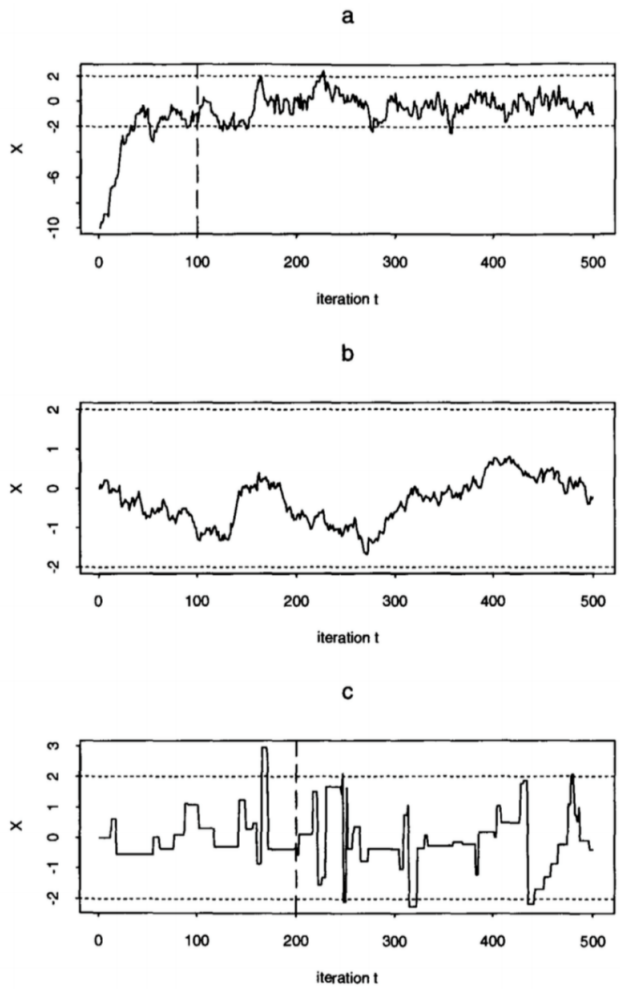

Figure 4.1: The effects of step size in estimating a normal distribution $N(0, 1)$ using 500 steps of MCMC Chain. The top panel shows the optimal step size which quickly moves to a region of high probability and samples the stationary distribution. The middle panel has a small step size which cause too many steps to be accepted and takes a very long time to reach the stationary distribution. The last panel depicts the case of a large step size which fluctuates between the tails of the distribution leading to a poor acceptance rate. The dotted line shows the burn-in value. Figure is adapted from [13].

4.1.2 Adaptive Metropolis-Hastings Algorithm

The fitter used for this analysis uses a slightly modified version of the Metropolis-Hastings algorithm. The principle behind any optimization of MCMC methods is to efficiently sample the phase space of higher likelihood values instead of all possible values of the parameters. It is also important to optimize the step size of the proposal function. A small step size would lead to too many points being accepted and a very long time to completely sample the posterior distribution while a very large step size jumps very often to the tails of the distribution leading to a poor acceptance rate of steps. Figure 4.1 shows the affects of step size on the convergence of MCMC chains. This helps the MCMC chain converge quickly. Knowing the higher likelihood phase space a priori implies that the posterior distribution we started out to calculate is already established.

This predicament is solved in the Adaptive Metropolis-Hastings Algorithm by developing a chain that learns from all the previous accepted steps. Instead of proposing the next step depending on only the current step, it builds a covariance matrix of all the accepted steps and chooses the next step based on this matrix and the acceptance rate of the steps. It increases the step size if too many points were being accepted and decreases it if too few points were accepted. The starting point for the sampling could be very far from the region of high posterior probability. A burn-in value for MCMC chains is defined as the number of steps it takes for the chain to go from the initial conditions to the region of high likelihood. All steps before the burn-in value can be discarded as they are only useful to traverse the sample space to the region of interest. Figure 4.1 also shows the burn-in values for each chain by the dotted line. The middle panel does not reach the burn-in point for 500 iterations as it has a small step size.

4.2 Likelihood

The likelihood function provides a measure of how well a given set of parameters of the model describe the observed data. The best fit parameters maximize the likelihood function. It is easier to work with the log of the likelihood function so that the different contributions to likelihood become additive instead of multiplicative. This aids in taking the derivative required to maximize the function. The log likelihood used for this analysis is given by Eq. 4.4:

$$Log\mathcal{L} = Log(\mathcal{L}_{stat}) + Log(\mathcal{L}_{syst}) + Log(\mathcal{L}_{penalty}) \tag{4.4}$$

$\mathcal{L}_{stat}$ is the standard poisson likelihood, given by Eq. 4.5

$$Log(\mathcal{L}_{stat}) = \sum_{i=1}^{nbins} N^i_{Data} \times Log\frac{N^i_{MC}}{N^i_{Data}} + N^i_{Data} - N^i_{MC} \tag{4.5}$$

N^i_{Data} is fixed and is the number of data events in each bin at the end of event selection. N^i_{MC} varies for each iteration. For each throw of the fit parameters, a new value of N^i_{MC} is calculated in each bin. This value is then used to compute the likelihood by comparing it to N^i_{Data}. The way in which each fit parameter alters N^i_{MC} depends on the type of parameter.

Section 4.2.1 details how each parameter affects N_{MC}. $\mathcal{L}_{stat}$ is calculated for all input samples and to get the total likelihood for each throw of the parameter.

$\mathcal{L}_{syst}$ is given by Eq. 4.6:

$$Log(\mathcal{L}_{syst}) = -\frac{1}{2}V^{\dagger}(Cov)^{-1}V \tag{4.6}$$

V is the vector of all parameters used to vary the N^{i}_{MC} at each step, and Cov is the covariance matrix constraining these parameters to vary in a correlated way and not deviate far away from the priors on these parameters. The priors on the parameters reflect our knowledge of the parameters before fitting them with data. These typically come from fitting these parameters to other data sets or from external experiments. If the parameters take a value far away from the prior, Eq. 4.6 penalizes the likelihood in proportion to the difference from the mean as compared to its standard deviation.

$\mathcal{L}_{penalty}$ is added to the likelihood as a more stringent penalty if the parameters stray away beyond their physically allowed lower or upper bound. It defines the boundaries of the phase space the parameters are allowed to sample.

4.2.1 Fit Parameters

From the Bayesian perspective, there is no difference in the parameters that measure the signal events and the other model or detector parameters. These parameters can be classified into two artificial categories 'parameters of interest' and nuisance parameters. Nuisance parameters are the parameters that must be included as they affect the probability distribution of the parameters of interest in the fit. For instance, in this fit the mass of water in the PØD is not an interesting physics observable but it will directly impact the number of π^0 particles produced on water. In this way, all systematics parameters can be added to the fit as nuisance parameters. By integrating the final posterior distribution over all nuisance parameters, a posterior in just the parameters of interest can be obtained, as given by Eq. 4.7. It is equivalent to projecting the posterior on to a small number of dimensions. This process is known as marginalization.

$$P(\vec{\theta}_{poi}|x) = \frac{\int P(x|\vec{\theta}_{poi}, \vec{\theta}_n)P(\vec{\theta}_{poi}, \vec{\theta}_n)d\vec{\theta}_n}{\int P(x|\vec{\theta})P(\vec{\theta})d\vec{\theta}} \tag{4.7}$$

where poi is the subscript for parameters of interest and n is nuisance. This section lists all the parameters and the how they alter the numbers of events predicted by the Monte Carlo. They are classified into separate sections depending on the part of the Monte Carlo they affect.

Cross Section and FSI Model Parameters

These parameters alter the underlying cross section parameters of the background events. The nominal Monte Carlo has a given set of models to predict the background events. However to make the background subtraction model independent, the cross section models for these events are allowed to vary and are constrained with the data by fitting the background

control sample simulatenously. These parameters only affect the background event and each event is reweighted individually. The weights from all the model parameters are multiplied to get the total weight for each event.

Flux Parameters

The nominal beam flux model predicts the number of incoming neutrino of a particular energy. The T2K beam group provides the parameters and covariances to re-weight the events. These parameters are also applied to the background events only. The events are binned according to their incoming neutrino energy. All the events in a bin are re-weighted by the same weight.

Detector Systematics Parameters

These parameters are used to vary the detector response which might differ for data and Monte Carlo. These parameters are applied individually to all signal and background events. Parameters that are expected to behave differently for signal and background events are explicitly divided into two separate signal and background components to provide the freedom to the fit to move these parameters independently.

Signal Weight Parameters

As the name suggests, these are weight parameters that are applied only to signal events. These parameters are applied bin-by-bin in the π^0 invariant mass of distribution which is being fit. The bins are divided such that a fairly even distribution of statistics exist across all bins. The relevant bins for this analysis span the range of 0-500 MeV. One additional bin for all events with invariant mass > 500 MeV is created to account for all event migrations in and out of the relevant bins but is not used for the final measurement. All bins are listed in Table 4.1.

NBins	Bin boundaries (in MeV)
9	0 - 40 - 80 - 120 - 150 - 190 - 250 - 350 - 500 - 1500

Table 4.1: π^0 invariant mass bins in which the fit is performed.

To obtain the final result in terms of number of signal events that occurred on water separately from all the other signal events, signal weight parameters are divide in two categories - on water and not-water. The Monte Carlo events in PØD water-in configuration are weighted by $c_i^{on-water}$ if the target of their interaction is water or by $c_i^{not-water}$ for all other targets. All signal events of PØD water-out configuration are weighted by $c_i^{not-water}$. This procedure fits the samples from both PØD configurations simulatenously and extracts the number of events on-water intrinsically without the need of a statistical subtraction of the two samples.

$c_i^{on-water}$ are thus the parameters of interest and the rest are nuisance parameters. In all, there are 133 fit parameters, out of which 8 are parameters of interest measuring signal

weight on water. To obtain the final count of number of events on water, nuisance parameters must be marginalized and the signal on-water weights must be multiplied with the nominal number of signal on-water events predicted by the Monte Carlo.

To make this task simpler, the fitter saves the $N^{signal}_{on-water}$, given by Eq. 4.8 at each accepted step.

$$N^{signal}_{on-water} = \sum_{i=1}^{nbins-1} c_i^{on-water} \times N^{signal,nominal}_{i,on-water} \tag{4.8}$$

After the fit, the mean of this distribution gives the total number of on-water signal events and the variance gives the error in measurement, marginalized over all nuisance parameters.

Chapter 5

Systematic Uncertainty

"How will you go about finding that thing the nature of which is totally unknown to you?"
- Rebecca Solnit, A Field Guide to Getting Lost

The list of parameters that will be used to vary the nominal Monte Carlo in the fit with data was provided in Section 4.2.1. Including the systematic effects as nuisance parameters in the fitter accounts for the systematic errors from all the sources in the final result. This makes the error calculation straightforward and the errors do not need to be calculated externally. Simultaneous fitting of both PØD water-in and water-out configurations also makes it simple to keep track of systematic parameters that are correlated between the two PØD configurations and the ones which are not.

This chapter explains the physics motivation behind all parameters and the priors applied on them in the fitter. Section 5.1 details all the cross section model parameters and the processes they impact. It'll be followed by a section on flux parameters. Finally, detector systematic parameters and their priors would be discussed.

5.1 Cross Section & FSI Parameters

The cross section and FSI parameters in the fit are applied only to the background events and are constrained in the selected sample by the background control sample. The purpose of not varying the cross section of signal model is to measure any difference data provides with the default model.

The Neutrino Interaction Working Group (NIWG) of the T2K Experiment is dedicated to collating different theoretical models and test their validity against external data sets from various neutrino experiments. It then recommends a set of parameters and the uncertainty on them that can be used to vary the nominal NEUT models to reflect our best understanding.

This analysis uses the recommendation provided by NIWG on cross section model parameters and their uncertainties for the latest T2K oscillation analysis [14]. It is combined with guidance from NIWG on adapting these model parameters for a cross section analysis. [76].

To calculate the effect of altering the underlying cross section model, NIWG provides a software tool called 'T2K Re-weight'. It provides a re-weighting for each event of the simulation to provide the desired effect of changing the underlying cross section model. This prevents having to reproduce the entire simulation for a tweaked parameter value, which would take a very large computing and time resource. However, using T2K Re-weight for all the model parameters at each step of MCMC would still be very costly in time. To subvert this problem, a 'response function' is produced using T2K Re-weight for each event by tweaking the value of the parameter up and down by three standard deviations or from the lower bound to the upper bound if the parameter has a limited range of validity. A linear spline is used to interpolate between the values at which the weights are calculated. Since loading the response function of each event is still time intensive, a further optimization is achieved by saving the response functions only for the parameters that provide a unique weight for each event because they depend on some underlying interaction or kinematics variable. The normalization weight parameters are same for all events and are multiplied directly to re-weight all the events by the same value. The default T2K Monte Carlo uses SF model and Nieves 2p2h model for CCQE events, as discussed in Section 1.3.1. However, based on results from external data fits [77], events are retuned to change the default model to the Relativistic Fermi Gas (RFG). Additionally, relativistic Random Phase Approximation (Nieves RPA) is also applied as a tuning to include the screening effects of nuclear matter. These alter the fundamental interaction models. Additional parameters added to the fit and the priors applied to them are listed in the following sections. Further details on the function of each parameter and their priors can be found in the T2K Technical Note of NIWG [14].

CCQE Parameters

These parameters change the axial form factor and Pauli blocking for CCQE events. A gaussian distribution with the central value and error listed in Table 5.1 is used as priors for these parameters.

Parameter	Nominal NEUT	Central Value	Error	Lower Bound	Upper Bound
MAQE	1(1.20)	1(1.20)	0.41(0.34)	0.00	10.00
$p_F C$	1(217)	1(217)	0.14(31)	0.92(200)	1.27(275)
$p_F O$	1(225)	1(225)	0.14(31)	0.89(200)	1.22(275)

Table 5.1: Priors on CCQE parameters. Values are normalized with respect to NEUT Nominal. Absolute values are provided in brackets.

2p2h Parameters

Separate and uncorrelated normalization parameters are applied to 2p2h events for ν and $\bar{\nu}$. A scaling for 2p-2h norm is applied to O and scales the weight from carbon to oxygen target. This scaling has 20% uncertainty which is fully correlated between ν and $\bar{\nu}$.

Apart from the normalization uncertainty, separate 2p2h shape parameters are applied for C and O. These parameters control the contribution of different models to the 2p2h interactions. There is 30% correlation between the two shape parameters and they are fully correlated between ν and $\bar{\nu}$. A large error ensures that though the prior is gaussian, it remains relatively flat between the lower and upper bound.

Parameter	Nominal NEUT	Central Value	Error	Lower Bound	Upper Bound
2p-2h shape C	0	0	3	-1.00	1.00
2p-2h shape O	0	0	3	-1.00	1.00

Table 5.2: Priors on 2p2h shape parameters.

RPA Parameters

These are currently applied to CCQE event only. The RPA would affect other channels as well but currently no external fit is available and the contribution from nuclear effects are included in the tuning of the 1 π parameters. The five RPA normalization parameters introduced by NIWG for 2017 oscillation analysis are adapted for the purpose of this analysis.

1π Resonance Parameters

These parameters were fit with external bubble chamber and MiniBooNE data and updated with new central values and errors [14]. These parameters affect both the signal and background channels but are applied selectively to background events.

Parameter	Nominal NEUT	Central Value	Error	Lower Bound	Upper Bound
CA5	1(1.01)	0.95(0.96)	0.15(0.15)	0.00	10.00
MARES	1(0.95)	1.13(1.07)	0.16(0.15)	0.00	10.00
ISO_BKG	1(1.30)	0.74(0.96)	0.31(0.40)	0.00	10.00

Table 5.3: Priors on resonance interaction parameters.

The parameters are applied as gaussian priors with errors mentioned in Table 5.3. The correlation between these parameters is shown in Figure 5.1 below:

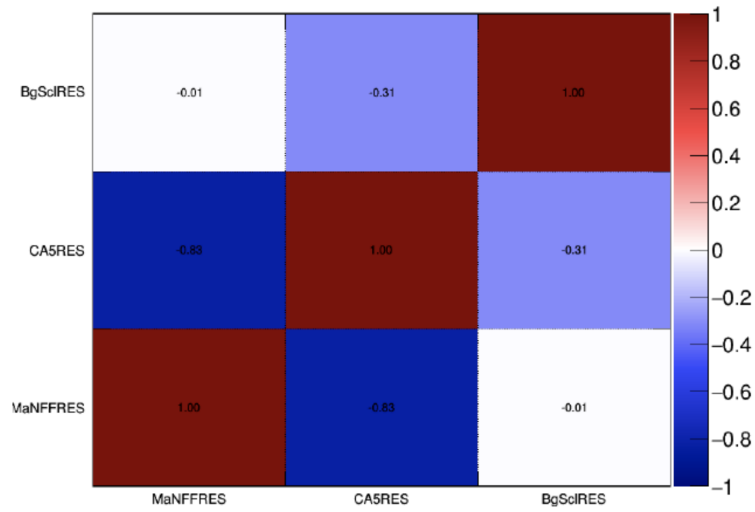

Figure 5.1: Correlation Matrix for Resonance Parameters [14].

1π Coherent Parameters

NEUT uses Rein-Sehgal(RS) model which overestimates the CC coherent cross section. The more recent Berger-Sehgal model is implemented in the next NEUT version which agrees better with external data. Current NEUT version uses a tuning, given in Table 5.4, to re-weight simulated CC coherent events as a function of pion energy.

Pion energy (GeV)	weight
0.00 - 0.25	0.135
0.25 - 0.50	0.4
0.50 - 0.75	0.294
0.75 - 1.00	1.206

Table 5.4: Tuning applied to CC Coherent events as a function of pion energy.

The CC Coherent parameters on C and O are fully correlated with each other.

Parameter	Nominal NEUT	Central Value	Error	Lower Bound	Upper Bound
CC Coherent C(norm)	1.00	1.00	0.30	0.00	10.00
CC Coherent O(norm)	1.00	1.00	0.30	0.00	10.00

Table 5.5: Priors on 1 π coherent parameters.

No re-weighting is applied to NC Coherent interactions as it forms one of the signal channels.

ν_e Parameters

Theoretically motivated uncertainties [78] are applied to ν_e events as a ratio of cross section to ν_μ events to account for the difference in the neutrino flavor. They are implemented separately for ν and $\bar{\nu}$ with a 2% anti-correlation between them.

Parameter	Nominal NEUT	Central Value	Error	Lower Bound	Upper Bound
ν_e/ν_μ	1.00	1.00	0.03	0.00	10.00
$\bar{\nu}_e/\bar{\nu}_\mu$	1.00	1.00	0.03	0.00	10.00

Table 5.6: Priors on ν_e interaction parameters.

Other Parameters

A single CC Other shape uncertainty is applied to all other remaining CC channels which includes deep inelastic scattering. This parameter is applied as an inverse function of incoming neutrino energy (E_ν) with an internal threshold at 0.6 GeV. A gaussian normalization parameter with 30% uncertainty is applied to all remaining NC interaction channels. NC1γ events are multiplied by additional factor of 2.0 from the default NEUT simulation [79].

Parameter	Nominal NEUT	Central Value	Error	Lower Bound	Upper Bound
NC 1 γ	1.00	1.00	1.00	0.00	10.00
CC Other (shape)	0.00	0.00	0.40	-10.0	10.00
NC Other (norm)	1.00	1.00	0.30	0.00	10.00

Table 5.7: Priors on NC1γ, NC Other and CC other interaction parameters.

FSI Parameters

NEUT uses a cascade model to simulate pion interactions. Pion FSI parameters either scale the probability of π interaction with the nuclear medium or scale the charge exchange fraction. T2K re-weight predicts an escape probability for each pion inside the nucleus by re-running the cascade algorithm with different values of the FSI parameters. The ratio of the new varied probability to the nominal value is given as the FSI weight of the event. These six parameters give the probability of inelastic scattering, absorption or production of pion or charge exchange of pions when traveling through the nuclear medium.

Parameter	Nominal NEUT	Central Value	Error	Lower Bound	Upper Bound
FSI Inelastic LO (FEFQE)	0.00	0.00	0.41	-10.00	10.00
FSI Inelastic HI (FEFQEH)	0.00	0.00	0.34	-10.00	10.00
FSI PI PROD (FEFINEL)	0.00	0.00	0.50	-10.00	10.00
FSI PI ABS (FEFABS)	0.00	0.00	0.41	-10.00	10.00
FSI CHARGE EX LO (FEFCX)	0.00	0.00	0.57	-10.00	10.00
FSI CHARGE EX HI (FEFCXH)	0.00	0.00	0.28	-10.00	10.00

Table 5.8: Priors on pion final state interaction parameters.

The correlation between above parameters is shown in Figure 5.2 below:

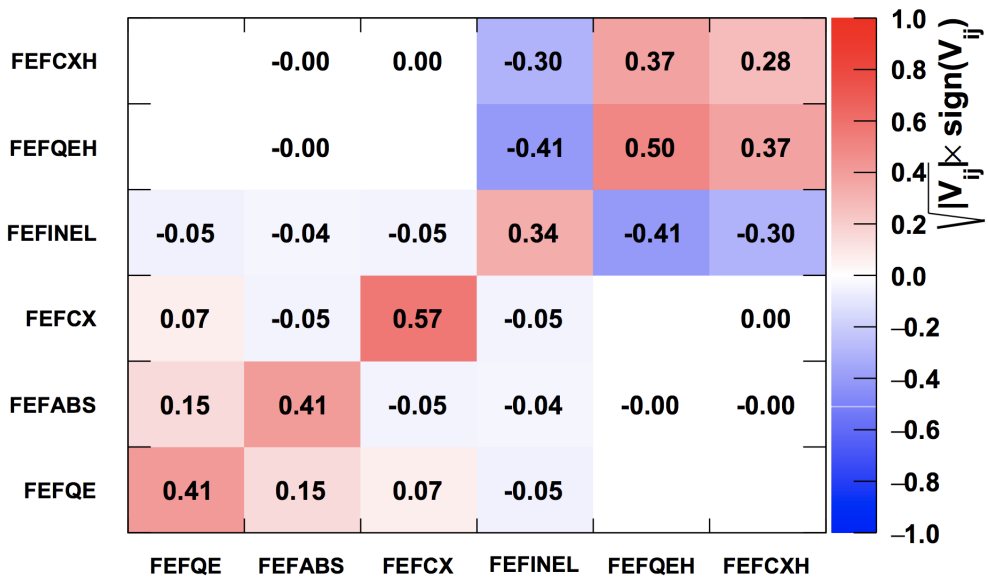

Figure 5.2: Correlation Matrix for FSI Parameters [14].

5.2 Flux Parameters

Flux re-weighting parameters are provided by the T2K beam group. The fit is done without varying the neutrino flux on signal events to measure the number of NC1π^0 events for the the "real" flux of T2K beam. However, it is applied to the background events so as to provide enough freedom for them to vary and fit the background control sample which is then used to estimate the background in the signal sample. To make a cross section measurement, the event rate has to be averaged over the integrated neutrino flux.

The events are binned according to the flavor of incoming neutrino and its true energy, given in Table 5.9. Each bin has one fit parameter and all the events in that bin are re-

weighted by the value of the parameter. There are a total of 25 parameters and their priors are provided in Table 5.10 and correlation between them is shown in Figure 5.3.

ν flavor	NBins	Bin boundaries (in GeV)
ν_μ	11	0.0 - 0.4 - 0.5 - 0.6 - 0.7 - 1.0 - 1.5 - 2.5 - 3.5 - 5.0 - 7.0 - 30.0
$\bar{\nu}_\mu$	5	0.0 - 0.7 - 1.0 - 1.5 - 2.5 - 30.0
ν_e	7	0.0 - 0.5 - 0.7 - 0.8 - 1.5 - 2.5 - 4.0 - 30.0
$\bar{\nu}_e$	2	0.0 - 2.5 - 30.0

Table 5.9: Incoming neutrino energy bins for flux reweighting

Parameter	Nominal	Central Value	Error	Lower Bound	Upper Bound
ν_μ Bin 0	1.00	1.00	0.101	0.00	10.00
ν_μ Bin 1	1.00	1.00	0.099	0.00	10.00
ν_μ Bin 2	1.00	1.00	0.092	0.00	10.00
ν_μ Bin 3	1.00	1.00	0.085	0.00	10.00
ν_μ Bin 4	1.00	1.00	0.105	0.00	10.00
ν_μ Bin 5	1.00	1.00	0.104	0.00	10.00
ν_μ Bin 6	1.00	1.00	0.074	0.00	10.00
ν_μ Bin 7	1.00	1.00	0.069	0.00	10.00
ν_μ Bin 8	1.00	1.00	0.082	0.00	10.00
ν_μ Bin 9	1.00	1.00	0.097	0.00	10.00
ν_μ Bin 10	1.00	1.00	0.115	0.00	10.00
$\bar{\nu}_\mu$ Bin 0	1.00	1.00	0.104	0.00	10.00
$\bar{\nu}_\mu$ Bin 1	1.00	1.00	0.084	0.00	10.00
$\bar{\nu}_\mu$ Bin 2	1.00	1.00	0.081	0.00	10.00
$\bar{\nu}_\mu$ Bin 3	1.00	1.00	0.085	0.00	10.00
$\bar{\nu}_\mu$ Bin 4	1.00	1.00	0.088	0.00	10.00
ν_e Bin 0	1.00	1.00	0.091	0.00	10.00
ν_e Bin 1	1.00	1.00	0.090	0.00	10.00
ν_e Bin 2	1.00	1.00	0.085	0.00	10.00
ν_e Bin 3	1.00	1.00	0.080	0.00	10.00
ν_e Bin 4	1.00	1.00	0.080	0.00	10.00
ν_e Bin 5	1.00	1.00	0.081	0.00	10.00
ν_e Bin 6	1.00	1.00	0.096	0.00	10.00
$\bar{\nu}_e$ Bin 0	1.00	1.00	0.072	0.00	10.00
$\bar{\nu}_e$ Bin 1	1.00	1.00	0.143	0.00	10.00

Table 5.10: Priors on T2K flux parameters.

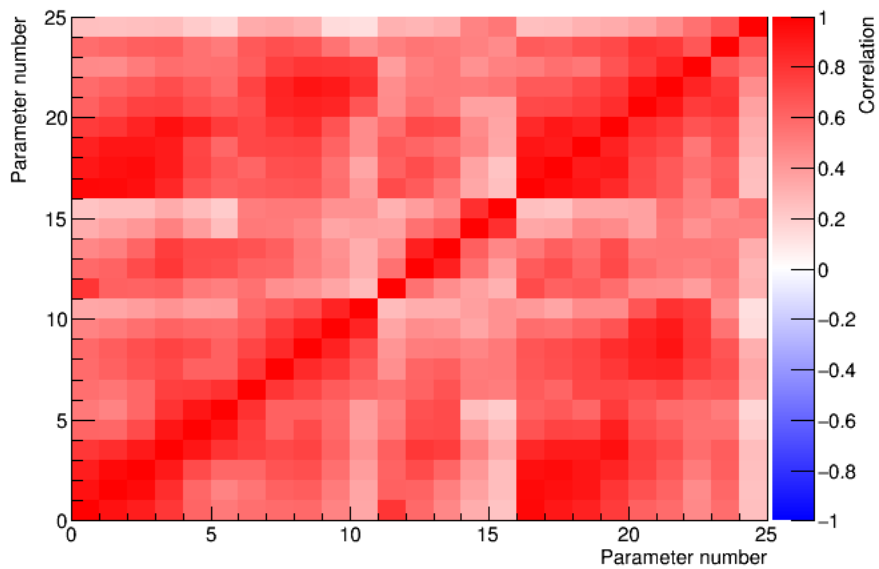

Figure 5.3: Correlation Matrix for Flux Parameters

5.3 Detector Systematics Parameters

Detector systematics parameters are introduced to account for the disparity in the real, physical detector versus its simulation and the differences which lead to a bias in reconstruction between data and Monte Carlo events. Depending on the feature of the detector the parameters quantify, they are applied separately to only signal, only background or all events. The correlations for these parameters between PØD water-in and water-out configurations is also considered individually and discussed in each section. The parameters that are discussed in this section are: PØD mass, data and Monte Carlo differences in the Charge Ratio, Particle ID and Shower Separation Distance selection cuts described in Section 3.1, efficiency of tagging muon decay and the rate of false muon decay tagging by the reconstruction.

This chapter will conclude with a discussion on vertex position resolution and the impact of difference in energy scale on the reconstruction efficiency of π^0 particle. These two categories are not included in the fit as their effects on the signal distribution could not be suitably parametrized. However, the estimate of the systematic uncertainty contribution from these variables are small and can be directly applied to the final fit result.

PØD Mass Uncertainty

The difference in the as-built mass of PØD and the simulation was extensively measured during the construction of the detector and documented in [71]. Most of the mass difference originates from the dead material in water target (such as sensors) which were not modeled in the simulation. Between T2K Run 1 and Run 2, the water depth sensor system was completely replaced, so Run 1 is treated separately from the other Runs. Table 5.11 [12] provides the percentage difference between the simulated and the as-built measurements.

These values form the prior for the mass parameters in the fit. Two separate corrections are applied to the Monte Carlo events depending on if the true interaction vertex is on-water or not-on-water. As the mass difference for the not-water part of the detector is completely correlated between PØD water-in and water-out configuration, the same mass correction is applied to events that occur not-on-water in PØD water-in and events in PØD water-out sample. Each event is simply re-weighted by the value of the relevant parameter according to its target material and Run number.

Run Period	On-Water (%)	Not-On-Water (%)
Run 1	98.9 ± 0.8	102.6 ± 1.0
Run 2+	98.9 ± 0.8	103.1 ± 1.0

Table 5.11: Priors on PØD mass systematics parameters taken from [12]

Systematics from cut on charge in shower particles

The cut on charge deposited by shower particles is described in Section 3.1. The cut is placed on the ratio of the charge deposited by the two shower particles to the total charge in the event. To estimate the difference in data and Monte Carlo behavior, the charge ratio of simulated events is smeared by a scale parameter:

$$(charge\ ratio)' = (1 - scale) \times charge\ ratio \tag{5.1}$$

Four separate systematic parameters to fit the signal and background independently for PØD water-in and PØD water-out configurations are added to the fitter. To obtain a prior on these four parameters, a fit is performed on the distribution of charge ratio for a control sample. This control sample is obtained by selecting events passing all selection cut but failing the Particle ID cut for both PØD water-in and water-out configuration, shown in Figure 5.4.

The MCMC fitter described in chapter 4 is pared down and simplified for this control sample fit. The priors on the parameters for this control sample fit are centered at a nominal value of zero, and allowed to float between $[0, 1]$. The posterior of the parameters from this fit are listed in Table 5.12 which are used as the prior for the main analysis fit. The anti-correlations between signal and background parameters are captured by the fitter and shown in Figure 5.5.

Index	Parameter	Nominal	Central Value	Error	Lower Bound	Upper Bound
1	Signal Scale Water-In	0.00	0.022	0.015	0.00	1.00
2	Background Scale Water-In	0.00	0.005	0.004	0.00	1.00
3	Signal Scale Water-Out	0.00	0.032	0.015	0.00	1.00
4	Background Scale Water-Out	0.00	0.005	0.004	0.00	1.00

Table 5.12: Priors on charge ratio scale parameters for the analysis fit.

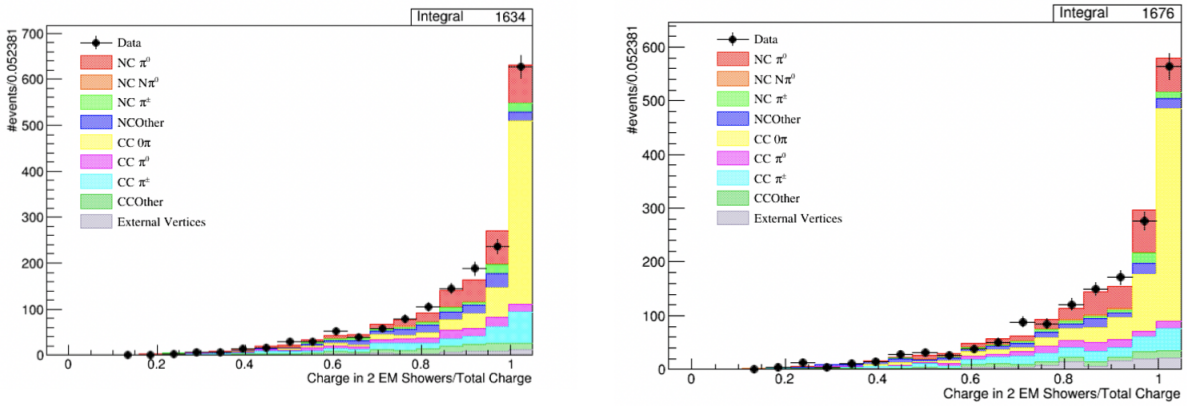

(a)
PØD water-in configuration

(b)
PØD water-out configuration

Figure 5.4: Distribution of fraction of charge in two highest momentum shower particles from the total deposited charge for events that pass all cuts but fail the particle ID cut. This is used as a control sample to obtain priors on the systematics parameters for the cut on charge in shower particles.

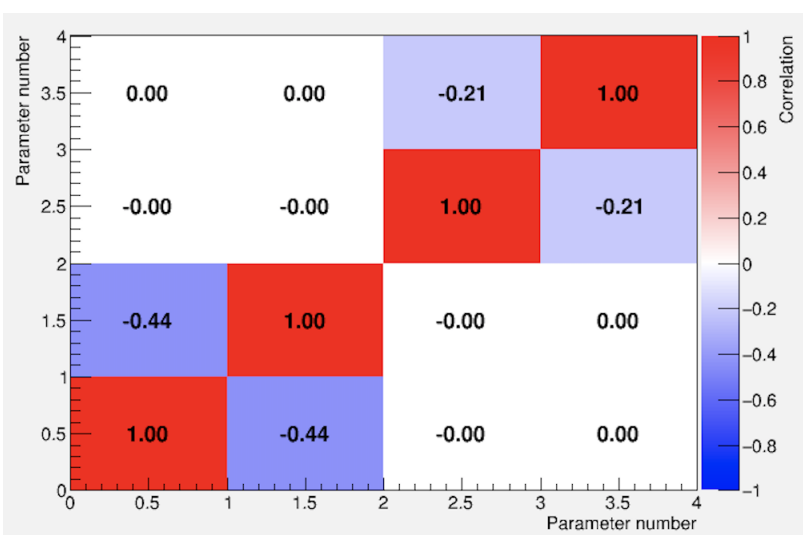

Figure 5.5: Correlation matrix for charge in shower systematics parameters

Systematics from Cut on Particle ID Weight

The process of assigning weights to different PIDs for an event was described in Section 2.4.1. The cut is placed on the difference of kEM PID weight and kShower PID weight. The underlying parameters used to assign these weights are first charge asymmetry and middle charge asymmetry of clusters as described in Section 2.4.1. To estimate the systematics from this cut, the discrepancy in data and Monte Carlo behavior for these distributions should be measured and propagated to the measurement of number of π^0 events. As the lookup table which assigns the particle identification weight is constructed separately for a reconstructed shower particle with 3, 4 or 5 clusters, they are fitted individually. Since the amount of charge deposited by the shower particles in different clusters differs between the two detector configuration, separate parameters are added in the fit for the PØD water-in and water-out samples.

The charge asymmetry of simulated events are smeared by a shift and a scale parameter, given by Eq. 5.2, as these distributions are gaussian-like.

$$Q'_{asymmetry} = scale \times Q_{asymmetry} + shift \tag{5.2}$$

As the background events in the sample are particles that are mis-reconstructed as showers, the charge asymmetry distribution should move in the opposite manner for the signal and background events. Thus, the signal and the background events are allowed to move independently by adding separate parameters for each of them. This gives a total of four parameters (Scale-Signal , Shift-Signal, Scale-Background, Shift-Background) for each distribution. There are three separate cluster categories for two charge asymmetry variables and two PØD configurations totaling to 12 distributions. Thus the fit has a total of 48 parameters to account for the systematics due to cut on PID weight.

Initially, a control sample was constructed to obtain a prior on these parameters by inverting the charge in shower particles cut and not applying any cut on particle ID weight, π^0 direction or shower separation distance. As an example two distributions from this control sample are shown in Figure 5.6.

While the formalism is theoretically rigorous, it produces practical concerns for the fit. A fit using MCMC fitter is performed and as seen from Figure 5.7, the four parameters that control the fit behavior have a high correlation. The two signal and the two background parameters are correlated among themselves while being highly anti-correlated from each other. The MCMC sampling using Adaptive Metropolis Hastings algorithm loses its efficiency if the parameter phase space has high correlations. Ideally, these parameters could be recombined or re-parameterized to form uncorrelated or weakly correlated combinations but that will involve further investigations discussed in Chapter 7. In the interim, to mitigate this issue for the final analysis fit, the errors on these priors are inflated and their correlations are dropped. From the survey of fit results of the control sample discussed above, a conservative value of 50% error on scale and 5% for the shift was chosen, listed in Table 5.13.

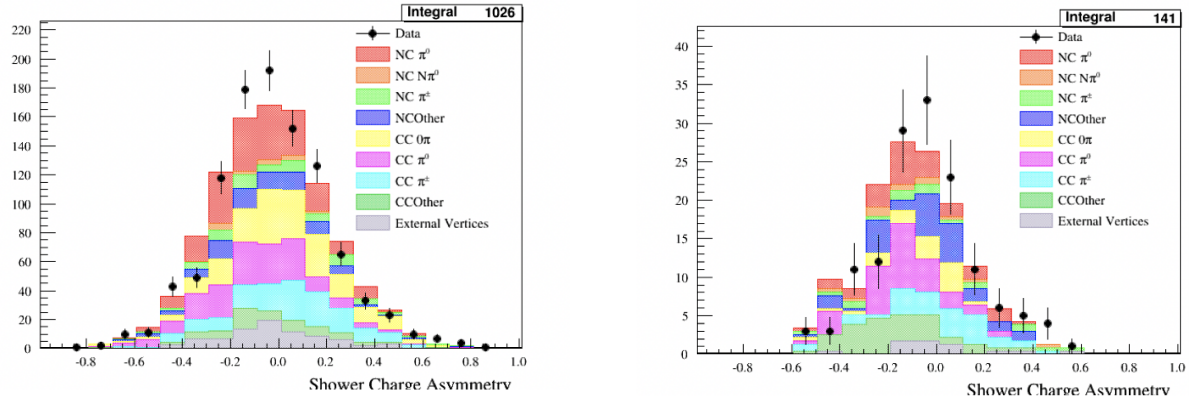

(a) Cluster = 3 (b) Cluster = 4

Figure 5.6: First charge asymmetry distribution for events failing the the charge in shower particles cut and not applying any cut on particle ID weight, π^0 direction or shower separation distance for PØD water-in configuration.

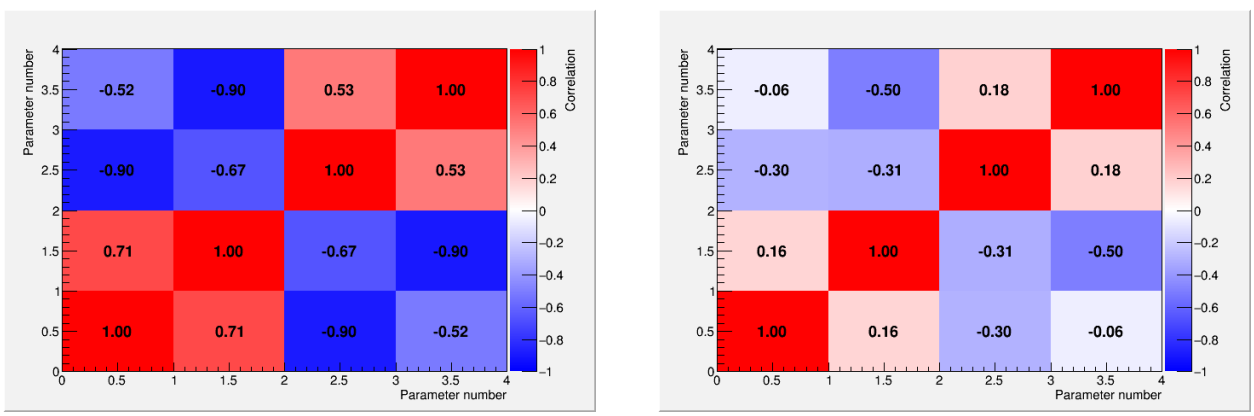

(a) Cluster = 3 (b) Cluster = 4

Figure 5.7: Correlation Matrix obtained from the control sample fit of first charge asymmetry parameters in PØD water-in configuration. Parameter numbers correspond to the index in Table 5.13.

Index	Parameter	Nominal Value	Fit Central Value	Error	Lower Bound	Upper Bound
1	Scale-Signal	1.0	1.0	0.5	0	10.0
2	Shift-Signal	0.0	0.0	0.05	-1.0	1.0
3	Scale-Bkg	1.0	1.0	0.5	0.0	10.0
4	Shift-Bkg	0.0	0.0	0.05	-1.0	1.0

Table 5.13: Priors on the charge asymmetry parameters for PID systematics in the analysis fit. 12 sets of parameters listed in this table are used to account for three separate cluster categories, two charge asymmetry variables and two PØD configurations

By using these parameters as nuisance parameters in the final fit and then marginalizing over them, the error on these parameters is converted to the error on the number of signal events.

Shower Separation Scale

The systematics contributed by any difference in shower separation distance between data and Monte Carlo are measured directly in the final fit. As mentioned in Section 3.1, shower separation distance cut is used to divide the sample in two halves. The events that fail this cut are store as a separate sample, tagged by an additional 'close' to describe the closeness of the two candidate shower particles.

The shower separation distance of Monte Carlo is smeared by a scale parameter as shown in Eq. 5.3 As before, signal and background events and the two PØD configurations are treated independently.

$$d' = scale \times d \tag{5.3}$$

$$d : \text{Shower separation distance}$$

This allows the freedom to Monte Carlo events to move between the two samples divided by the shower separation cut. If the smearing increases the distance such that the value is larger than the cut, the events move from the 'close' sample to the 'separated' selected sample and vice versa. We apply very loose priors on these four parameters which are constrained by fitting the 'close' and 'separated' samples simultaneously during the final fit.

Parameter	Nominal	Central Value	Error	Lower Bound	Upper Bound
Signal Scale Water-In	1.00	1.00	1.00	0.00	10.00
Background Scale Water-In	1.00	1.00	1.20	0.00	10.00
Signal Scale Water-Out	1.00	1.00	1.00	0.00	10.00
Background Scale Water-Out	1.00	1.00	1.00	0.00	10.00

Table 5.14: Priors on shower separation scale parameters for the analysis fit.

Muon Decay Tag: Efficiency and Fake Rate

Events in the background control sample have at least one tagged muon decay cluster while the selected sample have none. This implies that all neutral current events in the background control sample have a fake muon decay tag. Similarly, muon decay tag was missed by the reconstruction for all charged current events present in the selected sample. This systematic measures any difference between data and Monte Carlo in tagging muon decay clusters. It was calculated using a sample of stopping muons by the previous analysis [12]. The difference in Monte Carlo to data in fake rate of tagging muon decay is 1.06 ± 0.5 % for PØD water-in and -1.24 ± 0.7 % for PØD water-out. The efficiency of tagging muon decay clusters is given in Table 5.15.

Parameter	Monte Carlo (%)	Data (%)	MC -Data (%)
Efficiency Water-In	45.6 ± 0.5	44.1 ± 0.5	1.5 ± 0.7
Efficiency Water-Out	43.9 ± 0.6	46.2 ± 0.6	-2.3 ± 0.8

Table 5.15: Efficiency of muon decay reconstruction measured using a sample of stopping muons [12].

To propagate the effect of this systematic to the final result, four parameters were added to the fit using the above listed measurements as priors on them, shown in Table 5.16. No correlations were added between the two PØD configurations. These parameters move events between the selected sample and the background control sample, providing a normalization constraints on both samples.

Parameter	Nominal	Central Value	Error	Lower Bound	Upper Bound
μ decay fake rate Water-In	0.00	0.011	0.005	-1.00	1.00
μ decay efficiency Water-In	0.00	0.015	0.007	-1.00	1.00
μ decay fake rate Water-Out	0.00	-0.012	0.007	-1.00	1.00
μ decay efficiency Water-Out	0.00	-0.023	0.008	-1.00	1.00

Table 5.16: Priors on muon decay efficiency and fake rate parameters for the PØD water-in and water-out samples.

It is important to note that the implementation of these parameters to modify Monte Carlo events is not straightforward. To illustrate, consider an example of one throw of muon decay efficiency water-in parameter. For this throw, assume that the value of this parameter is 0.0145. This suggests that the efficiency to detect muon decay cluster in Monte Carlo is 1.45% more than data, implying more charged current events were tagged correctly for Monte Carlo and hence are present in the background control sample. Hence, 1.45% of total charged current events in Monte Carlo should be moved from background control sample to selected sample. Instead of randomly choosing certain events to move between samples, all charged current events in selected signal are re-weighted to increase the total normalization

by the required amount. At the same time, the charged current events in background control sample are re-weighted to decrease the total normalization by the same amount, such that the total charged current events between the two sample remains constant.

Fiducial Volume systematics

The position of the vertex is used to cut out events which lie outside the PØD fiducial volume. The shower vertex finding algorithm of PØD reconstruction first finds the direction of each of the shower particle in 2D X-Z and Y-Z PØD planes. It combines the 2D projection to form a 3D direction for each shower particle with some error. The vertex position is calculated by optimizing for an objective function which measures the likelihood that the directions of all shower particles on being projected back in space meet at the same point. It is possible to do this because the lifetime of a π^0 particle is very short so the distance between the interaction vertex and π^0 decay is negligible.

The aim of this systematic is to measure any difference in the reconstruction of vertex position between data and Monte Carlo, and how this difference changes the total number of events inside the fiducial volume. The previous PØD analyses for showering events have used the difference between true and reconstructed vertex position in Monte Carlo to calculate this systematics. This difference gives us the vertex resolution of the detector. The resolution of the signal events, as measured in the previous analysis [12] is given in Table 5.17.

	$< x >$ (cm)	σ_x (cm)	$< y >$ (cm)	σ_y (cm)	$< z >$ (cm)	σ_z (cm)
Water-In	-0.06	5.52	0.06	6.06	1.67	8.65
Water-Out	0.08	6.67	0.20	7.95	1.72	11.21

Table 5.17: NC1π^0 vertex resolution in PØD [12].

In the absence of a control sample with data events, this is currently the only estimator available to calculate this systematic. A straightforward approach would be to use these errors in the resolution for each dimension, to smear the position of the Monte Carlo events and then use the new position to determine if it falls within the fiducial volume.

However, the error in the reconstruction of vertex position is dependent on the angle between the two decay photons of π^0 particle while the numbers in Table 5.17 give the average error in the reconstructed position across all signal events. For instance, Figure 5.8 depicts that if the angle between the two shower particles is narrow, the uncertainty in it's vertex reconstruction is larger as compared to for a wider angle.

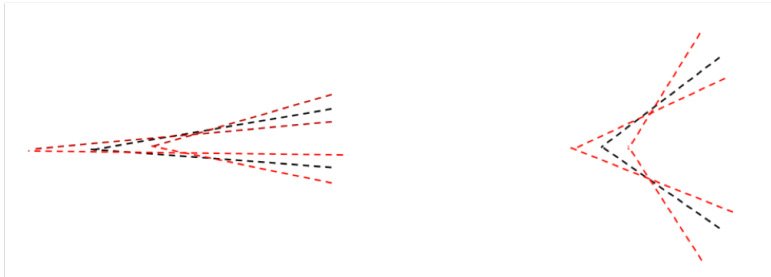

Figure 5.8: Effect of opening angle on Vertex Resolution

To incorporate this additional information, a procedure to estimate the impact of this systematics as outlined below. An uncertainty is assigned to the measurement of σ_x, σ_y and σ_z in Table 5.17. This uncertainty is denoted by $\Delta(\sigma_x)$, $\Delta(\sigma_y)$ and $\Delta(\sigma_z)$. For instance, $\Delta(\sigma_x) = 5$ cm for water-in sample would imply that the error on the x position can vary between 0.52 cm to 10.52 cm. A study was done for the values of $\Delta(\sigma_x) = \Delta(\sigma_y) = \Delta(\sigma_z) =$ 2, 5 and 10 cm. Recall, the dimensions of the PØD are 210 cm (x) $\times$ 224 cm(y) $\times$ 240 cm(z). These values were chosen to understand the effects of a reasonable range of error on the computation of standard deviation in the Monte Carlo resolution. We sample the distribution 10,000 times and in each throw we get a particular value of σ_x, σ_y and σ_z. For each event, the number of sigmas (nsigma) the reconstructed position varies from the true position, in the nominal Monte Carlo, is used as the metric to calculate the new position. The new position of the vertex is obtained by multiplying the value of the sigma from the gaussian throw by its nsigma in nominal Monte Carlo. Once a new position is calculated for the vertex, if it falls within the fiducial volume it is counted towards the total number of events inside the fiducial volume. This is repeated for 10,000 throws. The results of this study is shown in Figure 5.9 and 5.10. The nominal number of signal events with a reconstructed vertex in the fiducial volume for the sample used in this study is 1363 for the PØD water-in and 766 for the PØD water-out configuration.

Even for the largest variation of $\Delta(\sigma_{x/y/z}) = 10$ cm, a conservative estimate of the systematic error on the number of signal events can be computed by adding the difference in mean values to the rms. This gives an error of ~ 5 events for PØD water-in and ~ 4 events for PØD water-out. Thus the systematic error contributed by the vertex resolution on the number of signal events is $< 1\%$ for both PØD water-in and PØD water-out configurations.

Energy scale and π^0 reconstruction efficiency

The relationship between deposited charge in photo-electric unit or (PEU) in the detector to the true energy of the particle (MeV) is given by energy scale. This was studied in detail using simulated samples of photons for different PØD configurations in the previous analysis [12]. These measurements are used to convert the deposited charge from reconstructed hits back to energy of the particle for both data and Monte Carlo events. To estimate if the energy scale of the detector behaves differently for data and Monte Carlo, the previous analysis implemented two energy scale parameters in the fit, one each for PØD water-in and water-out configuration. The fitted values of these parameters is reported as $89.5 \pm 3.4\%$ for PØDwater-in configuration and $96.7 \pm 0.6\%$ for PØD water-out. However, it should be noted

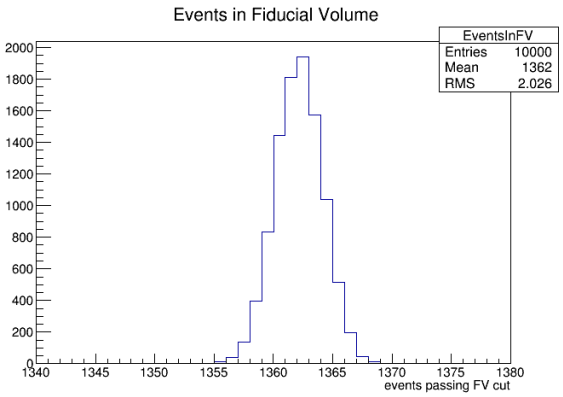

(a) $\Delta(\sigma_x) = \Delta(\sigma_y) = \Delta(\sigma_z) = 2$ cm

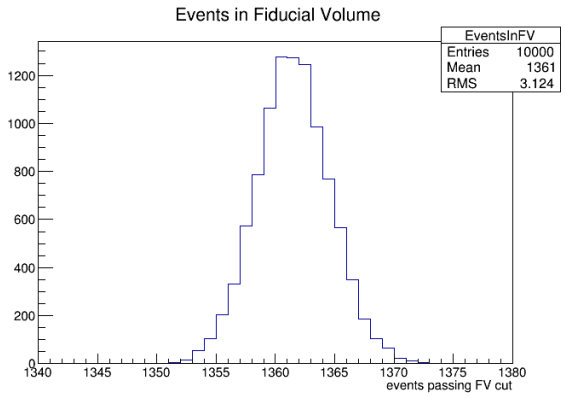

(b) $\Delta(\sigma_x) = \Delta(\sigma_y) = \Delta(\sigma_z) = 5$ cm

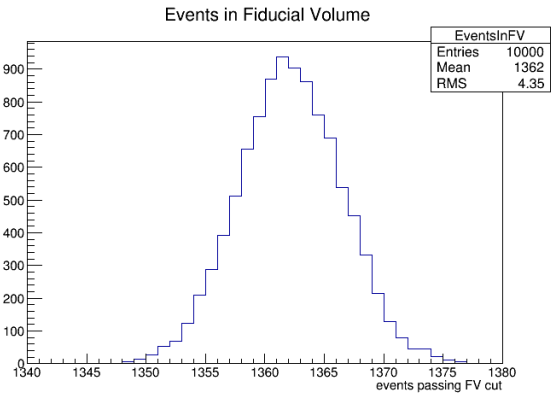

(c) $\Delta(\sigma_x) = \Delta(\sigma_y) = \Delta(\sigma_z) = 10$ cm

Figure 5.9: Distribution of number of events in PØD fiducial volume for 10,000 throws of $\Delta(\sigma_{x/y/z})$ for PØD water-in configuration. Nominal number of events for this Monte Carlo sample is 1363.

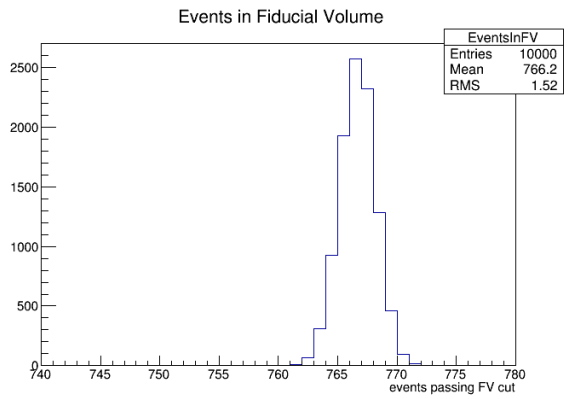

(a) $\Delta(\sigma_x) = \Delta(\sigma_y) = \Delta(\sigma_z) = 2$ cm

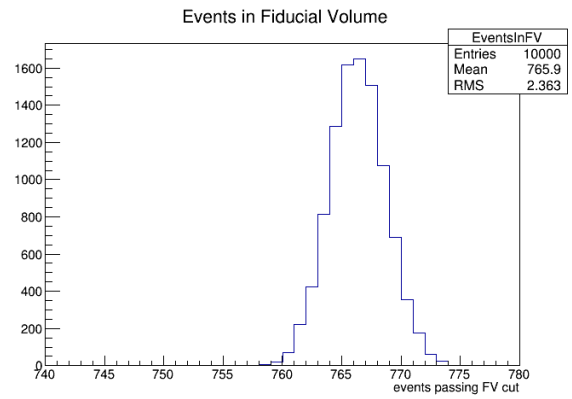

(b) $\Delta(\sigma_x) = \Delta(\sigma_y) = \Delta(\sigma_z) = 5$ cm

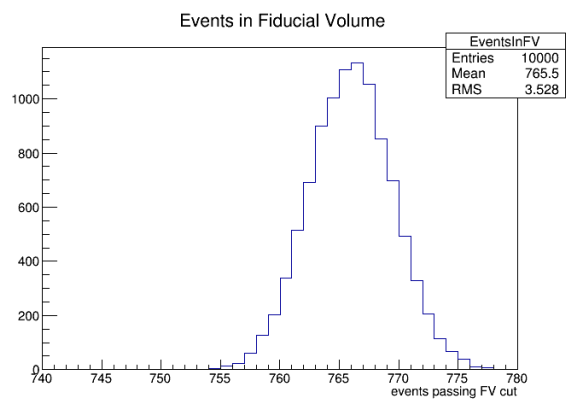

(c) $\Delta(\sigma_x) = \Delta(\sigma_y) = \Delta(\sigma_z) = 10$ cm

Figure 5.10: Distribution of number of events in PØD fiducial volume for 10,000 throws of $\Delta(\sigma_{x/y/z})$ for PØD water-out configuration. Nominal number of events for this Monte Carlo sample is 766.

that the energy scale parameters were the only parameters that modified the shape of the signal in this measurement, possibly folding in other detector shape systematics with it. In the present analysis, there are 18 separate signal weight parameters to modify signal shape. While this gives all the possible freedom required to vary and fit the shape of the signal, even this approach folds in any shape differences due to energy scale with all other detector systematics.

Nonetheless, an estimate of the energy scale parameter can be obtained by measuring the position of the π^0 invariant mass peak. Any shift in the π^0 invariant mass peak between data and Monte Carlo can be attributed to energy scale differences. Using a simple gaussian to fit data and Monte Carlo selected signal samples, the mean and standard deviation of the π^0 mass distribution are calculated, listed in Table 5.18 and 5.19.

Sample	Mean (MeV)	Δ(Mean) (MeV)	Std. Dev (MeV)	Δ(Std. Dev) (MeV)
Monte Carlo	144.41	3.59	67.44	3.39
Data	148.68	9.08	88.24	9.60

Table 5.18: A Gaussian fit to data and Monte Carlo selected signal samples for PØD water-in configuration. The difference in means can be used as an approximation of energy scale difference between data and Monte Carlo.

Sample	Mean (MeV)	Δ(Mean) (MeV)	Std. Dev (MeV)	Δ(Std. Dev) (MeV)
Monte Carlo	141.63	5.55	77.06	6.32
Data	148.36	8.86	90.89	1.13

Table 5.19: A Gaussian fit to data and Monte Carlo selected signal samples for PØD water-out configuration.The difference in means can be used as an approximation of energy scale difference between data and Monte Carlo.

This gives a difference in the mean of 4.27 ± 9.76 MeV for PØD water-in and 6.73 ± 10.45 MeV for PØD water-out. This can be used as a fair approximation of energy scale differences.

While any comparative shift between data and Monte Carlo would naturally be taken into consideration by the signal weight parameters in the fit, the energy scale differences can still impact the measurement due to the dependence of the efficiency on the true π^0 momentum. As shown in Figures 3.14 and 3.15, if the energy scale of the Monte Carlo shifts the momentum up, the efficiency of detecting the event also changes.

A natural place to calculate this systematics would emerge in the next iteration of this analysis, discussed in Chapter 7, as that analysis is likely to implement the bin-by-bin efficiency correction in true π^0 momentum phase space for model comparisons. For the purpose of this analysis, a rough approximation can be made by re-weighting the Monte Carlo events by the ratio of their new efficiency when shifted by the energy scale, to the original efficiency,

shown in Figures 3.14 and 3.15. Since this is just an approximation, this calculation was done for just three different values - the difference in mean and the $\pm 1\sigma$ values of energy scale, for both PØD water-in and water-out configuration. Using this method, an error of 0.5% on the PØD water-in and 1% on PØD water-out configuration was obtained.

Chapter 6

Results

"Forty-two!" yelled Loonquawl. "Is that all you've got to show for seven and a half million years' work?" - Douglas Adams, The Hitchhiker's Guide to the Galaxy

The framework of the fitter, likelihood to be maximized and priors on the fit parameters were established in the previous chapters. This chapter provides the final data and Monte Carlo distributions that were provided as the input samples to the fitter. Using these samples, the output from the fitter gives the trace and the posterior distribution of the fit parameters. A comparison of the priors and posteriors of the parameters is presented. The distribution of signal weight parameters on-water, marginalized over all nuisance parameters will be used to calculate the final result of the number of signal events on-water. Posterior predictive plots, constructed by random sampling of the fit parameters from their posteriors, will demonstrate the effect of fit on the π^0 invariant mass distribution for each sample. A goodness-of-fit for this analysis

6.1 Input Samples

The final list of input samples used in this analysis are :

1. Selected sample water-in : Events passing all selection cuts for PØD water-in configuration
2. Selected sample - 'close' water-in : Events failing the shower separation distance cut but passing all other selection cuts for PØD water-in configuration
3. Background control sample water-in : Events failing the μ decay cluster cut but passing all other selection cuts for PØD water-in configuration

4. Background control sample - 'close' water-in : Events failing both the μ decay cluster and shower separation distance cut but passing the rest of the selection cuts for PØD water-in configuration

5. Selected sample water-out : Events passing all selection cuts for PØD water-out configuration

6. Selected sample - 'close' water-out : Events failing the shower separation distance cut but passing all other selection cuts for PØD water-out configuration

7. Background control sample water-out : Events failing the μ decay cluster cut but passing all other selection cuts for PØD water-out configuration

8. Background control sample - 'close' water-out : Events failing both the μ decay cluster and shower separation distance cut but passing the rest of the selection cuts for PØD water-out configuration

Samples (1) and (5) are the signal enriched samples from which the number of signal events on water is calculated. Samples (3) and (7) are the background enriched samples used to constrain the background under the signal peak in signal samples. Samples (2), (4), (6) and (8) are used to constrain the shower separation scale parameters described in Section 5.3.

Figures 6.1, 6.2, 6.3 and 6.4 show the POT normalized Monte Carlo and data distributions for the above listed samples forPØD water-in and water-out configurations side-by-side. The binning in these plots is the same as the one chosen for the fit. The last bin containing all events with invariant mass > 500 MeV is omitted in the plots for a clear presentation. The number of events in this bin are shown in the overflow text box. The events in the last bin are used for the fit but the final result are marginalized over that bin parameter.

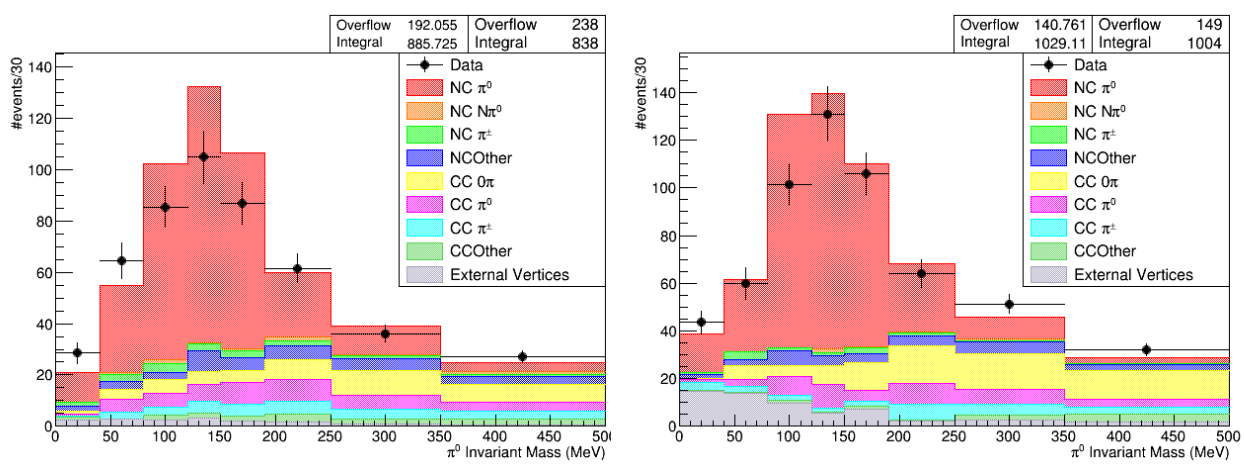

(a) Water-in configuration

(b) Water-out configuration

Figure 6.1: Invariant mass distribution of events passing all selection cuts.

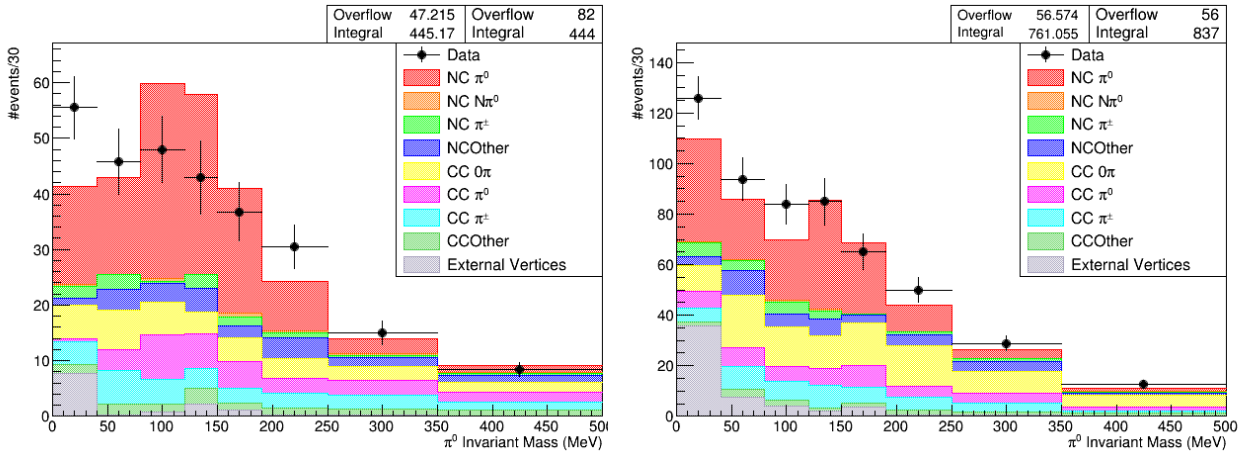

(a) Water-in configuration (b) Water-out configuration

Figure 6.2: Invariant mass distribution of events failing shower separation cut but passing all other cuts.

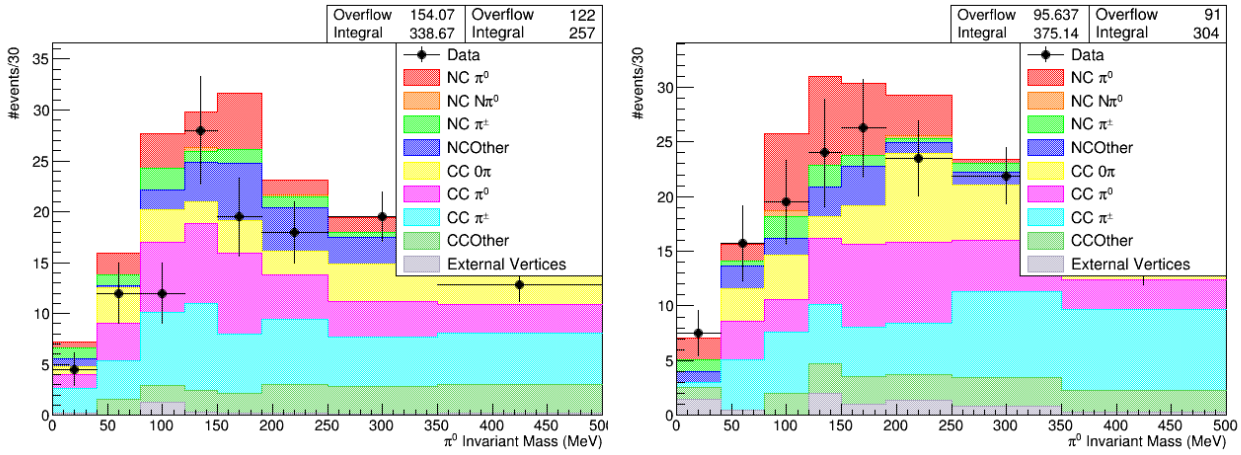

(a) Water-in configuration (b) Water-out configuration

Figure 6.3: Invariant mass distribution of events failing μ decay cluster cut but passing all other cuts.

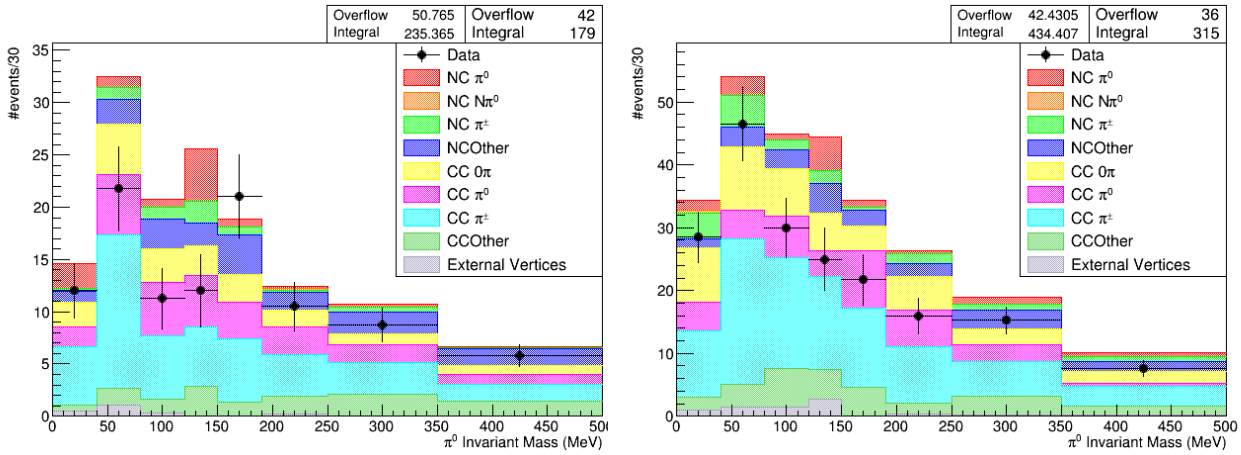

(a) Water-in configuration

(b) Water-out configuration

Figure 6.4: Invariant mass distribution of events failing μ decay cluster and shower separation cut but passing all other cuts.

6.2 Prior-Posterior Comparisons

In the MCMC fitter, if a step is accepted, the fitter will save the log likelihood value and the value of all fit parameters at that step while if the step is rejected the previous value is saved again. Fom the posterior distribution, all steps preceding the burn-in value are rejected as explained in Section 4.1. The mean and the rms of the 1 dimensional histogram of each parameter can be used to approximate the posterior distribution of that parameter marginalized over all the other parameters of the fit. Figures 6.5, 6.6, 6.7 and 6.8 provide a comparison for the posterior of all parameters in the fit with their priors.

The analysis samples are not expected to provide any strong constraints on the cross section and FSI parameters. As shown in Section 5.3, the detector systematics parameters are already constrained by fitting them to different control samples. The exceptions are the shower separation cut systematic parameters (parameter number 3 - 6), noticeable as the biggest red bands in Figure 6.7 to denote the large prior. These parameters are constrained very well by this fit as seen by the the small posteriors.

The signal weight parameters for events not on water, re-weight the signal events in all samples which interact on any target material other than water. These nuisance parameters do a lot of heavy lifting. The purpose of these parameters which are constrained by being exactly the same across all eight samples is to absorb any shape differences between data and Monte Carlo in signal which isn't covered by a systematic parameter. This, in principal, leaves the signal weight parameters on water to measure only the cross section differences between data and Monte Carlo.

Signal weight on water are the parameters of interest, shown in Figure 6.9. The last bin which is mostly composed of background events is also marginalized over in the calculation of signal events on water. Figure 6.10 shows the number of NC1π^0 events on water predicted by the nominal NEUT Monte Carlo. It also uses the mean value of signal weight parameters from Figure 6.9 and multiplies it with the predicted number in that bin to approximate the

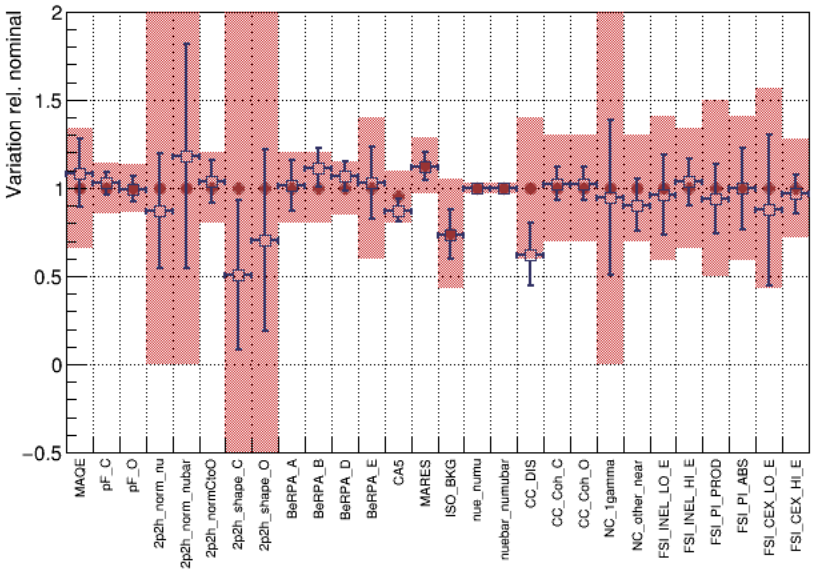

Figure 6.5: Comparison of prior and posterior of cross section and FSI parameters after the analysis fit.The one sigma error on the priors are highlighted by red boxes. The mean and the rms of the posterior histogram is plotted on top for comparison. The X axis labels all individual parameters.

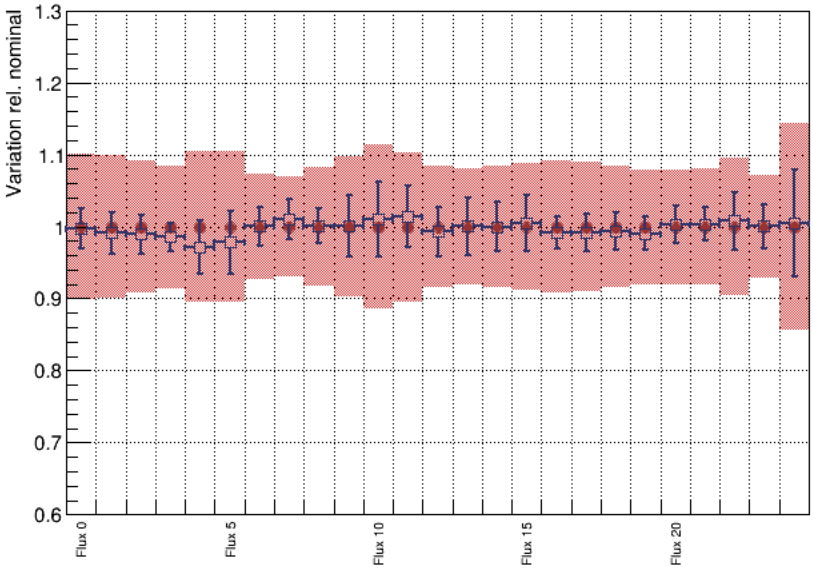

Figure 6.6: Comparison of prior and posterior of flux parameters after the analysis fit. The one sigma error on the priors are highlighted by red boxes. The mean and the rms of the posterior histogram is plotted on top for comparison. The numbers on X axis correspond to the order of parameters listed in Table 5.10.

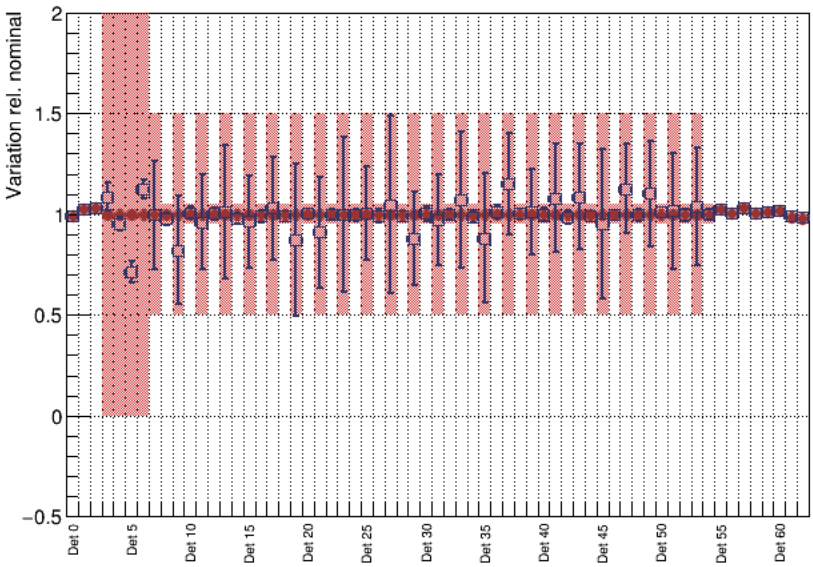

Figure 6.7: Comparison of prior and posterior of detector systematics parameters after the analysis fit.The one sigma error on the priors are highlighted by red boxes. The mean and the rms of the posterior histogram is plotted on top for comparison.

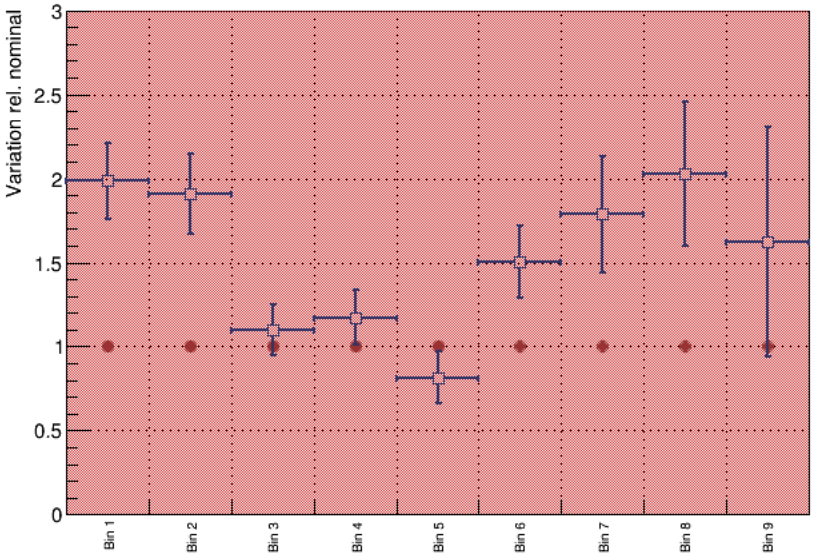

Figure 6.8: Comparison of prior and posterior of signal weight parameters for events not on water after the analysis fit. The one sigma error on the priors are highlighted by red boxes. The mean and the rms of the posterior histogram is plotted on top for comparison. The X axis labels the invariant mass bin that the parameter is used to re-weight.

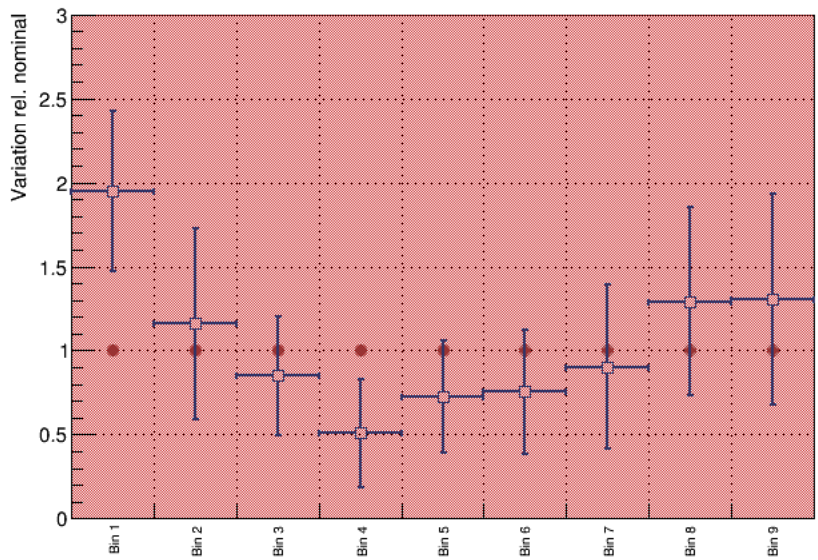

Figure 6.9: Comparison of prior and posterior of signal weight parameters for events on water after the analysis fit.The one sigma error on the priors are highlighted by red boxes. The mean and the rms of the posterior histogram is plotted on top for comparison.The X axis labels the invariant mass bin that the parameter is used to re-weight.

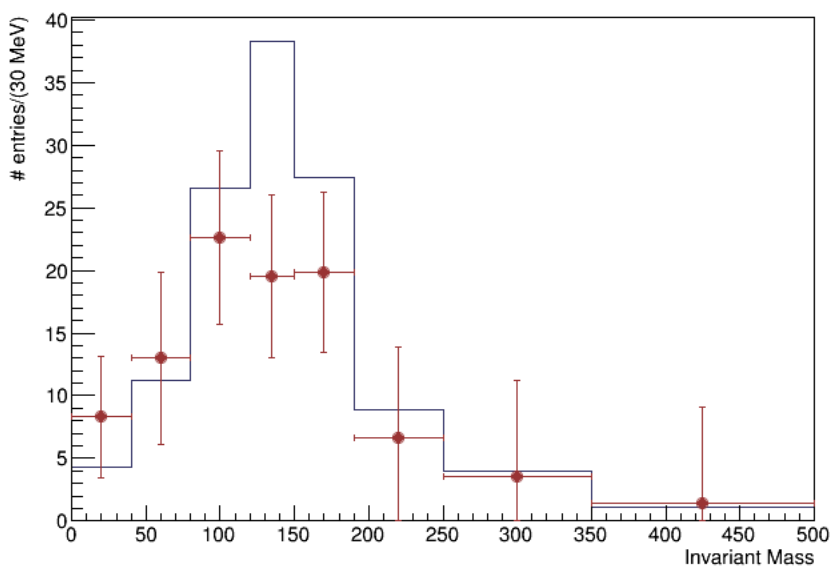

Figure 6.10: Comparison of number of NC1π^0 events on water predicted by the nominal NEUT Monte Carlo (blue histogram) with the best fit number of NC1π^0 events (red points) from the fit in that bin. The best-fit is calculated by using the mean of the 1D posterior of the signal weight on-water parameters multiplied by the predicted number of events in the bin by the nominal Monte Carlo.

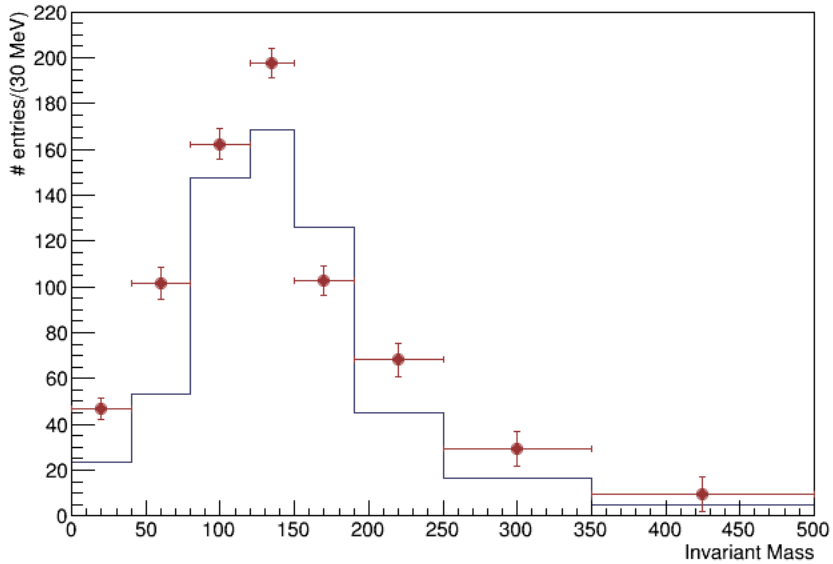

Figure 6.11: Comparison of number of NC1π^0 events not on water predicted by the nominal NEUT Monte Carlo (blue histogram) with the best fit number of NC1π^0 events (red points) from the fit in that bin. The best-fit is calculated by using the mean of the 1D posterior of the signal weight not-water parameters multiplied by the predicted number of events in the bin by the nominal Monte Carlo.

best fit value of NC1π^0 events in each bin. The large value of signal weight parameter in Bin 1 is compensated by the poor statistics of the bin for an overall negligible effect on the total fit.

6.3 Signal Event Rate

As explained in Section 4.2.1, Eq. 4.8 is used to calculate the number of signal events on water at each accepted step within the fitter. Using the parameter values at the same step of MCMC ensures that the correlations between all parameters are accounted for as each throw of the parameters incorporates the correlation matrix via $\mathcal{L}_{syst}$, given by Eq. 4.6.

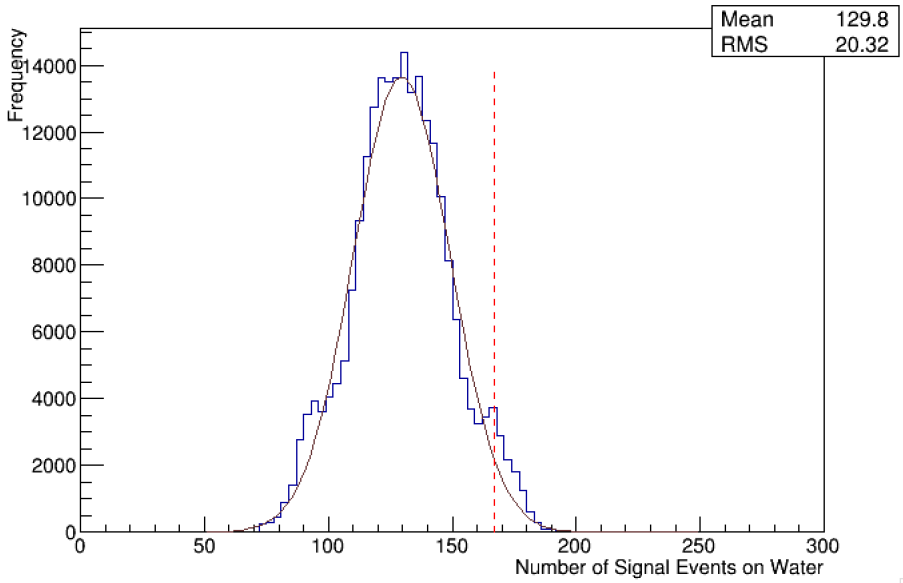

Figure 6.12: Number of signal events on water for invariant mass of 0 - 500 MeV marginalized over all nuisance parameters. The red line shows the nominal Monte Carlo prediction of 167 events.

The nominal Monte Carlo predicts 167 events on-water. Fitting all eight samples of data and Monte Carlo, described in Section 6.1 simulatenously for PØD water-in and PØD water-out gives 130 ± 20 events on water. A gaussian fit to the histogram of total number of signal events on water, Figure 6.12, gives a mean of 129.6 ± 19.6. The mean and root-mean-square from the histogram is chosen as the quoted result as it has a more conservative estimate of the uncertainty. This measurement includes all statistical and systematic uncertainties except the uncertainty in energy scale and fiducial volume. However, the calculations in Section 5.3 estimate both of these sources to contribute $< 1\%$ error which when added in quadrature with 15.6% error from this measurement remains the same. The ratio between nominal and the best fit value is 0.78 ± 0.12.

6.4 Posterior Predictive Distributions

While it is desirable to inspect the best fit Monte Carlo distribution to the data, it involves the non-trivial task of finding the mode of the posterior distribution in 134 dimensional parameter space. As a substitute, posterior predictive plots are drawn using the final posterior distributions of all parameters. The posteriors of all parameters need to be sampled simultaneously for the same step. One dimensional projections of the posteriors are marginalized over all other parameters and sampling from them individually ignores all correlations. To understand how these parameters impact the π^0 invariant mass distributions, a random throw is performed to pick a particular accepted step of all parameters. Using the values in this step, the nominal Monte Carlo is re-weighted to produce a new distribution. Repeating this random throw multiple times intrinsically provides the regions of higher density of

accepted parameter values. 5000 points were randomly sampled from the posterior distribution to form the posterior predictive distribution of each of the eight input samples shown in Figures 6.13 - 6.20.

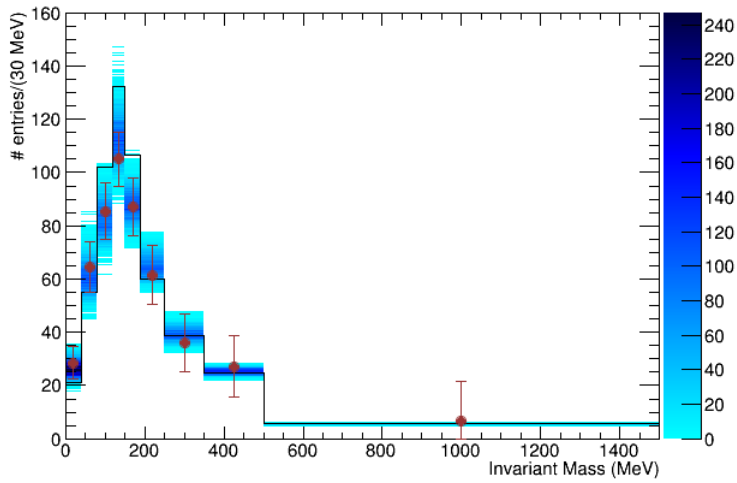

Figure 6.13: Posterior predictive plots for the selected sample for PØD water-in configuration. The black line represents the POT normalized nominal Monte Carlo distribution and the red line is the data. The blue density region shows 5000 random throws from the posteriors of all fit parameters.

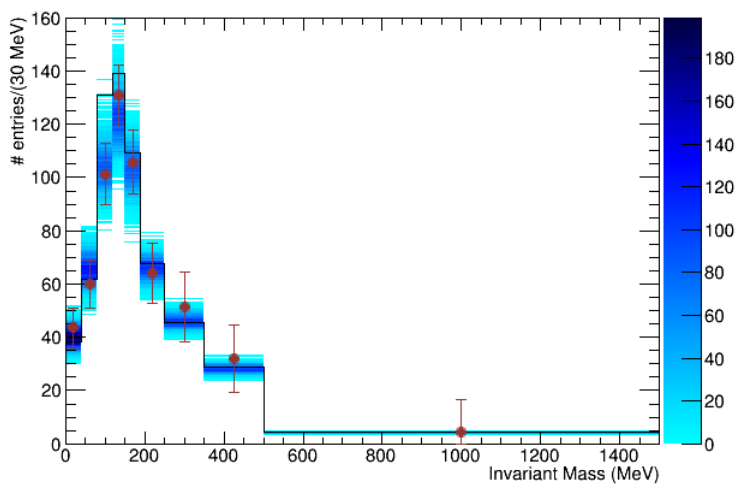

Figure 6.14: Posterior predictive plots for the selected sample for PØD water-out configuration. The black line represents the POT normalized nominal Monte Carlo distribution and the red line is the data. The blue density region shows 5000 random throws from the posteriors of all fit parameters.

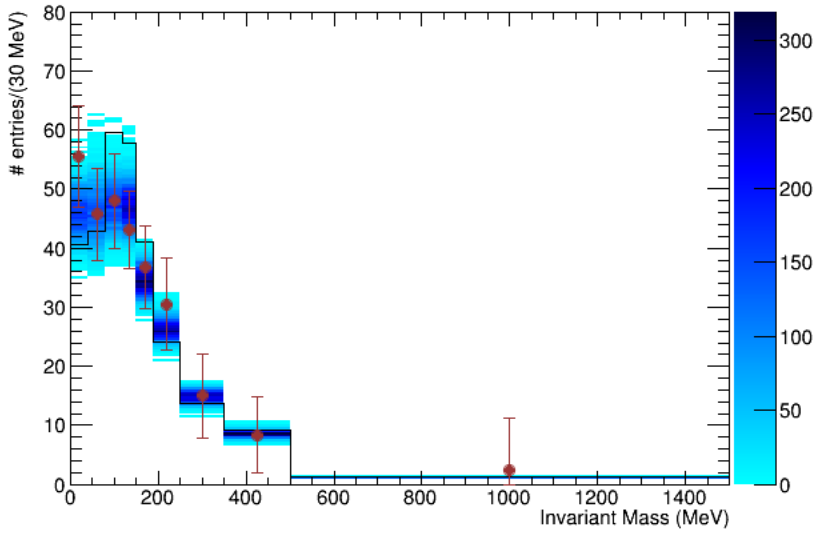

Figure 6.15: Posterior predictive plots for the selected sample events that fail the shower separation cut for PØD water-in configuration. The black line represents the POT normalized nominal Monte Carlo distribution and the red line is the data. The blue density region shows 5000 random throws from the posteriors of all fit parameters.

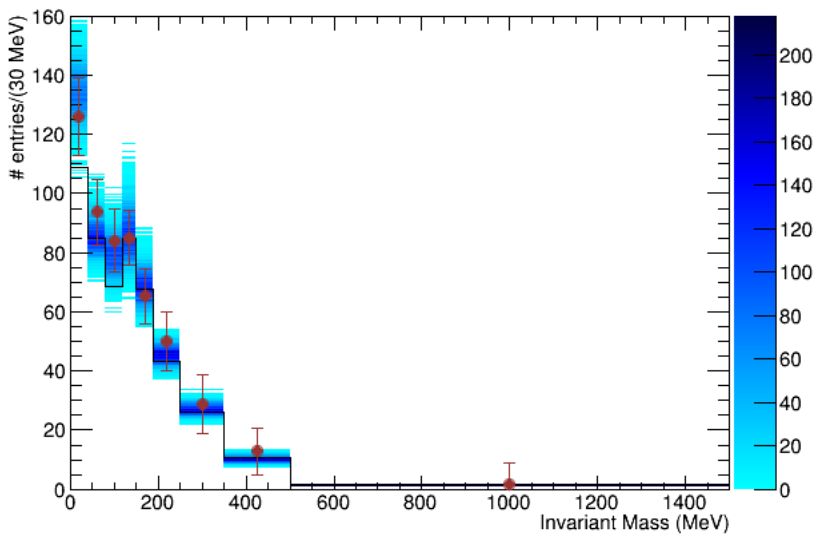

Figure 6.16: Posterior predictive plots for the selected sample events that fail the shower separation cut for PØD water-out configuration. The black line represents the POT normalized nominal Monte Carlo distribution and the red line is the data. The blue density region shows 5000 random throws from the posteriors of all fit parameters.

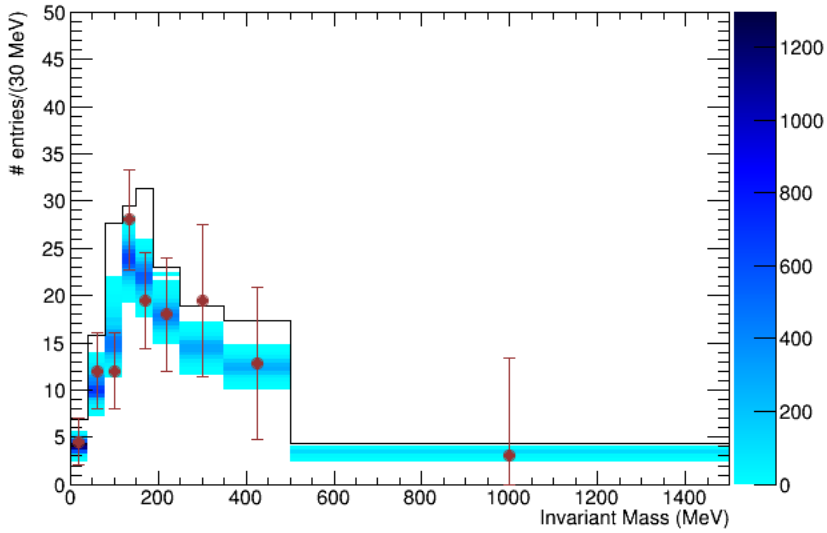

Figure 6.17: Posterior predictive plots for the background control sample for PØD water-in configuration. The black line represents the POT normalized nominal Monte Carlo distribution and the red line is the data. The blue density region shows 5000 random throws from the posteriors of all fit parameters.

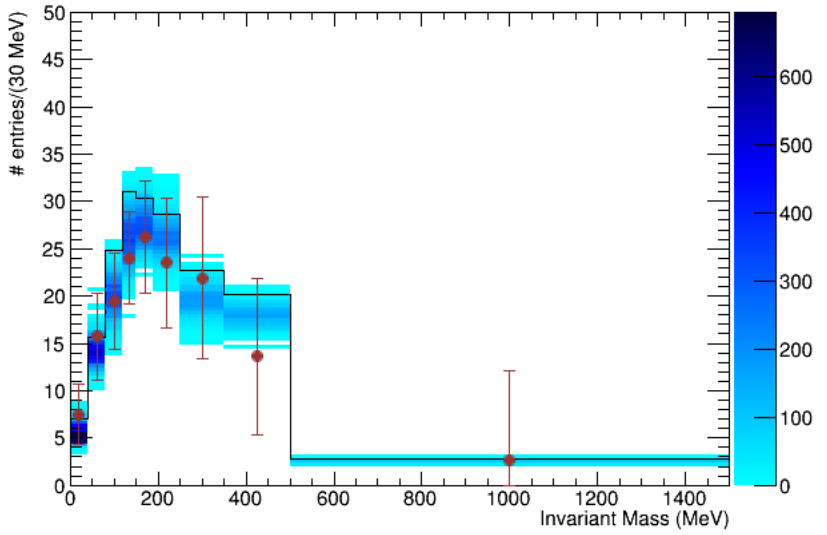

Figure 6.18: Posterior predictive plots for the background control sample for PØD water-out configuration. The black line represents the POT normalized nominal Monte Carlo distribution and the red line is the data. The blue density region shows 5000 random throws from the posteriors of all fit parameters.

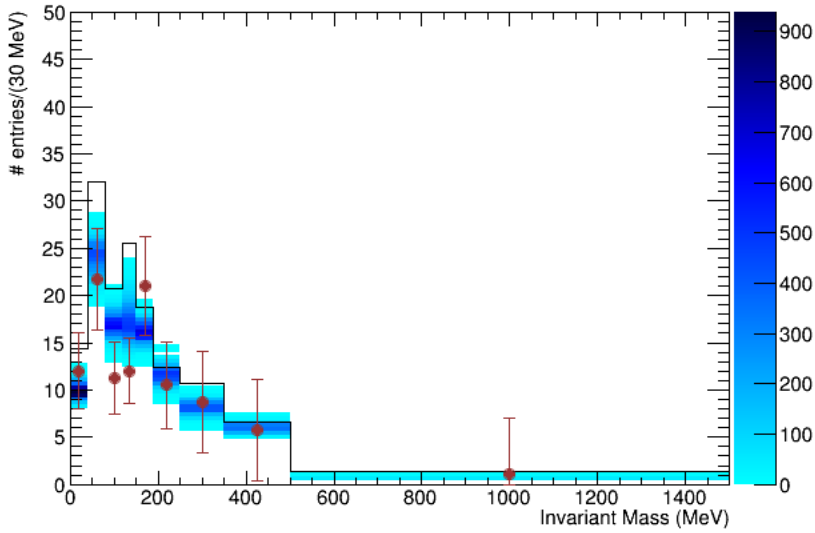

Figure 6.19: Posterior predictive plots for the background control sample events that fail the shower separation cut for PØD water-in configuration. The black line represents the POT normalized nominal Monte Carlo distribution and the red line is the data. The blue density region shows 5000 random throws from the posteriors of all fit parameters.

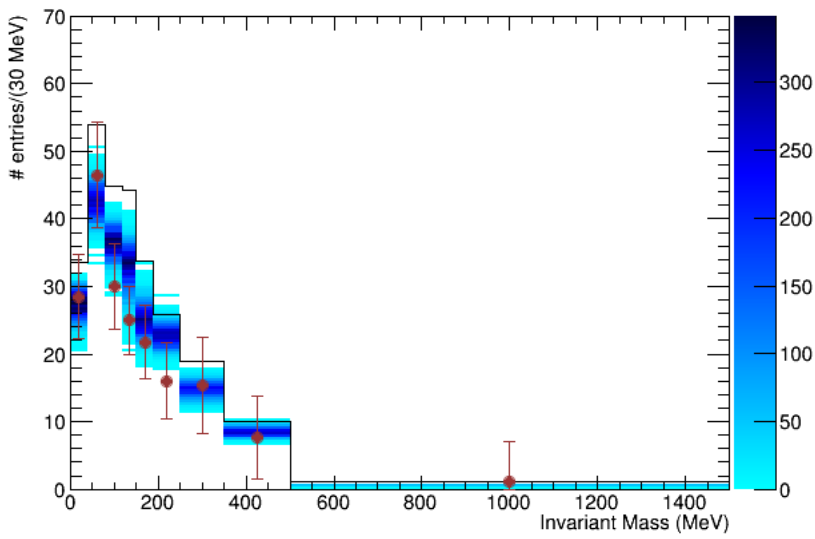

Figure 6.20: Posterior predictive plots for the background control sample events that fail the shower separation cut for PØD water-out configuration. The black line represents the POT normalized nominal Monte Carlo distribution and the red line is the data. The blue density region shows 5000 random throws from the posteriors of all fit parameters.

6.5 Goodness-of-Fit

The parameters of the model that best fit the data are obtained by the MCMC method of Bayesian inference. The posterior predictive distributions show the behavior of the Monte Carlo model for the parameters sampled from the posterior distributions. It is useful to measure a goodness-of-fit of the data with the Monte Carlo predictions calculated from parameter posteriors. A measure of p-value quantifies the probability of the occurrence of the given data set if the model predicted by the posteriors is true. It provides a criterion to reject the hypothesis but not an evidence to support it. Typically, a p-value of less than 0.05 is chosen as the criterion to reject the hypothesis.

A p-value for the posterior predictive spectra can be calculated using the method outlined by A. Gelman et al. [80]. At each throw of the posterior distribution of parameters used to generate the posterior predictive plots, a fake data set is created by a doing a poisson throw of the Monte Carlo prediction at that point. Two χ^2 are computed using the Poisson log-likelihood between the Monte Carlo prediction at the point with fake data set (χ^2 fake data), and another one with the real data set (χ^2 data). This is done for 5000 random sampling of posterior distribution. The p-value is calculated as the fraction of events for which χ^2 data $<$ χ^2 fake data. Figure 6.21 shows the two dimensional distribution of χ^2 data against χ^2 fake data. The black line represents the values for which χ^2 data $=$ χ^2 fake data and p-value is the fraction of points below it.

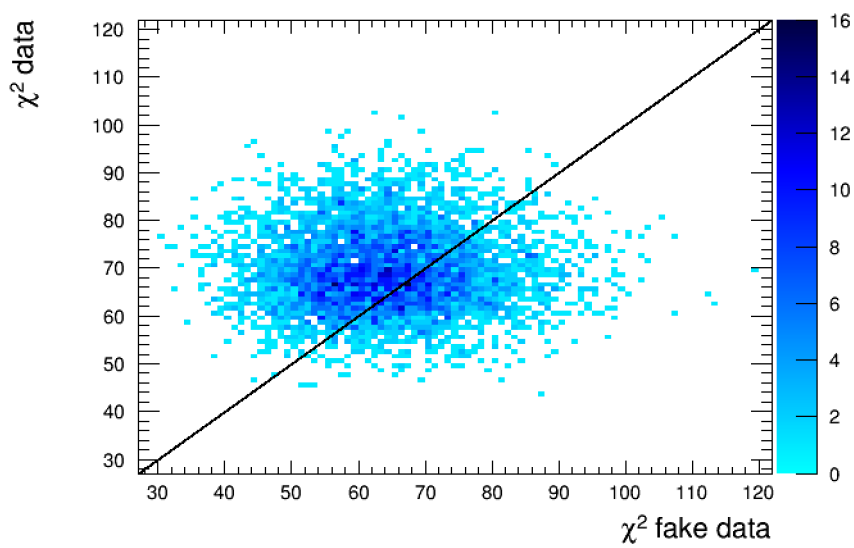

Figure 6.21: A distribution of χ^2 data vs χ^2 fake data. The fake data is obtained by the poisson throws of the Monte Carlo prediction obtained by the sampling of posterior distributions of the parameters. χ^2 measures the poisson log-likelihood between this Monte Carlo prediction and data or fake data. The line represents χ^2 data $=$ χ^2 fake data. p-value is the fraction of points below the line.

For this analysis a p-value of 0.35 for the simultaneous fit of all eight samples was calculated.

Chapter 7

Conclusion

"Would you tell me, please, which way I ought to go from here?"
"That depends a good deal on where you want to get to" said the Cat.
- Lewis Caroll, Alice in Wonderland

This thesis has presented an analysis of neutral current induced single π^0 production of neutrino interaction on water. In this chapter, the results of this analysis are summarized followed by suggestions and ideas to improve and further this analysis.

7.1 Summary

In this analysis, a set of selection cuts were implemented to obtain signal enriched sample. The neutrino beam data of T2K from Run 1, Run 2, Run 3, Run 4 and Run 8 were analyzed. T2K ran in the antineutrino beam mode from Run 5 - Run 7. This gives a total of 3.53×10^{20} POT for the PØD water-in configuration and 6.70×10^{20} POT for PØD water-out configuration. The selection cuts were developed using T2K nominal NEUT Monte Carlo event generator. An extensive restructuring of the software was required to implement this analysis in the standard T2K HighLAND software framework. The need and benefits of this work is discussed ahead in Appex. A. The cut on fraction of charge in shower particles was modified while the cut on shower separation distance was completely redefined. Although the cut on the weight difference in particle identification hypothesis remained unchanged but the underlying PID algorithm was improved between the earlier and current production of PØD reconstruction. These changes produce a signal sample with a purity of $52.9 \pm 1.8\%$ ($48.9 \pm 2.2\%$) and an efficiency of $9.2 \pm 0.3\%$ ($8.3 \pm 0.3\%$) for π^0 particles with an angle $< 60°$ from the beam axis in the PØD water-in (water-out) configurations.

Bayesian inference technique for parameter estimation is implemented with the use of Markov Chain Monte Carlo method to do a binned analysis fit in the π^0 invariant mass distribution. A simultaneous fit of PØD water-in and water-out configuration directly provides the result in terms of NC1π^0 events on water. The signal on-water parameters were marginalized over all the nuisance systematic parameters to obtain the final fit results inclusive of all statistical and systematic errors. The nominal Monte Carlo predicts 167 events . The data fit results in 130 ± 20 events on water. The ratio between nominal and the best fit value is 0.78 ± 0.12. This result is consistent with the previous ratio measurement of $0.68 \pm 0.26(\text{stat.}) \pm 0.44(\text{syst.})$.

7.2 Outlook

The next step for this analysis would be to do a fit in π^0 kinematic variables. It is one of the few T2K analysis that correctly reconstructs and identifies both decay photons of the π^0 particle 90% of the time. The resolution of π^0 momentum and direction for forward going particles is sufficient to make measurements in these variables. This step would greatly aide in making comparisons with different models in other event generators such as GENIE or NuWro. The next release of NEUT will also implement the new MK model [44] which further modifies the pion production rate of neutrino interactions.

While in the software, it is straightforward to extend the new MCMC fitter framework to add analysis bins in π^0 kinematics but it is non-trivial to implement this properly. To compare against a model, the events typically have to be efficiency corrected, flux averaged and unfolded to true kinematics phase space. Efficiency correction should be done in bins of relatively flat efficiencies so as to minimize the model dependence in an inherently Monte Carlo dependent step. The limited statistics of NC1π^0 events makes it even harder as sufficient statistics should exist in each bin or efficiency correction just reproduces the Monte Carlo simulation. It is unreasonable to calculate the energy of incoming neutrino based on just the outgoing π^0 energy as the outgoing neutrino escapes and the nucleon is seldom detected. Even for charged current interactions with only μ and the nucleon in the final state, the impact of the presence of nuclear matter around the target nucleon are still poorly understood. Estimating the incoming neutrino energy would require depending on the models to account for these effects. While it is common to report results averaged over the whole neutrino flux of the beam, the average neutrino energy producing NC1π^0 is 1.4 GeV, as compared to the nominal T2K flux of 0.6 GeV. Further attention should be paid while averaging over the T2K flux and assigning flux uncertainties using input from beam group developed for the oscillation analysis. There are ongoing discussions in the neutrino cross-section community regarding the validity and stability of unfolding processes to go from the reconstructed kinematics to true kinematics phase space of a particle for a comparison to theoretical model. The unfolding process needs to be carefully chosen and rigorously validated before implementation.

As the MCMC fitter used in this analysis is a newly developed software package, the parameterization of systematics uncertainties as nuisance parameters in the fit needs to be further investigated. While it is a beneficial feature of the bayesian analysis that all the systematics uncertainties are naturally taken into account when marginalized over all

nuisance parameters, it limits the understanding of each specific systematic contribution to the final result. Studies can be done by varying only one set of parameters and fixing others for a control sample or a fake data set to understand the impact and coverage of systematic parameters. In particular, for detector systematics, the parametrization for PID systematics parameter could be changed as they are highly correlated with each other which reduces the efficiency of MCMC sampling. Some combination of the underlying 48 parameters into a small number of 'effective' parameter set is required. An estimate of the error due to difference in energy scale, calculated by varying the π^0 reconstruction efficiency, is added to this analysis. Although, it would fit more naturally in the kinematically binned analysis which will implement efficiency correction in true π^0 momentum bins. Moreover, changing this systematics such that it measures the effect of energy scale on each photon reconstruction instead of the π^0 particle would provide a more rigorous approach. The impact of vertex resolution on the shower based analyses has always been small but a validation against data from control sample is desirable. However, attempts at finding CCπ^0 events in PØD that can serve as ideal control samples have been unsuccessful in the past with $< 2\%$ for such selections.

On the cross-section side, the impact of final state interactions of proton on this analysis is unknown. New efforts are being made in T2K to implement systematics caused by secondary interactions of pions and protons after leaving the nucleus in which they interact. Effects of secondary interaction in PØD on this analysis should be tested and implemented once the parameterizations are fully mature.

Lastly, the priors on signal event weight parameters do not reflect all the information that we have about them a priori. They are currently allowed to move in the fit independent of each other with no in-built correlation. However, the knowledge that π^0 invariant mass peak should be approximately Gaussian with a mean around π^0 invariant mass and width from detector resolutions and systematics should ideally form the prior on these parameters. It can be introduced as some form of regularization between neighboring bins but the exact details and values would need to be investigated.

T2K has been running with reverse horn current beam collecting equal POT in this anti-neutrino beam mode. Analyzing NC1π^0 interactions for anti-neutrino beam would be useful for a study of a ratio of neutrino and antineutrino cross-section or a joint fit of both beam modes.

Finally, the T2K oscillation analysis fitters use standardized ND280 samples from HighLAND framework to constrain the oscillation fit. A switch to HighLAND framework was made to make it possible to add these samples in the oscillation analysis fits to constrain neutral current events. Adapting both HighLAND and the reconstruction used for this analysis to work with each other was a major task which was completed successfully. However, the systematics for this analysis are currently calculated as nuisance parameter in the MCMC fitter. To enable use of these samples in oscillation analysis fit, the systematics would have to be implemented in HighLAND as well. This is not expected to require any major structural change to HighLAND package.

References

[1] C. Burgard. Standard model image in tex. `http://www.texample.net/tikz/examples/model-physics/`.

[2] S. Abe et al. Precision measurement of neutrino oscillation parameters with KamLAND. *Physical Review Letters*, 100(22), 2008.

[3] K. Abe and others [SK Collaboration]. Atmospheric neutrino oscillation analysis with external constraints in Super-Kamiokande I-IV. *Physical Review D*, 97(7), 2018.

[4] K. Abe and others [T2K Collaboration]. Measurement of neutrino and antineutrino oscillations by the T2K experiment including a new additional sample of ν_e interactions at the far detector. *Physical Review D*, 96(9), 2017.

[5] P. Adamson and others [NOνA Collaboration]. Constraints on oscillation parameters from ν_e appearance and ν_μ disappearance in NOνA. *Physical Review Letters*, 118(23), 2017.

[6] D. Casper. The nuance neutrino physics simulation, and the future. *Nuclear Physics B - Proceedings Supplements*, 112(1-3), 2002.

[7] J. A. Formaggio and G. P. Zeller. From eV to EeV: Neutrino cross sections across energy scales. *Reviews of Modern Physics*, 84(3):1307–1341, 2012.

[8] S. Yamamoto. *Search for μ to e Oscillation in a Long-baseline Accelerator Experiment*. PhD thesis, Kyoto University, 2006.

[9] G.P. Zeller. Low Energy Neutrino Cross Sections: Comparison of Various Monte Carlo Predictions to Experimental Data. *arXiv:hep-ex/0312061*, December 2003.

[10] K. Abe et al. Measurement of the single π^0 production rate in neutral current neutrino interactions on water. *Physical Review D*, 97(3), 2018.

[11] S. Assylbekov et al. The T2K ND280 off-axis pi–zero detector. *Nuclear Instruments and Methods in Physics Research Section A: Accelerators, Spectrometers, Detectors and Associated Equipment*, 686, 2012.

[12] Karin Gilje. *Neutral Current π^0 Production Rate Measurement On-Water Using the Pi-Zero Detector in the Near Detector of the T2K Experiment*. PhD thesis, Stony Brook University, `https://ir.stonybrook.edu/xmlui/handle/11401/76700`, 2012.

[13] W. R. Gilks, S. Richardson, and D. J. Spiegelhalter. *Markov Chain Monte Carlo in Practice*. Chapman and Hall/CRC, 1995.

[14] S. Bolognesi et al. NIWG model and uncertainties for 2017 oscillation analysis. T2K Technical Note 315, `http://www.t2k.org/docs/technotes/315`, 2017.

[15] M. Tanabashi et al. Review of particle physics. *Physical Review D*, 98(3), 2018.

[16] A. A. Aguilar-Arevalo et al. Measurement of ν_μ and $\bar{\nu}_\mu$ induced neutral current single π^0 production cross sections on mineral oil at E$\nu\sim$O(1 GeV). *Physical Review D*, 81(1), 2010.

[17] K. Kodama and others [DONUT Collaboration]. Observation of tau neutrino interactions. *Physics Letters B*, 504(3), 2001.

[18] M. Cribier et al. Results of the whole GALLEX experiment. *Nuclear Physics B - Proceedings Supplements*, 70(1-3):284–291, jan 1999.

[19] J. N. Abdurashitov et al. Solar neutrino flux measurements by the soviet-american gallium experiment (SAGE) for half the 22-year solar cycle. *Journal of Experimental and Theoretical Physics*, 95(2), 2002.

[20] Q. R. Ahmad et al. Direct evidence for neutrino flavor transformation from neutral-current interactions in the sudbury neutrino observatory. *Physical Review Letters*, 89(1), 2002.

[21] Y. Fukuda et al. Evidence for oscillation of atmospheric neutrinos. *Physical Review Letters*, 81(8), 1998.

[22] S. Schael et al. Precision electroweak measurements on the z resonance. *Physics Reports*, 427, 2006.

[23] E. K. Akhmedov. Neutrino Physics. In *Particle Physics*, page 103, 2000.

[24] B Aharmim and others [SNO Collaboration]. Electron energy spectra, fluxes, and day-night asymmetries of B^8 solar neutrinos from measurements with nacl dissolved in the heavy-water detector at the sudbury neutrino observatory. *Phys. Rev. C72, 055502*, 2005.

[25] Nick Jelley et al. The sudbury neutrino observatory. *Annu. Rev. Nucl. Part. Sci. 2009. 59:431–6*, 2009.

[26] K. Eguchi et al. First results from KamLAND: Evidence for reactor antineutrino disappearance. *Physical Review Letters*, 90(2), 2003.

[27] M Ambrosio et al. Measurement of the atmospheric neutrino-induced upgoing muon flux using MACRO. *Physics Letters B*, 434(3-4), 1998.

[28] M. Sanchez et al. Measurement of the L/E distributions of atmospheric $\bar{\nu}$ in Soudan 2 and their interpretation as neutrino oscillations. *Physical Review D*, 68(11), 2003.

[29] K. Abe et al. Indication of electron neutrino appearance from an accelerator-produced off-axis muon neutrino beam. *Physical Review Letters*, 107(4), 2011.

[30] F. P. An et al. Observation of Electron-Antineutrino Disappearance at Daya Bay. *Physical Review Letters*, 108(17), 2012.

[31] F. P. An et al. Measurement of electron antineutrino oscillation based on 1230 days of operation of the Daya Bay experiment. *Physical Review D*, 95(7), 2017.

[32] DUNE Collaboration, R. Acciarri, et al. Long-Baseline Neutrino Facility (LBNF) and Deep Underground Neutrino Experiment (DUNE) Conceptual Design Report Volume 2: The Physics Program for DUNE at LBNF. *arXiv:1512.06148*, December 2015.

[33] K. Abe et al. Physics potential of a long-baseline neutrino oscillation experiment using a J-PARC neutrino beam and Hyper-Kamiokande. *Progress of Theoretical and Experimental Physics*, 2015(5), 2015.

[34] Yoshinari Hayato. A neutrino interaction simulation program librarary NEUT. *Acta Physical Polonica B 40, 2477 (2009)*, 2009.

[35] C. Andreopoulos et al. The GENIE neutrino monte carlo generator. *Nuclear Instruments and Methods in Physics Research Section A: Accelerators, Spectrometers, Detectors and Associated Equipment*, 614(1), 2010.

[36] T. Leitner, O. Buss, L. Alvarez-Ruso, and U. Mosel. Electron- and neutrino-nucleus scattering from the quasielastic to the resonance region. *Physical Review C*, 79(3), 2009.

[37] O. Buss, T. Gaitanos, K. Gallmeister, H. van Hees, M. Kaskulov, O. Lalakulich, A.B. Larionov, T. Leitner, J. Weil, and U. Mosel. Transport-theoretical description of nuclear reactions. *Physics Reports*, 512(1-2), 2012.

[38] Tomasz Golan, Cezary Juszczak, and Jan T. Sobczyk. Effects of final-state interactions in neutrino-nucleus interactions. *Physical Review C*, 86(1), 2012.

[39] C.H. Llewellyn Smith. Neutrino reactions at accelerator energies. *Physics Reports*, 3(5), 1972.

[40] Dieter Rein and Lalit M Sehgal. Neutrino-excitation of baryon resonances and single pion production. *Annals of Physics*, 133(1):79–153, apr 1981.

[41] Dieter Rein and Lalit M. Sehgal. Coherent π^0 production in neutrino reactions. *Nuclear Physics B*, 223(1), 1983.

[42] Ch. Berger and L. M. Sehgal. Lepton mass effects in single pion production by neutrinos. *Physical Review D*, 76(11), 2007.

[43] Krzysztof M. Graczyk and Jan T. Sobczyk. Form factors in the quark resonance model. *Physical Review D*, 77(5), 2008.

[44] M. Kabirnezhad. Single pion production in neutrino-nucleon interactions. *Physical Review D*, 97(1), 2018.

[45] R. A. Smith and E. J. Moniz. Neutrino reactions on nuclear targets. *Nuclear Physics B*, 101(2), 1975.

[46] S. K. Singh and E. Oset. Inclusive quasielastic neutrino reactions inC12ando16at intermediate energies. *Physical Review C*, 48(3), 1993.

[47] Omar Benhar and Adelchi Fabrocini. Two-nucleon spectral function in infinite nuclear matter. *Physical Review C*, 62(3), 2000.

[48] J. Nieves, I. Ruiz Simo, and M. J. Vicente Vacas. Inclusive charged-current neutrino-nucleus reactions. *Physical Review C*, 83(4), 2011.

[49] R. Gran, J. Nieves, F. Sanchez, and M. J. Vicente Vacas. Neutrino-nucleus quasi-elastic and 2p2h interactions up to 10 GeV. *Physical Review D*, 88(11), 2013.

[50] M. Martini, M. Ericson, G. Chanfray, and J. Marteau. Unified approach for nucleon knock-out and coherent and incoherent pion production in neutrino interactions with nuclei. *Physical Review C*, 80(6), 2009.

[51] K. Abe et al. Characterization of nuclear effects in muon-neutrino scattering on hydrocarbon with a measurement of final-state kinematics and correlations in charged-current pionless interactions at T2K. *Physical Review D*, 98(3), 2018.

[52] C. E. Patrick et al. Measurement of the muon antineutrino double-differential cross section for quasielastic-like scattering on hydrocarbon at $E_{\bar{\nu}}$ ∼3.5GeV. *Physical Review D*, 97(5), 2018.

[53] S. J. Barish et al. Observation of single-pion production by a weak neutral current. *Physical Review Letters*, 33(7), 1974.

[54] M. Derrick et al. Study of single-pion production by weak neutral currents in low-energyνdinteractions. *Physical Review D*, 23(3), 1981.

[55] E. Hawker. Single pion production in low energy ν-carbon interactions. In *Proceedings of the 2nd International Workshop on Neutrino Nucleus Interactions in the Few GeV Region (NuInt'02)*, 2002.

[56] W. Lee et al. Single-pion production in neutrino and antineutrino reactions. *Physical Review Letters*, 38(5):202–204, jan 1977.

[57] Paul Joseph Nienaber. *Single Neutral Pion Production in Charged Current and Neutral Current Neutrino Interactions*. PhD thesis, University of Illinois at Urbana-Champaign, 1988.

[58] G.L. Fogli and G. Nardulli. Neutral current induced one-pion production. *Nuclear Physics B*, 165(1):162–184, 1980.

[59] S. Nakayama et al. Measurement of single π^0 production in neutral current neutrino interactions with water by a 1.3 GeV wide band muon neutrino beam. *Physics Letters B*, 619(3-4), 2005.

[60] Y. Kurimoto et al. Measurement of inclusive neutral current π^0 production on carbon in a few-GeV neutrino beam. *Physical Review D*, 81(3), 2010.

[61] Y. Kurimoto et al. Improved measurement of neutral current coherent π^0 production on carbon in a few-GeV neutrino beam. *Physical Review D*, 81(11), 2010.

[62] R. Acciarri et al. Measurement of ν_μ and $\bar{\nu}_\mu$ neutral current $\pi^0 \rightarrow \gamma\gamma$ production in the ArgoNeuT detector. *Physical Review D*, 96(1), 2017.

[63] K. Abe and others [T2K Collaboration]. The T2K experiment. *Nuclear Instruments and Methods in Physics Research Section A: Accelerators, Spectrometers, Detectors and Associated Equipment*, 659(1), 2011.

[64] G. Battistoni et al. The FLUKA code: description and benchmarking. In *AIP Conference Proceedings*. AIP, 2007.

[65] A. Ferrari, P. R. Sala, A. Fasso, and J. Ranft. FLUKA: A Multi-Particle Transport Code. Report No. SLAC-R773 `https://www.slac.stanford.edu/pubs/slacreports/reports16/slac-r-773.pdf`, 2005.

[66] R. Brun, F. Carminati, and S. Giani. GEANT: Detector Description and Simulation Tool. Technical Report No. CERN-W5013 (1994), `http://www.slac.stanford.edu/comp/physics/cernlib/cerndoc/geant/aaaa.ps.gz`, 1994.

[67] C. Zeitnitz and T.A. Gabriel. The GEANT-CALOR interface and benchmark calculations of ZEUS test calorimeters. *Nuclear Instruments and Methods in Physics Research Section A: Accelerators, Spectrometers, Detectors and Associated Equipment*, 349(1), 1994.

[68] N. Abgrall et al. Measurements of cross sections and charged pion spectra in proton-carbon interactions at 31 GeV/c. *Physical Review C*, 84(3), 2011.

[69] N. Abgrall et al. Measurement of production properties of positively charged kaons in proton-carbon interactions at 31 GeV/c. *Physical Review C*, 85(3), 2012.

[70] Antonin Vacheret, Sarah Greenwood, Matt Noy, Mark Raymond, and Alfons Weber. The front end readout system for the T2K-ND280 detectors. In *2007 IEEE Nuclear Science Symposium Conference Record*. IEEE, 2007.

[71] Karin Gilje et al. Geometry and Mass of the PØD in the ND280 Basket. T2K Technical Note 73, http://www.t2k.org/docs/technotes/73, 2012.

[72] A. Cervera-Villanueva, J.J. Gómez-Cadenas, and J.A. Hernando. "RecPack" a reconstruction toolkit. *Nuclear Instruments and Methods in Physics Research Section A: Accelerators, Spectrometers, Detectors and Associated Equipment*, 534(1-2):180–183, 2004.

[73] Phoc Trung Le. *Event reconstruction and energy calibration using cosmic muons for the T2K π^0 detector*. PhD thesis, Stony Brook University, 2009.

[74] Nicholas Metropolis, Arianna W. Rosenbluth, Marshall N. Rosenbluth, Augusta H. Teller, and Edward Teller. Equation of state calculations by fast computing machines. *The Journal of Chemical Physics*, 21(6), 1953.

[75] W. K. Hastings. Monte carlo sampling methods using markov chains and their applications. *Biometrika*, 57(1), 1970.

[76] K. Mahn et al. 2016 XSEC-NIWG Inputs. https://www.t2k.org/nd280/physics/xsec/docs/xsec-niwg-doc/niwg2016, 2016.

[77] C. Wilkinson et al. Testing charged current quasi-elastic and multinucleon interaction models in the NEUT neutrino interaction generator with published datasets from the MiniBooNE and MINERνA experiments. *Physical Review D*, 93(7), 2016.

[78] Melanie Day and Kevin S. McFarland. Differences in quasielastic cross sections of muon and electron neutrinos. *Physical Review D*, 86(5), 2012.

[79] E. Wang, L. Alvarez-Ruso, Y. Hayato, K. Mahn, and J. Nieves. Photon emission in neutral current interactions at the T2K experiment. *Physical Review D*, 92(5), 2015.

[80] Andrew Gelman, Xioa-Li Meng, and Hal Stern. Posterior Predictive Assessment of Model Fitness via Realized Discrepancies. Statistica Sinica 6(1996) 733-807 http://www3.stat.sinica.edu.tw/statistica/j6n4/j6n41/j6n41.htm.

Appendix A

Adapting Analysis Tools Software to Interface with PØD Reconstruction

Each sub-detector of ND280 maintains an independent reconstruction algorithm alongside a global reconstruction for the whole off-axis detector, as explained in Section 2.4.1. A software package, called *High Level Analysis at Near Detector* (HighLAND) provides analysis tools for event selections, implementation of systematics, plotting schemes and techniques. As HighLAND provides standardized output samples for all inputs, the softwares that fit near and far detector samples to obtain oscillation parameters designed their framework to accept near detector samples in HighLAND format. Thus for a near detector sample to be used in T2K oscillation analysis, the selections and systematics have to be implemented in the HighLAND framework.

The early samples used for constraining oscillation parameters were charged current samples from tracker region of near detector. Due to its origins based in tracker based analysis, HighLAND was designed to implement global reconstruction of ND280.

When the task of expanding HighLAND to make it compatible with local reconstruction of sub-detectors was undertaken, PØD reconstruction provided difficult challenges due to a mismatch in the fundamental architecture of the data handling and storage in the two softwares. This project is outlined below using simplistic schematics of the storage structures in each software package.

The layout of PØD reconstruction (PØDRecon) was established in Section 2.4.1. Figure A.1 depicts the way in which PØDRecon stores the outputs from its various reconstruction algorithm. It essentially creates a vector of all possible reconstructed vertex, particles, clusters and hits, and links them to each other using pointers in accordance with the information provided by different reconstruction algorithm. The user can choose a particular reconstruction algorithm (such as Track, Shower or Delayed Muon Decay Cluster Reconstruction) and follow the chain of pointers to extract the relevant particles their vertex and hits. This can be labeled as a 'parallel architecture'.

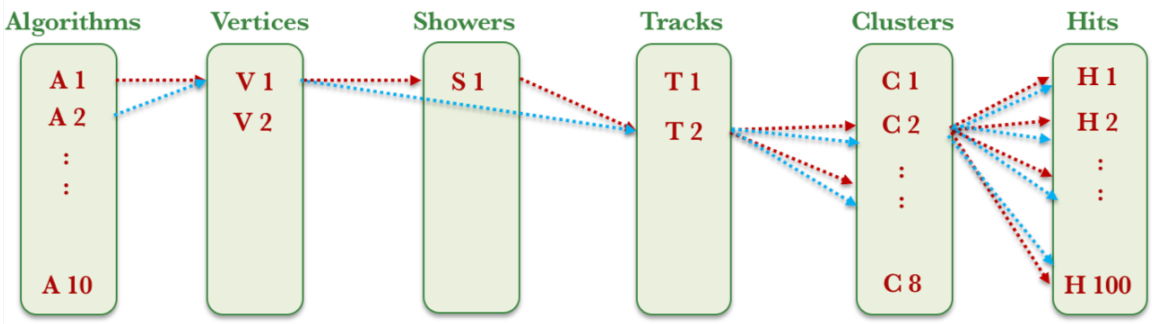

Figure A.1: Parallel architecture of data storage in PØDRecon. The different colored arrows show the chain of pointers that is selected contingent on the reconstruction algorithms that is picked by the user.

HighLAND package uses the more traditional 'hierarchical architecture' where an event contains particles which are formed from hits in the detector, Figure A.2. In its original form, particles in HighLAND could only be reconstructed tracks.

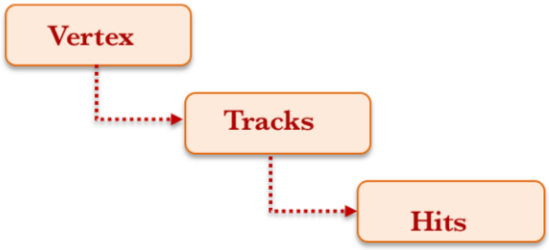

Figure A.2: Schematic depiction of hierarchical structure of classes in HighLAND software package prior to modifications to make it compatible with PØDRecon.

There were many modifications required in the core structure of HighLAND for it to store all information available in PØDRecon. As all previous tracker analyses were done using HighLAND, it had to be backward compatible. The most fundamental changes are shown in Figure A.3. The class available for storing particle information was modified to accept a reconstructed track or a shower particle. An extra class was introduced to hold information about clusters of hits used widely in this analysis. The figure does not depict a class labeled by 'Event' which holds instances of class vertex. To avail two or more reconstruction algorithms from PØDRecon simulatenously, a vector of 'Event' can be created which holds separate reconstruction information in each cell.

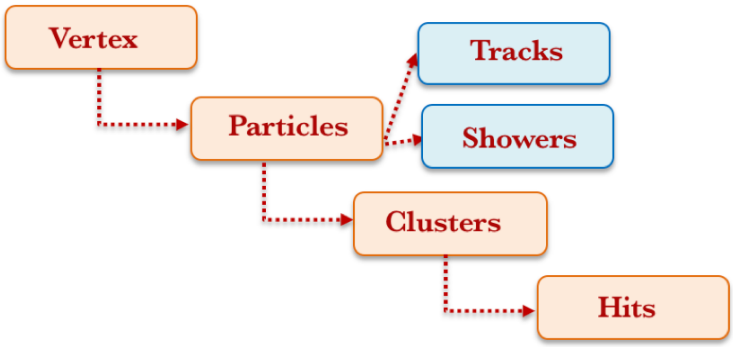

Figure A.3: Modified structure of classes in HighLAND software that support interfacing with PØD reconstruction.

All PØD analyses since the implementation of these changes are written in HighLAND framework. Work is presently ongoing to incorporate a mature CC0π analysis from PØD to near detector samples in oscillation analysis.